

Ph.D. Thesis

Study on the Inclusive Production
Cross Section of Forward Muons
in $p\bar{p}$ Collisions at $\sqrt{s} = 1.8$ TeV

José Guilherme Rocha de Lima

Centro Brasileiro de Pesquisas Físicas

Rio de Janeiro — May 1995

To my *princess*
Gabriella
with love and
fondness

Acknowledgments

To my advisor and friend Alberto Santoro, for the guidance and support throughout the development of the present work, but mainly for all the special attention dedicated through the seven years I have been part of his professional life. His availability and tenacity on the arduous fight against all sort of difficulties in our research field, and mainly in our country, are strong examples I would like to follow, though doubting my ability in doing it with such a competence.

To my friend Arthur Maciel, for the friendship and active partnership in innumerable hours of discussions and hard work, including many suggestions along this thesis. His seriousness and competence in research activities is another example I will always have in mind along my professional career.

To Gilvan Alves, for all the experience transmitted in so many discussions on Physics, hardware, computing or any other topic related to our research field, and also for the critical reading of the previous versions of this thesis.

To Vitor Oguri, for the interchange of ideas about Physics, computing and electronics, for so many hours of cooperative work in the $D\bar{O}$ trigger system, and also for the family environment of West Chicago.

To my friends João Torres and Jussara Miranda, for the friendship and companionship inside and outside LAFEX, for the permanent support, and for some contributions to the present work. I am sure these contributions would be much larger if we had had more than only a few days together since our engagement in $D\bar{O}$ up to the conclusion of this thesis.

To Moacyr Souza, always obliging, for many discussions, especially about programming, which much enriched my formation.

To the other LAFEX colleagues who are members of $D\bar{O}$ Collaboration, especially Mário Vaz, for the discussions on electronics, and also Wagner Carvalho, Marcello Nicola and André Sznajder, who were always available for help, and therefore also contributed to this work.

To all other members of the experimental wings of LAFEX, for turning it into a pleasant environment for the development of high quality research.

To Kamel Bazizi, for the collaborative work along two years I have spent at Fermilab, for the support and confidence in giving me the responsibility for many activities for the development of the Level 1 Muon Trigger System at $D\bar{O}$, and also to innumerable discussions about hardware and data analysis.

To Profs. Dave Hedin, Ken Johns, Andrzej Zieminski, Daria Zieminska and especially to Profs. Daniel Green and Dmitri Denisov, for many fruitful discussions and suggestions regarding the present analysis.

To Profs. Paul Grannis, Hugh Montgomery, spokespersons for DØ Collaboration, and to Prof. Eugene Fisk, for their competent ability in conducting this huge Collaboration. And besides them, also to Prof. Roy Rubinstein, for all the support provided to LAFEX group.

To all other members of DØ Collaboration (about 440 researches from eight countries), responsible for the construction and operation of the DØ detector, thus making possible the development of our analysis and results.

To Profs. Carlos O. Escobar, José Bellandi Filho and Ronald Shellard, for having accepted to participate in the committee to examine and judge this thesis, for the constructive and objective criticism.

To Myriam Coutinho, for the friendship and all the attention in the early months of my stay in Rio de Janeiro, and also for the seriousness and fondness always dedicated to the graduate students at CBPF.

To my teacher and good friend Henrique Antunes Neto, with whom I had the pleasure of innumerable hours of nice and fruitful discussions in my undergraduate studies at UFPa. His presence will be kept forever in my memories.

Also to Profs. José Bassalo and Paulo Alencar, from UFPa, for the suggestions for graduate studies in Experimental High Energy Physics at LAFEX/CBPF.

To my parents and brothers, for all the comprehension and endless support, essential to my stay in this research career, so difficult and also so depreciated in Brazil.

To my wife Gabriella, my eternal girlfriend and inseparable companion, whose love, fondness, patience and comprehension has made my life much happier. Her help with the figures and final lay-out of this thesis has soothed the finalization task.

Finally, I acknowledge the financial support to this work from CAPES and CNPq.

Abstract

We present the first measurement of $d\sigma^\mu/dp_{T_\mu}$, the inclusive differential production cross section of forward muons in proton-antiproton collisions at $\sqrt{s} = 1.8$ TeV, for the pseudorapidity range $2.2 < |\eta| < 3.3$. This is an important measurement, from a region of overwhelming combinatoric background. Our analysis is based on a 3700 muons data sample, collected in dedicated runs of the DØ detector, corresponding to 32 nb^{-1} of integrated luminosity. We observe some disagreement between our results and the outcome of a detailed simulation of muon production, based on ISAJET model for heavy quark production and their semileptonic decays.

Index

1	Introduction	1
1.1	Generalities	2
2	Theory	5
2.1	The Standard Model	5
2.2	Bottom Quark Production Mechanisms	8
2.2.1	The Strong Coupling Constant	9
2.2.2	The Parton-Parton Cross Sections	11
2.2.3	The Proton Structure	14
2.3	The Theoretical Predictions	16
2.4	Monte Carlo Simulation of Physical Processes	16
2.5	Motivations to this Work	22
3	DØ Experiment	23
3.1	The Beams	23
3.2	The DØ Spectrometer	26
3.2.1	The Central Detector	29
3.2.2	The Calorimeters	35
3.2.3	The Muon System	41
3.3	Data Acquisition and Trigger Systems	47
3.3.1	Level 0 Trigger	48
3.3.2	Level 1 Trigger	50

3.3.3	Level 2 Trigger	55
3.3.4	Data Acquisition System	55
3.3.5	Monitoring System	57
3.4	Data Processing	57
3.4.1	Utilities	57
3.4.2	Event Reconstruction	60
3.4.3	Monte Carlo Simulation	61
3.4.4	Trigger Simulation	62
3.4.5	Off-line Analysis Packages	63
4	Data Analysis	64
4.1	The Simulation of Forward Muons	64
4.2	On-line Event Selection	65
4.3	Off-line Event Selection	67
4.4	Efficiencies	72
4.4.1	Fiducial Cut on Detection Efficiency	76
4.5	Backgrounds	80
4.6	The Experimental Spectrum	83
4.7	Momentum Resolution	85
4.8	Systematical Error Analysis	89
4.9	Results	91
5	Conclusions	94

List of Figures

2.1	The strong coupling constant, $\alpha_s(\mu)$	10
2.2	Feynman diagrams for the production of heavy flavors in LO QCD	11
2.3	Feynman diagrams for the production of heavy flavors in NLO QCD	13
2.4	Some parameterizations for gluon distribution functions inside the nucleon	15
2.5	NLO QCD predictions for the bottom production cross section	17
2.6	Theoretical expectations and experimental data for $d\sigma^\mu/dp_{T_\mu}$ ($ \eta < 0.8$)	20
2.7	Theoretical expectations for $d\sigma^\mu/dp_{T_\mu}$ in the forward region ($2.2 < \eta < 3.3$)	21
3.1	The accelerator complex at Fermilab	24
3.2	Isometric view of the DØ spectrometer	28
3.3	Longitudinal view of Central Detector	29
3.4	Transversal cut of a quadrant in the Vertex Chamber	30
3.5	End view of some cells of the Transition Radiation Detector	32
3.6	End view of some cells of the Central Drift Chamber	33
3.7	View of the Forward Drift Chambers	35
3.8	Isometric view of the calorimeters	37
3.9	The calorimeter segmentation	38
3.10	End view of the Central Calorimeter	38
3.11	Schematic view of the DØ muon detection system	42
3.12	Side view of the DØ detector, showing the elements of the muon detection system	43
3.13	End view of a WAMUS chamber	43
3.14	Cathode pads in WAMUS PDT's	44

3.15	Geometry of SAMUS stations	46
3.16	Simplified diagrams of the trigger system at DØ	48
3.17	The scintillator hodoscopes of Level 0 Trigger	49
3.18	Block diagram of the muon trigger system	51
3.19	Block diagram of the Level 1 Muon Trigger	52
3.20	The <i>Software</i> of Data Acquisition System	56
3.21	Side view of a $t\bar{t}$ candidate, as seen by the DØ detector	59
4.1	Illustration of reconstruction algorithm for SAMUS muon tracks	67
4.2	Some distributions for collected events	68
4.3	Comparison for number of hits on a muon track	69
4.4	Comparison between the energy deposited in hadronic calorimeters	70
4.5	Comparison of χ^2 distributions for muon tracks in SAMUS	71
4.6	Some muon distributions after muon-id cuts	72
4.7	Estimation procedure used for the efficiency of N_{hits} cut	74
4.8	Spatial dependence of $\varepsilon_{\text{Trig.Reco}}$, for different combinations of muon momentum and electrical charge	75
4.9	$\varepsilon_{\text{Trig.Reco}}$ distributions for muon candidates after off-line cuts	76
4.10	Acceptance of the fiducial cut	78
4.11	Cross section variations as a function of the value chosen for the fiducial cut	79
4.12	Background estimation based on the energy deposited in the hadronic calorimeters	81
4.13	Background estimation based on the number of hits along the muon track	82
4.14	The experimental spectrum $d\sigma^\mu/dp_{T_\mu}\Delta\eta$	84
4.15	The muon momentum resolution in SAMUS region	86
4.16	Result of the correction procedure for muon momentum resolution	88
4.17	Experimental spectrum of the differential inclusive muon production cross section in the kinematical region $2.2 < \eta < 3.3$	93

List of Tables

2.1	Main properties of leptons	6
2.2	Main properties of quarks	7
2.3	Main properties of gauge bosons	7
2.4	Relevant parameters for indirect decays in ISAJET model	20
3.1	Main characteristics of the Vertex Chamber	31
3.2	Main characteristics of the Transition Radiation Detector	32
3.3	Main characteristics of the Central Drift Chamber	34
3.4	Main characteristics of the Central Calorimeter	39
3.5	Main characteristics of the Endcap Calorimeters	40
3.6	Main characteristics of the WAMUS System	45
3.7	Main characteristics of the SAMUS system	47
4.1	Average number of muons per nb^{-1} of integrated luminosity	68
4.2	Efficiency estimation for many selection criteria	74
4.3	Fitted values for the three free parameters used in the procedure for muon momentum resolution correction	87
4.4	Analysis of systematical errors before momentum resolution correction	90
4.5	Total systematical errors, after the momentum resolution correction	91
4.6	Numerical values for $d\sigma^\mu/dp_{T\mu}\Delta\eta$ in the kinematical region $2.2 < \eta_\mu < 3.3$	92

Chapter 1

Introduction

This work presents results obtained in the analysis of data collected by the DØ spectrometer, with the purpose of extracting the inclusive muon production cross section in the kinematical region

$$\begin{aligned} 1 \text{ GeV}/c < p_{T_\mu} < 30 \text{ GeV}/c \\ 2.2 < |\eta_\mu| < 3.3 \end{aligned} \tag{1.1}$$

The analysis and results described are fruit of the collaboration of LAFEX (Laboratório de Cosmologia e Física Experimental de Altas Energias) group with the DØ Collaboration, in the study of $p\bar{p}$ collisions at energies of 1.8 TeV. As a member of this collaboration, we spent two years at Fermilab, working on the first run of the DØ spectrometer. Back to Rio de Janeiro, we could complete this thesis making use of the powerful computing system at LAFEX.

This thesis is subdivided into five chapters. In this first chapter we try to locate our research subject in the context of High Energy Physics, enumerating the main motivations of heavy flavor physics. The second chapter deals with the theoretical expectations of heavy quark production in hadronic collisions, and bottom quark production in particular.

The third chapter brings a superficial description of the experimental apparatus, the DØ detector used in the data collection, along with the main software packages employed in the data processing, including the Monte Carlo simulation. In section 3.3 the muon trigger system is described in some more details, as LAFEX group gave a significant contribution for its development, in both software and hardware. As we shall see later, the muon trigger at small angles was essential for the present analysis.

The central part of the thesis, the data analysis, is described in details in the fourth chapter.

In the fourth chapter, central part of this thesis, we discuss in depth all the

procedures involved in the statistical treatment of the collected data, with the purpose of extracting the inclusive muon production cross section. The main results are presented at the end of this chapter.

Finally, in the fifth and last chapter we point out some conclusions reached from our results.

1.1 Generalities

The heavy flavor physics is one of today's most active research fields in high energy physics. By heavy flavor we mean quarks c , b and t (charm, bottom and top respectively), which are called heavy because their masses lie above the theoretical parameter Λ_{QCD} (see chapter 2). This fact allows us to treat these three quarks according to the framework of perturbative QCD, which is the best theory known for strong nuclear interactions.

The precise study of the properties of heavy quarks requires us to produce such quarks in large amounts, through high energy collisions between sub-atomic particles. One long known source of such energetic particles is cosmic radiation. However, such particles come to earth in extremely low rates, and this makes them less useful in most current scientific experiments, as these are generally based on an enormous number of collisions.

An alternative approach consists in *fabricating* the energetic sub-atomic particles in laboratory, by using gigantic particle accelerators. This approach is more suitable for use in scientific experiments, because such artificially accelerated particles are much more abundant and controllable by the experimentalist.

Worthy of note is the fact that each of the heavy flavors has remarkable characteristics, which significantly distinguish them from each other, from both theoretical and experimental point of view.

The charm discovery, in November 1974^[1, 2], marked the beginning of the heavy flavor physics, and gave support to the quark hypothesis, suggested by Gell-Mann and Zweig some years before. The charm was the first quark flavor to be predicted prior to its discovery. Experimentally, the development of silicon vertex detectors with excellent spatial resolution, capable of resolving the charm production and decay vertices in fixed target experiments¹, allowed very pure charm samples to be extracted^[3, 4, 5, 6], and most charm properties were then accurately measured. Nowadays, with the study of rare processes like doubly Cabibbo-suppressed decays^[7, 8], flavor changing neutral currents^[9, 10, 11] or precision measurements of $D^0 - \overline{D}^0$ oscillations, charm physics still raises great interest, for it is a good laboratory for the study of physical processes in the validity threshold of perturbative QCD.

¹Fixed target experiments are discussed in Chapter 3.

Bottom quark was discovered in 1977^[12], but the study of its properties took much longer than for the charm quark, due to experimental details. In first place, the minimum energy of 10 GeV needed to produce $b\bar{b}$ pairs makes it difficult to use fixed target arrangements for bottom production. Also, even when bottom quarks are produced in such arrangements, they tend to have very low momentum in the laboratory frame, therefore the experimental technique of distinguishing production and decay vertices, used to extract charm signal, is not helpful for the case of bottom quarks.

From the theoretical point of view, the bottom quark discovery brought with it the perturbation of a certain order established after the charm discovery and its accommodation in the Standard Model scheme of weak isospin doublets. To restore the order we need to assume the existence of a sixth quark, called top quark, which together with the bottom quark would compose a new weak isospin doublet. Today's confidence in the Standard Model is so strong that nobody would doubt that the top quark exists, despite of the several experimental failures over about 18 years of intense search^[13, 14, 15, 16]. The recent observation of the top quark^[17, 18] confirmed what everybody expected and, more than this, gave even more support to the Standard Model, the current theory describing the interactions between the fundamental particles of nature.

The study of heavy flavor production and decay provides quantitative tests to some of the main predictions of the Standard Model. The more we know about the properties of known particles, more precise will be the theoretical predictions of new phenomena, guiding therefore the experimental work aiming for the discovery or study of such new phenomena.

The purpose of the present work is to measure the inclusive muon production cross section in the forward region, $2.2 < |\eta| < 3.3$ ². From the fact that about 10% of bottom quarks decays semileptonically into muons, our results can be extended to provide an estimation of the bottom production cross section (σ_b). However this extension requires a detailed simulation of the decay $b \rightarrow \mu X$, and depends strongly on the simulation model used. This extension is not treated in the present work, and is left for the near term future.

On a further level, the measurement of σ_b in the forward region can be used as a constraint for the gluon distribution function for the proton, as the hadronic production of heavy flavors is sensitive to the presence of partons with $x \sim O(10^{-3})$, where x is the fraction of the proton's longitudinal momentum carried by the parton which takes part in the fundamental interaction of the proton-antiproton collision. The parton distribution functions will be discussed in more details in Chapter 2.

Finally we would like to emphasize that we will frequently use in the present work, as in any analysis in experimental high energy physics, expressions like “real events” and “Monte Carlo events”. We want to clarify that the extraction of a significant signal

²In the case of DØ experiment, the kinematical region $2.2 < |\eta| < 3.3$ corresponds to angles between 4° and 12° from beam line. This is the origin of the expression “small angles”, extensively used throughout this thesis

frequently follows a comparative study with its simulation. This methodology is currently part of any data analysis. Real events are the ones actually produced in nature, therefore they are the actual objects of the methodology used and the source of our results.

Chapter 2

Theory

In the previous chapter we briefly described some of the main features of the heavy quarks.

To go any deeper into the discussion of heavy flavors requires some knowledge about the Standard Model. In this chapter we discuss the main features of the Standard Model, emphasizing the topics relevant to bottom quark production mechanisms. There is also a quick description of the ISAJET model, used in our analysis for the simulation of heavy flavor production and decays.

2.1 The Standard Model

Elementary Particle Physics is the branch of Physics which deals with the fundamental interactions of nature, which act between the building blocks of all matter. We call Standard Model to the set of theories which best describe most of the experimental results existing so far. With no doubt, the Standard Model is today one of the physics theories most precisely tested in laboratory, and some of its predictions match experimental measurements with accuracy better than one part per million¹.

According to the Standard Model, all matter existing in the universe is composed of twelve different kinds of elementary fermions and their antiparticles. These elementary fermions are separated into two groups of three families each.

$$\begin{array}{l} \text{Leptons} \\ \text{Quarks} \end{array} \quad \begin{pmatrix} \nu_e \\ e \end{pmatrix} \quad \begin{pmatrix} \nu_\mu \\ \mu \end{pmatrix} \quad \begin{pmatrix} \nu_\tau \\ \tau \end{pmatrix} \\ \begin{pmatrix} u \\ d \end{pmatrix} \quad \begin{pmatrix} c \\ s \end{pmatrix} \quad \begin{pmatrix} t \\ b \end{pmatrix}$$

¹See, for instance, [20, p. 162]

In the group of leptons we find the electron (e), the muon (μ) and the tau (τ), each one associated to its partner neutrino (ν). In the other group we find the quarks *up* (u), *down* (d), *strange* (s), *charm* (c), *bottom* (b) and *top* (t).

All kinds of matter around us, is composed only by the quarks and leptons from the first family: atomic physics successfully describes matter in terms of atoms, which are composed of electrons revolving around a heavy nucleus, and the nucleus being responsible for the atomic mass. On their turn, the nuclei are described by nuclear physics as being composed of protons and neutrons. Finally, elementary particle physics describes protons and neutrons as being composed of quarks u and d . The electron neutrino, ν_e , is present among the products of nuclear β decay of some unstable nuclei, and also in the neutron decay.

All other elementary fermions can only be produced in collisions of energetic particles, from cosmic radiation or from particle accelerators. The present work deals with the production properties of one of these elementary fermions, the bottom quark, produced in collisions of protons and antiprotons at energies of 1.8 TeV.

Quarks and leptons interact through four kinds of forces (or interactions): strong, weak, electromagnetic and gravitational interactions. These interactions are *transmitted* (or mediated) by a different kind of elementary particles, collectively called *gauge bosons*. Each interaction acts upon matter with a characteristic intensity, represented by a *coupling constant*.

Tabs. 2.1-2.3 show the main properties of elementary fermions and gauge bosons.

The fundamental interactions can be described through the so called *Gauge Field Theories*, constructed with appropriate symmetries which describe all allowed and forbidden couplings for each interaction. As examples of such theories, we mention Quantum Electrodynamics (QED) which describes electromagnetic interactions, and Quantum Chromodynamics (QCD) which describes strong interaction.

lepton	electrical		mass [MeV/c ²]	decay lifetime [s]	Interactions		
	charge [e]	spin			strong	weak	electro- magnetic
ν_e	0	1/2	$< 17 \times 10^{-6}$	stable	no	yes	no
e	-1	1/2	0.5110	stable	no	yes	yes
ν_μ	0	1/2	< 0.27	stable	no	yes	no
μ	-1	1/2	105.7	2.20×10^{-6}	no	yes	yes
ν_τ	0	1/2	< 35	stable	no	yes	no
τ	-1	1/2	1784	3.03×10^{-13}	no	yes	yes

Table 2.1: Main properties of leptons (Adapted from [19]).

quark	electrical		mass [MeV/c ²]	mean life [s]	Interactions		
	charge [e]	spin			strong	weak	electro- magnetic
<i>d</i>	-1/3	1/2	~ 0.3	stable	yes	yes	yes
<i>u</i>	2/3	1/2	~ 0.3	stable	yes	yes	yes
<i>s</i>	-1/3	1/2	~ 0.5	~ 10 ⁻¹⁰	yes	yes	yes
<i>c</i>	2/3	1/2	~ 1.5	~ 10 ⁻¹²	yes	yes	yes
<i>b</i>	-1/3	1/2	~ 4.7	~ 10 ⁻¹²	yes	yes	yes
<i>t</i>	2/3	1/2	~ 200	?	yes	yes	yes

Table 2.2: Main properties of quarks (Adapted from [19]).

Interaction	Interaction carriers				Typical coupling constant
	name	symbol	spin	mass [GeV/c ²]	
Strong	gluon	<i>g</i>	1	0	~ 0.1 - 1
Weak	weak vector boson	<i>W</i> [±]	1	80.22	~ 1/30 at energies ~ <i>M_W</i>
		<i>Z</i>	1	91.19	
Electromagnetic	photon	<i>γ</i>	1	0	1/137
Gravitational	graviton	<i>g</i>	2	0	~ 10 ⁻³⁸

Table 2.3: Main properties of gauge bosons, carriers of fundamental interactions (Adapted from [19]).

Another example of gauge field theory is the so called *Electroweak Theory* (or Weinberg-Salam-Glashow Theory), which describes weak and electromagnetic interactions as different manifestations of a single fundamental interaction, called *electroweak interaction*, present in processes in high energies ($E \sim M_W = 80.22 \text{ GeV}/c^2$ or higher).

The Standard Model is basically built from a combination of QCD with Electroweak Theory, therefore it is able to describe nature in terms of its elementary building blocks, leptons and quarks, and the fundamental interactions among those. A detailed description of the sophisticated framework of Standard Model is beyond our purposes. One can find it in a vast literature, including many nice textbooks^[20, 21, 22, 23]. In the present work we are restricted to discuss only those topics directly related to our topic, namely bottom quark production².

²Actually the same basic formalism described in Section 2.2 can be used in the calculation for the production of any heavy flavor.

2.2 Bottom Quark Production Mechanisms

Bottom quarks are copiously produced in pairs in hadronic collisions through strong interactions between the elementary components of colliding hadrons, provided that this fundamental process has energy above the $b\bar{b}$ production threshold. This threshold is about 10 GeV.

According to the Standard Model, the cross section for hadronic production of heavy flavors, $\sigma(AB \rightarrow Q\bar{Q}X)$, can be calculated taking into account the fact that hadrons are composed of quarks, antiquarks and gluons, all them collectively called *partons*. Mathematically:

$$d\sigma(s, m_Q) = \sum_{ij} \int dx_A dx_B d\hat{\sigma}(\hat{s}, m_Q) F_i^A(x_A) F_j^B(x_B) \quad (2.1)$$

where \sqrt{s} is the energy in the $A + B$ center of momentum frame, m_Q is mass of the quark Q , F_i^A are called *parton distribution functions*, and represent the probability that a parton of type i be found inside hadron A with momentum p_i lying between $x_A p_A$ and $(x_A + dx_A)p_A$, p_A is the momentum of hadron A and $d\hat{\sigma}(\hat{s}, m_Q)$ is the partonic cross section corresponding to the fundamental process $ij \rightarrow Q\bar{Q}X$, with an effective energy $\hat{s} = x_A x_B s$.

For the development of Eq. 2.1 one usually uses the formalism of perturbative QCD, which consists in expanding the unknown quantities in infinite power series, in terms of the coupling constant α_s :

$$d\hat{\sigma}_{ij}(\hat{s}, m_Q) = \alpha_s^2(\mu_1) G_{ij}^{LO}(\hat{s}, m_Q) + \alpha_s^3(\mu_1) G_{ij}^{NLO}(\hat{s}, m_Q) + \dots \quad (2.2)$$

$$F_i^A(x_A) = C_i^{A,LO}(x_A, \mu_2) + \alpha_s(\mu_2) C_i^{A,NLO}(x_A, \mu_2) + \dots \quad (2.3)$$

where functions G_{ij} and C_i and constants μ_1 and μ_2 depend upon the procedure chosen for the expansion, and hence have some arbitrament in their definition. Constants μ_1 and μ_2 are the renormalization and factorization scales respectively, and for the sake of simplicity, are usually made equal, $\mu_1 = \mu_2 = \mu$. The indices LO and NLO indicate terms of order α_s^2 (Leading Order) and of order α_s^3 (Next to Leading Order) respectively.

The quantities $d\hat{\sigma}$ and F_i^A must not depend upon the arbitrary scale μ , as they correspond to physical observables. However, if the power series is truncated, there is a residual dependence with the scale. This dependence can be taken as an indication about the convergence of the series, and hence the necessity of taking into account higher order terms.

As any infinite power series, the lower α_s is, the faster is the convergence of the expansions above. Thus, when $\alpha_s \ll 1$ one can truncate the infinite series to some order, e.g. α_s^3 , and the residual dependence on the arbitrary scale μ tells us whether the truncated series is close to the convergence of the infinite series. A strong dependence with μ indicates that higher order terms need to be taken into account for a better result.

Now let us take for discussion each piece of the cross section calculation, as seen in Eq. 2.1.

2.2.1 The Strong Coupling Constant

In gauge field theories, the coupling constants depend on Q , the 4-vector momentum transfer of the fundamental process. One thus usually expresses $\alpha_s(\mu)$ for any scale μ in terms of its value $\alpha_s(\mu_0)$ calculated for a fixed scale $\mu_0 = Q_0$, called *renormalization scale*^[21]. The variation of $\alpha_s(\mu)$ with the scale μ is described by the renormalization group equation:

$$\frac{\partial \alpha_s(\mu)}{\partial \ln \mu^2} = -b \alpha_s^2(\mu) [1 + b' \alpha_s(\mu) + O(\alpha_s^2)] \quad (2.4)$$

where

$$b = \frac{33 - 2N_{\text{lf}}}{12\pi} \quad \text{e} \quad b' = \frac{153 - 19N_{\text{lf}}}{2\pi(33 - 2N_{\text{lf}})} \quad (2.5)$$

and N_{lf} is the number of light flavors (one usually takes as light the quark flavors q such that $m_q < \mu$). In lowest order (LO), the solution of Eq. 2.4 is:

$$\alpha_s(\mu) = \frac{\alpha_s(\mu_0)}{1 + b \alpha_s(\mu_0) \ln(\mu^2/\mu_0^2)} \quad (2.6)$$

and in NLO:

$$\frac{1}{\alpha_s(\mu)} - \frac{1}{\alpha_s(\mu_0)} + b' \ln \left(\frac{\alpha_s(\mu)}{\alpha_s(\mu_0)} \frac{1 + b' \alpha_s(\mu_0)}{1 + b' \alpha_s(\mu)} \right) = b \ln(\mu^2/\mu_0^2) \quad (2.7)$$

Note that one can always obtain the LO expression from the NLO expression, just setting $b' = 0$. Then, from now on, we deal only with the NLO expressions.

The expression above allows us to calculate the strong coupling constant from its value in any fixed scale, μ_0 . One usually rewrites $\alpha_s(\mu)$ in terms of Λ_{QCD} , which is defined using the Beta function $\beta(x)$:

$$\ln \frac{\mu^2}{\Lambda_{\text{QCD}}^2} = - \int_{\alpha_s(\mu)}^{\infty} \frac{dx}{\beta(x)} \quad (2.8)$$

and one finds:

$$\alpha_s(\mu) = \frac{1}{b \ln(\mu^2/\Lambda_{\text{QCD}}^2)} \left[1 - \frac{b'}{b} \frac{\ln \ln(\mu^2/\Lambda_{\text{QCD}}^2)}{\ln(\mu^2/\Lambda_{\text{QCD}}^2)} \right] \quad (2.9)$$

This expression, which is shown graphically in Fig. 2.1, shows us that the strong coupling constant α_s increases as $\mu \rightarrow 0$ ($Q \rightarrow 0$, or large distances), contrary to the behavior of α , the electromagnetic coupling constant. This means that an infinite energy would be needed to isolate quarks or gluons from a bound state. Therefore, quarks and gluons cannot exist in nature as free particles. They are always bound into color singlet states, called hadrons, of which protons and neutrons are familiar examples. This feature of QCD is known as *confinement*. Note that in the regime of confinement, $\alpha_s > 1$, so there is no sense in using the perturbative approach, used in Eqs. 2.2 and 2.3.

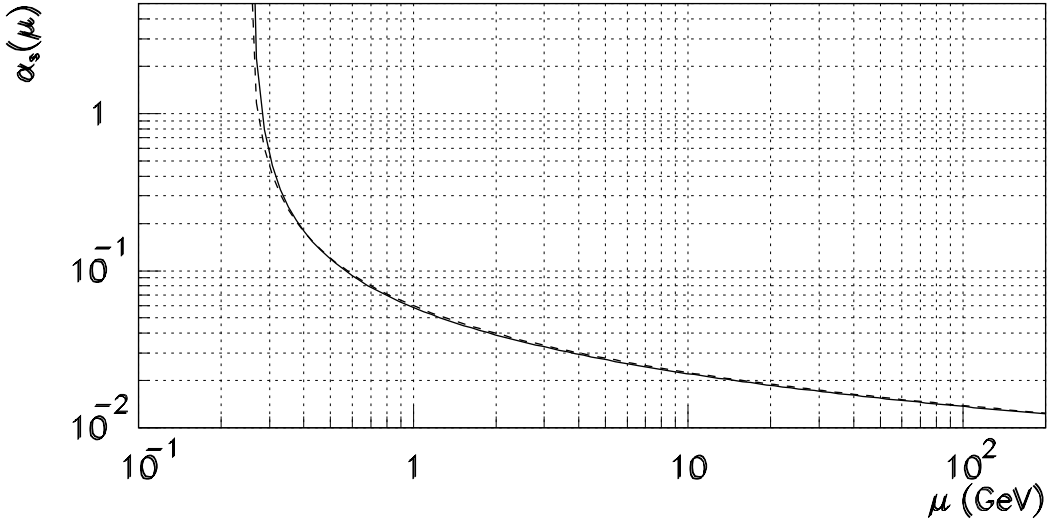


Figure 2.1: The strong coupling constant $\alpha_s(\mu)$ (Eq. 2.9), for $N_f = 5$ and $\Lambda_{\text{QCD}} = 250$ MeV. The dashed line represents $\alpha_s(\mu)$ for $b' = 0$.

On the other hand, $\alpha_s \rightarrow 0$ as $\mu \rightarrow \infty$ ($Q \rightarrow \infty$, or short distances), and one can consider quarks and gluons as effectively free particles. One labels this regime as *asymptotic freedom*, and in this regime one can safely use the perturbative approach, as for instance to calculate the heavy flavor production cross section.

2.2.2 The Parton-Parton Cross Sections

In Eq. 2.2 we expanded the parton-parton cross sections in powers of the strong coupling constant, α_s . The mathematical framework involved in these calculations is very sophisticated, then we are restricted to only describe the main results in order LO. To NLO, the complexity of the expressions is much higher, then we will only show some of the contributing diagrams and show the results graphically.

Leading Order Diagrams

In Leading Order QCD, $O(\alpha_s^2)$, heavy flavor quarks can be produced through two mechanisms:

$$q(p_1) + \bar{q}(p_2) \rightarrow Q(k_3) + \bar{Q}(k_4) \quad (2.10)$$

$$g(p_1) + g(p_2) \rightarrow Q(k_3) + \bar{Q}(k_4) \quad (2.11)$$

respectively called *quark-antiquark annihilation* and *gluon fusion*.

The matrix elements for these processes are calculated using the Feynman diagrams depicted in Fig. 2.2. After averaging (summing) over spins and colors of the initial (final) states, one finds^[24]:

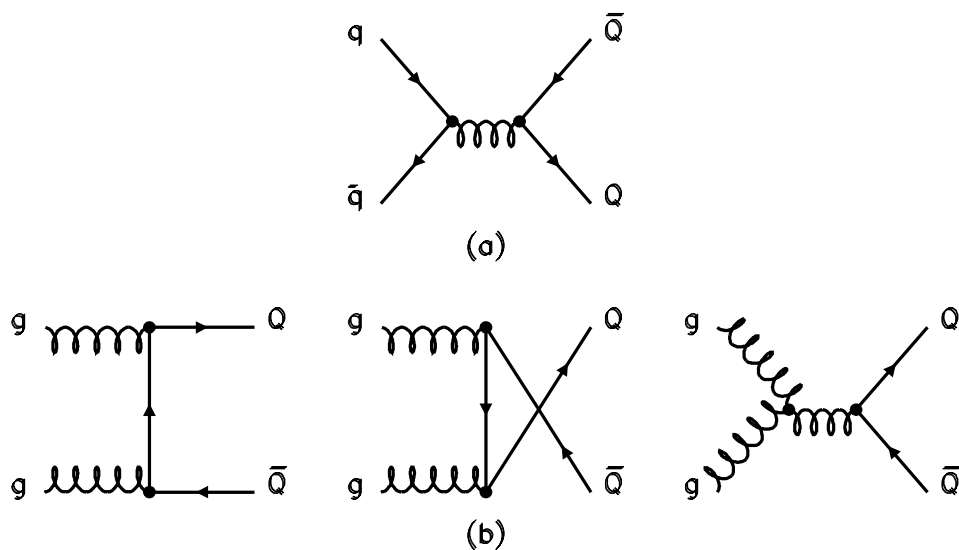


Figure 2.2: Feynman diagrams for the processes of heavy flavor production in LO QCD (flavor creation). (a) quark-antiquark annihilation. (b) Gluon fusion.

$$\sum |\overline{\mathcal{M}}_{q\bar{q}}|^2 = \frac{4\alpha_s^2}{9} \left(\tau_1^2 + \tau_2^2 + \frac{\rho}{2} \right) \quad (2.12)$$

$$\sum |\overline{\mathcal{M}}_{gg}|^2 = \frac{\alpha_s^2}{8} \left(\frac{4}{3\tau_1\tau_2} - 3 \right) \left(\tau_1^2 + \tau_2^2 + \rho - \frac{\rho^2}{4\tau_1\tau_2} \right) \quad (2.13)$$

where the dimensionless terms $\tau_{1,2}$ and ρ are given by:

$$\tau_1 = \frac{2p_1 \cdot k_3}{\hat{s}} = \frac{m_Q^2 - \hat{t}}{\hat{s}}, \quad \tau_2 = \frac{2p_1 \cdot k_4}{\hat{s}} = \frac{m_Q^2 - \hat{u}}{\hat{s}}, \quad \rho = \frac{4m_Q^2}{\hat{s}} \quad (2.14)$$

and one uses the Mandelstan variables for the partonic process:

$$\hat{s} = (p_1 + p_2)^2, \quad \hat{t} = (p_1 - k_3)^2, \quad \hat{u} = (p_1 - k_4)^2 \quad (2.15)$$

Then the cross section $d\hat{\sigma}_{ij}$ of the partonic process is given by:

$$d\hat{\sigma}_{ij} = \frac{1}{2\hat{s}} \frac{d^3k_3}{E_3} \frac{d^3k_4}{E_4} \delta^4(p_1 + p_2 - k_3 - k_4) \sum |\overline{\mathcal{M}}_{ij}|^2 \quad (2.16)$$

which can be rewritten in terms of the transverse momentum ($\vec{k}_t = \vec{k}_{t_3} = \vec{k}_{t_4}$) and rapidity (y) as:

$$\frac{d\hat{\sigma}_{ij}}{dy_3 dy_4 d^2k_t} = \frac{1}{4(m_Q^2 + k_t^2)^2 [1 + \cosh(y_3 - y_4)]^2} \sum |\overline{\mathcal{M}}_{ij}|^2 \quad (2.17)$$

From the expression above it is possible to show that the cross section for hadronic production of heavy flavors decreases sharply with the increase of $y_3 - y_4$ and k_t , and that these quarks have in general transverse momentum of order of m_Q .

One should also note that the quarks produced in LO mechanisms necessarily have same transverse momentum, in opposite azimuth angles, in a back-to-back configuration in order to conserve energy and momentum.

Next to Leading Order Diagrams

The contributions to heavy quark production due to NLO diagrams ($O(\alpha_s^3)$) were recently calculated^[25, 26]. Some typical NLO QCD diagrams used are shown in Fig. 2.3.

The heavy flavor production mechanisms in NLO are:

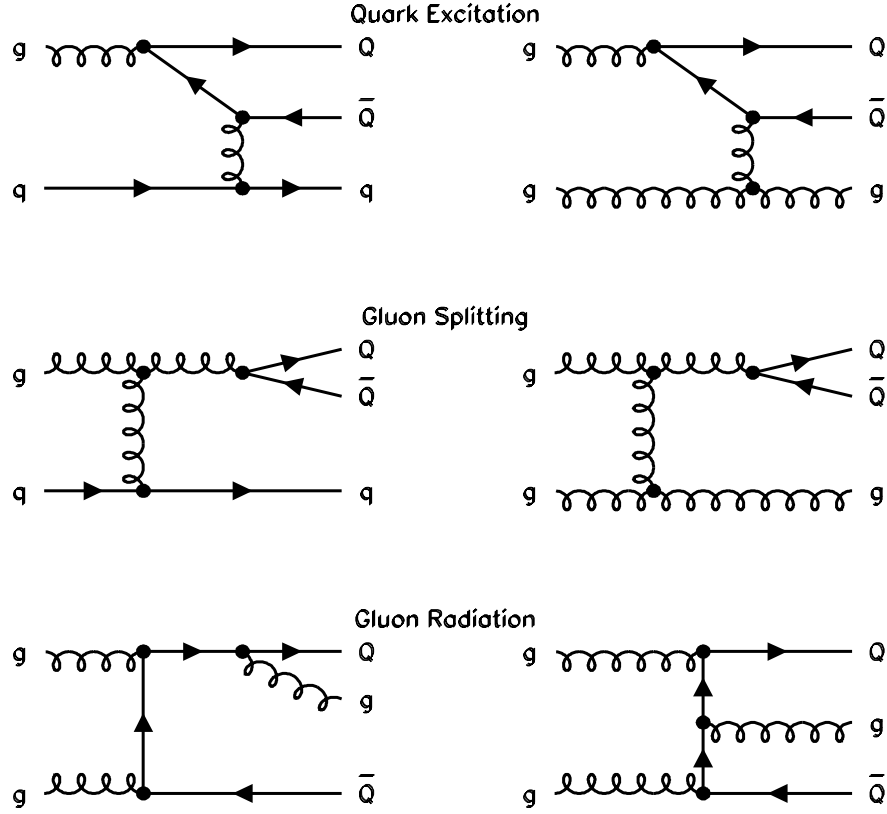


Figure 2.3: Some typical Feynman diagrams for the production of heavy flavors in NLO QCD.

$$\begin{aligned}
 q(p_1) + \bar{q}(p_2) &\rightarrow Q(k_3) + \bar{Q}(k_4) + g(k_5) \\
 g(p_1) + g(p_2) &\rightarrow Q(k_3) + \bar{Q}(k_4) + g(k_5) \\
 g(p_1) + q(p_2) &\rightarrow Q(k_3) + \bar{Q}(k_4) + q(k_5) \\
 g(p_1) + \bar{q}(p_2) &\rightarrow Q(k_3) + \bar{Q}(k_4) + \bar{q}(k_5)
 \end{aligned}
 \tag{2.18}$$

All the calculations are done in a similar fashion to the LO calculation, described in the previous section. However, the final expressions are too complex, and will not be shown here. It is not trivial to extract the informations we want from them anyway.

It is important to emphasize that the NLO diagrams can generate very different topologies for the $Q\bar{Q}$ pair, as compared to the back to back configuration of LO diagrams. This is due to the third parton emerging from the hard process, which participates in the energy-momentum balance. This is particularly true in the gluon splitting diagrams, where the heavy quarks emerge almost collinear.

An important conclusion one reaches in comparing the results for partonic LO and NLO cross sections is that the process $gg \rightarrow gg$ is much more important than

$gg \rightarrow Q\bar{Q}$:

$$\frac{\sigma(gg \rightarrow gg)}{\sigma(gg \rightarrow Q\bar{Q})} \sim 100 \quad (2.19)$$

but it only contributes to the heavy flavor production at NLO level, through gluon splitting processes (see Fig. 2.3). This is the main reason why the NLO contribution for heavy flavor production is quantitatively as important as that from LO processes, despite of being suppressed by one more strong coupling vertex than LO processes. This suppression is compensated by the large probability to find gluons inside the proton, favoring $gg \rightarrow gg$ diagrams which cannot produce heavy quarks in LO QCD.

This does not mean, however, that going one order higher ($O(\alpha_s^4)$, or NNLO), one will find also contributions of the same order as NLO QCD. NNLO diagrams should not produce any diagrams significantly different from those already seen in NLO. Hence one believes that NLO QCD calculations, mentioned above, should provide theoretical predictions sufficiently close to the physical heavy quark production cross sections. There should be no need to take into account higher order processes.

2.2.3 The Proton Structure

Now that one knows the partonic cross sections for production of heavy flavors, one needs to take a last step to obtain the cross sections for hadronic production of heavy quarks. One needs to consider the fact that protons are not elementary particles, but it is instead composed of elementary quarks.

Experimentally, the main source of informations about the structure of nucleons is the process of *Deep Inelastic Scattering* (DIS) of leptons off nuclear targets. The mathematical treatment of such processes is done with the help of structure functions. These are adequately parametrized functions included in the calculation of physical quantities, which are used to fit the experimental data.

On the other hand, the parton model describes hadrons as dynamical systems composed of quarks and gluons, where each particular type i of parton is associated to a probabilistic function $F_i^A(x)$, called *parton distribution function*. As mentioned earlier, the parton distribution functions represent the probability that one finds a parton of momentum lying between $x_A p_A$ and $(x_A + dx_A)p_A$ inside hadron A , of momentum p_A .

Similarly to α_s , the parton distribution functions also depend on the energy scale involved, *mu* *fac*, called *factorization scale*. This dependence is described by the Altarelli-Parisi equations^[27].

It is important to note that the study of hadronic structure using lepton scatterings does not provide direct information about the gluon structure of the hadrons, as there is no coupling between leptons and gluons, according to the Standard Model. The

information about gluons is indirectly obtained through the missing momentum needed to the quarks momenta to add up to hadron momenta. From this one concludes that about 50% of proton momentum is carried by gluons. This indirect determination of the gluon structure function, $G(x, \mu)$, is subject to large uncertainties, and thus it is responsible for a large source of uncertainties in any theoretical predictions involving hadrons. The indirect study of $G(x, \mu)$ requires experimental data on strong interactions involving gluons in the initial state, and that means hadron-hadron scatterings. Unfortunately, these data on hadronic processes usually come together with large error bars.

There is a large number of parameterizations for the gluon distribution functions inside the proton. A representative set of such parameterizations^[28] is shown in Fig. 2.4.

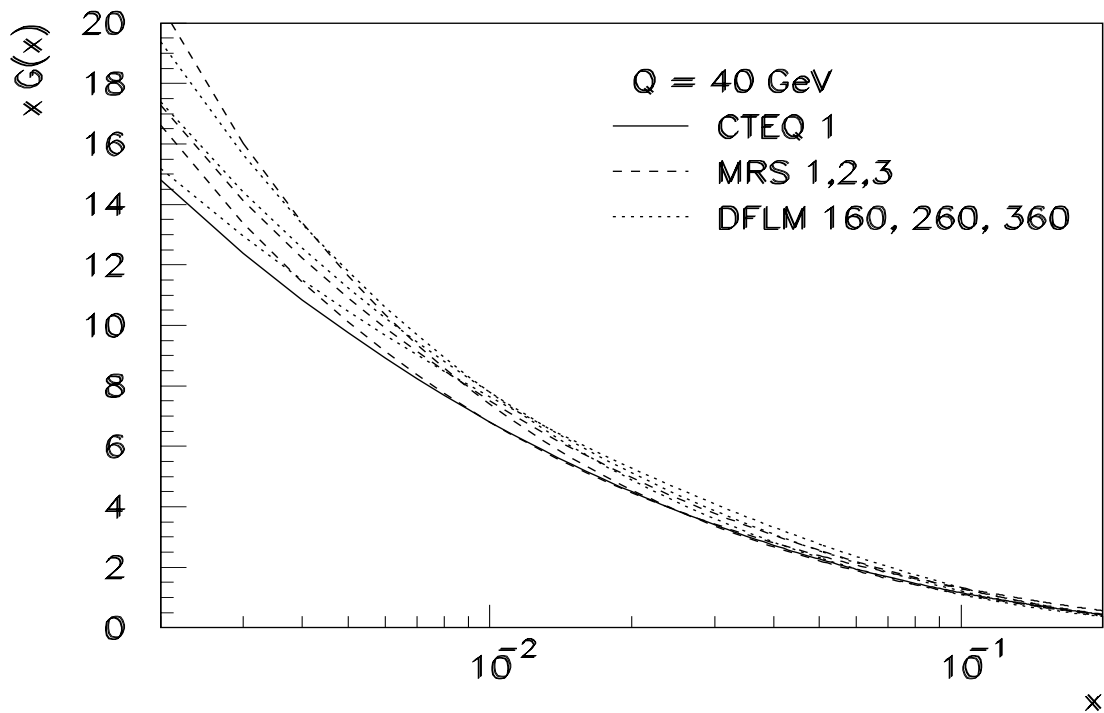


Figure 2.4: Some of the main parameterizations for the momentum distribution of gluons inside a nucleon, $xG(x)$, at a scale $Q = 40$ GeV, as a function of x , the fraction of the nucleon momentum carried by the gluons.

2.3 The Theoretical Predictions

Now that one has in hands all the pieces needed to the calculations of $\sigma(AB \rightarrow Q\bar{Q}X)$, these pieces can finally be combined according to Eq. 2.1. In practice this is usually done using numerical methods.

The results will be shown graphically, with the help of a computer software containing the differential expression of the cross section for production of heavy flavor quark-antiquark pairs. The software is written by Mangano, Nason and Ridolfi, and it is based on their calculations in NLO QCD.

Fig. 2.5 shows the theoretical expectations for the inclusive bottom quark production cross section, as a function of transverse momentum and rapidity. To make this plot we used CTEQ parameterization^[29] for parton distribution functions, and also the following parameters: the mass of the bottom quark, $m_b = 4.75 \text{ GeV}/c^2$, renormalization and factorization scales $\mu_{\text{ren}} = \mu_{\text{fac}} = \mu = \sqrt{m_b^2 + p_T^2}$, and $\Lambda_{\overline{MS}}^5 = 152 \text{ MeV}$.

In Fig. 2.5(b) one can see, as a solid line, the bottom production cross section in the forward region, defined as $2.2 < |y| < 3.3$, which is indirectly linked to the results of this thesis, as muonic decays of heavy flavors is one of the main sources of muons in the forward region.

2.4 Monte Carlo Simulation of Physical Processes

The experimental observation of heavy quarks is not made directly, because as we mentioned earlier, it is not possible to observe free quarks in nature. Although not demonstrated so far, this fact seems to be due to the color confinement property of QCD.

As soon as it is produced, the bottom quark combines to other lighter quarks, forming a color singlet state (hadron), which is most of the time a B meson. This process is called *hadronization*.

Although these hadrons can be directly observed, this is not what usually happens, because the heavy quark quickly decays into lighter, more stable states. This decay follows the exponential law of radioactive decays. In the case of bottom quarks, its decay lifetime is about 1 ps, as shown in Tab. 2.2.

The semileptonic decays of heavy quarks, $Q \rightarrow \ell^\pm X$, are particularly interesting to the heavy flavor physics, because the observation of leptons is experimentally simpler, thus simplifying the tagging of heavy quark decays. In this work we perform a measurement of the inclusive muon production cross section in $p\bar{p}$ collisions, and one notes that part of such muons come from bottom quark decays.

Therefore we need to translate the bottom quark production cross section, which calculation was described in the previous sections, into muon cross sections, as

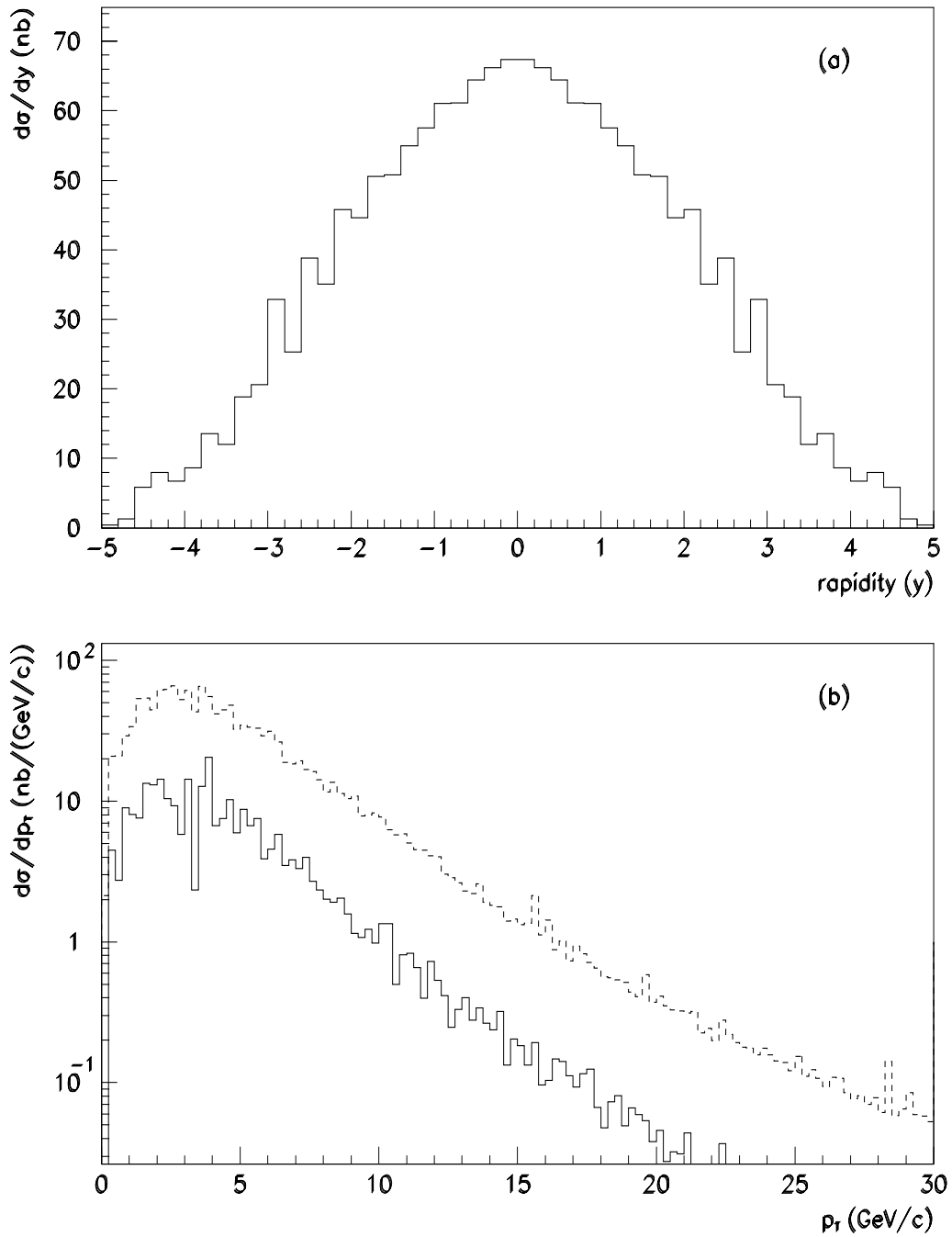


Figure 2.5: NLO QCD predictions for the bottom quark production cross section (see text for more details). (a) Dependence on rapidity. (b) Dependence on transverse momentum. The solid line represents $2.2 < |y| < 3.3$, while the dashed line represents $|y| < 5$.

muons are the particles we actually observe in our detector.

Once there are no exact analytical expressions to relate quarks and muons, one has to rely on simplified models for the several steps involved between hadron collision and muon detection. The steps involved are basically the following:

- An appropriate parameterization for partonic cross sections and for parton distribution functions, both discussed earlier. With these we can calculate the effective hadron-hadron cross sections, $\sigma(AB \rightarrow b\bar{b}X)$;
- The hadronization of all partons, i.e. those directly involved in the hard scattering, and also those which are merely spectators of the hard process;
- Decays of short lived hadrons;
- All effects and details involved in the muon detection.

With the purpose of combining all these effects, we make use of Monte Carlo techniques^[30]. There are some very known models, encompassing one or more of the steps above. Among such models we can mention: ISAJET^[31], HERWIG^[32], Vecbos^[33] and Pythia^[34]. Each model is more adequate for a given class of physical processes. The ISAJET model, extensively used in the present work, will be discussed in details in the next subsection.

The ISAJET Model

In the present work we use the ISAJET model^[31] for the simulation of the physical processes involved in the production, hadronization and decay of bottom quarks produced in $p\bar{p}$ collisions. More than a tool for the prediction of inclusive muon production cross sections, needed to compare our experimental results to theoretical expectations, ISAJET model can also be used as event generator, keeping all the kinematical information of each particle produced in simulated collisions, allowing us to process these particles through the detector simulation software packages (more on this at chapter 3).

The event generation process in ISAJET can be split into three stages. The first stage simulates the hard scattering itself, for which contribute all matrix elements of the kind $2 \text{ partons} \rightarrow 2 \text{ partons}$, including $gg \rightarrow gg$. Initial state heavy quarks can also contribute, as virtual partons coming from the splitting of any gluons inside the proton. The partonic cross sections are convoluted with a parameterization for the parton distribution functions, and one obtains the hadron-hadron cross section corresponding to the generated process. This hadron-hadron cross section is used later as a weight, to normalize the whole generated sample in terms of the absolute cross sections. Then the initial and final partons can radiate hard gluons, according to Altarelli-Parisi equations, as

a means of approximating the higher order radiative corrections. In our analysis we used the CTEQ^[29] parameterizations for the parton distribution functions inside the proton.

The second stage is the process of hadronization of the quarks and gluons emerging from the scattering and radiation processes just mentioned. In ISAJET, a quark q of momentum p_q combines with a light antiquark \bar{q}' forming a hadron $q\bar{q}'$ with a momentum zp_q , where z is defined by:

$$z = \frac{E^{\text{had}} + p_{\parallel}^{\text{had}}}{E^q + p^q} \quad (2.20)$$

where $p_{\parallel}^{\text{had}}$ is the hadron momentum in the original direction of quark q . For the hadronization of light quarks and gluons, z is randomly generated according to the distribution:

$$f(z) = 1 - a + a(b + 1)(1 - z)^b \quad (2.21)$$

where a and b are parameters fitted to experimental data. For heavy quarks, z is generated according to the Peterson fragmentation model^[35]:

$$f(z) = \frac{1}{z[1 - 1/z - \epsilon_Q/(1 - z)]^2} \quad (2.22)$$

where the parameter ϵ_Q is different for each heavy quark flavor, in order to agree with experimental data for heavy quarks produced in e^+e^- colliders.

Finally, the third and last stage deals with the decays of short lived particles, which are formed in the hadronization process, but decay into lighter particles before they can be detected. This is the case for all hadrons composed of heavy quarks.

The relevant decays are, in our case, the semileptonic decays of B mesons, producing muons in the final state. We can distinguish two cases: Direct decays (or first generation), such as $B \rightarrow \mu\nu X$, and indirect decays (or second generation), such as $B \rightarrow DX$, followed by $D \rightarrow \mu\nu X$.

For direct decays, the ISAJET model does not distinguish the light valence quark, partner of the bottom quark in the B meson, and assigns to all B mesons the same semileptonic branching ratio $Br(B \rightarrow \ell\nu X) = 12\%$. Note that the corresponding experimental value is $(10.3 \pm 0.5)\%$ ^[36], suggesting that small corrections need to be introduced in the cross sections involving direct semileptonic decays.

For indirect decays, besides the semileptonic branching ratios of charmed particles, it is important also to check the fraction of each charmed meson among the decay products of the B meson. These are shown together with the semileptonic branching ratios for each charmed meson in Tab. 2.4. These inclusive semileptonic branching ra-

Charmed Hadron (D_i)	ISAJET model		Experiment	
	f_i	$Br(D_i \rightarrow \mu\nu X)$	f_i	$Br(D_i \rightarrow \mu\nu X)$
D^0	0.49	0.075	0.54 ± 0.06	0.100 ± 0.026
D^\pm	0.24	0.170	0.26 ± 0.04	-
D_s	0.17	0.065	0.089 ± 0.011	-
c -baryon	0.10	0.075	0.064 ± 0.011	-

Table 2.4: ISAJET parameters relevant for indirect decays. f_i is the fraction of each charmed meson among the decay products of B mesons, including decays like $B \rightarrow D^* X \rightarrow DX$.

tios are not well known experimentally, and this fact also introduces uncertainties to the theoretical expectations calculated using the ISAJET model.

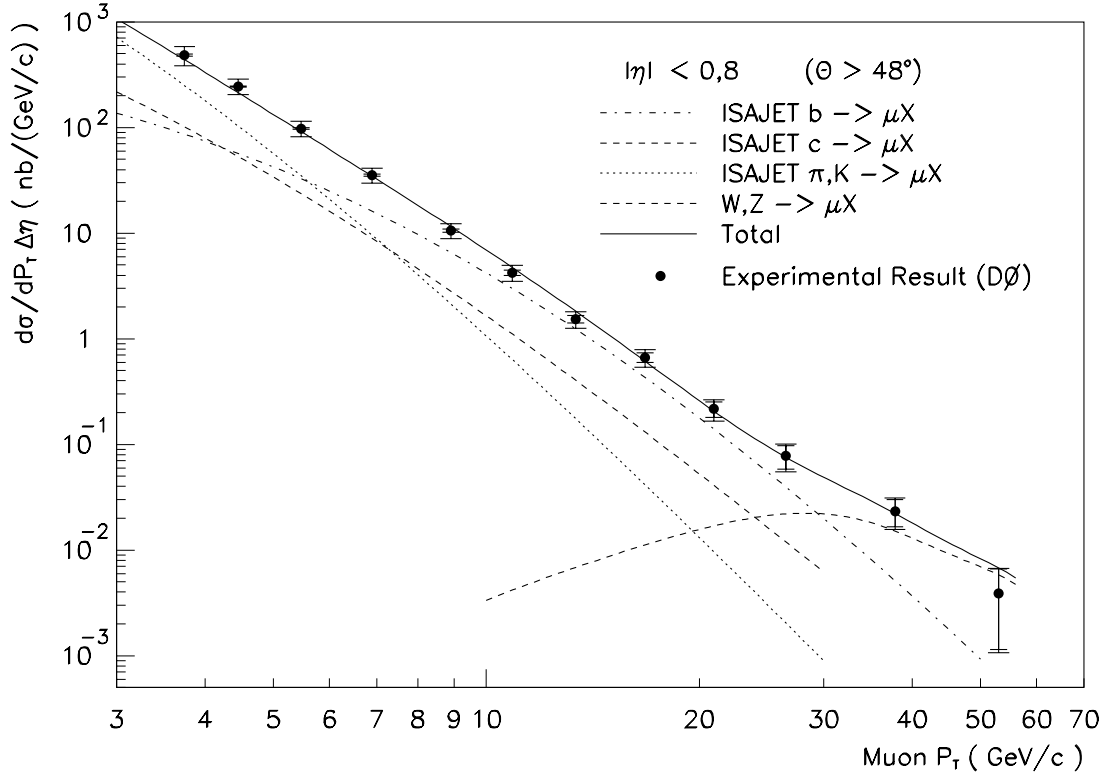


Figure 2.6: Theoretical expectations for the inclusive muon production cross section in the central region ($|\eta| < 0.8$) based on the ISAJET NLO model for the simulation of physical processes, and comparison with experimental results^[37].

Despite all theoretical uncertainties associated with the several steps involved, ISAJET is still the best existing model for the simulation of processes of production and decay of heavy flavor quarks. Fig. 2.6 shows the result of a detailed simulation in ISAJET model using a NLO QCD approximation, generating $p\bar{p} \rightarrow b\bar{b}X$ and $p\bar{p} \rightarrow c\bar{c}X$ events, where at least one of these heavy quarks decayed into one or more muons. Indirect decays $B \rightarrow DX \rightarrow \mu\nu X$ are considered part of the sample $p\bar{p} \rightarrow b\bar{b}X$. Note that, to simplify the

direct comparison between the results in different ranges of pseudorapidity, the results are presented as $d\sigma^\mu/dp_{T\mu}\Delta\eta$.

The experimental points^[37], obtained from the analysis of data collected by the DØ spectrometer in the region $|\eta| < 0.8$, show an excellent agreement with the ISAJET expectations. This agreement gives us some confidence that, at least in the central region, ISAJET model provides a satisfactory description of heavy quark production mechanisms.

Finally, in Fig. 2.7 one can see the theoretical predictions for the muon production cross section in the forward region (defined by $2.2 < |\eta| < 3.3$), for muons coming from bottom and charm quark decays. These predictions are based on the ISAJET NLO model for the production and decays of heavy flavor quarks.

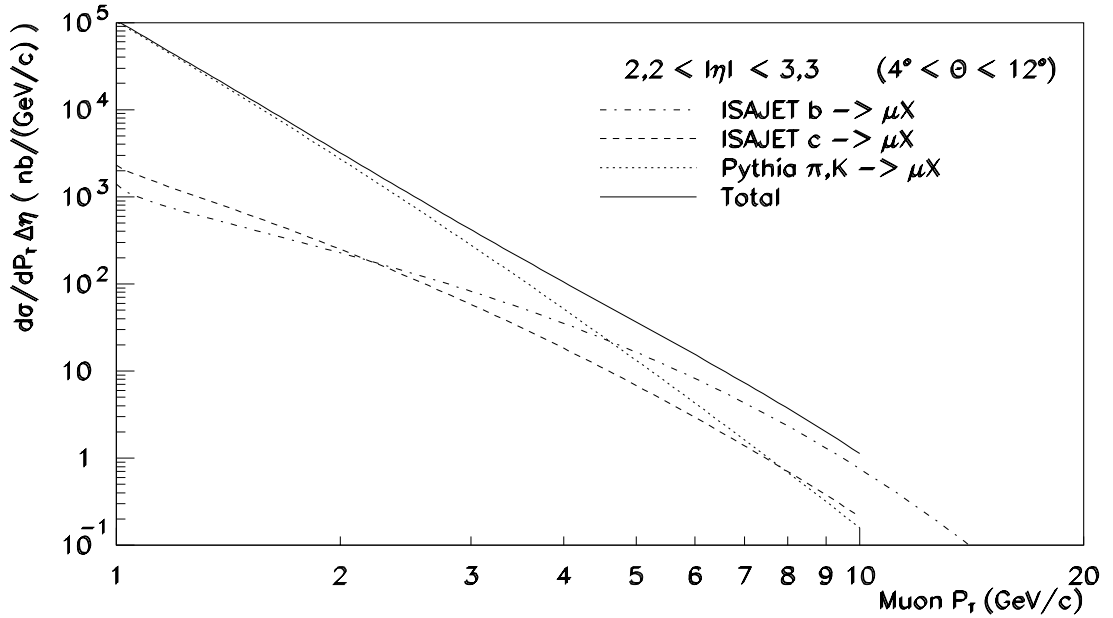


Figure 2.7: Theoretical expectations for the inclusive muon production cross section in the forward region ($2.2 < |\eta| < 3.3$) based on the ISAJET NLO model for the simulation of physical processes.

Fig. 2.7 also shows, as a dotted line, the result of another model, Pythia^[34], for the simulation of muons in the forward region, due to in-flight decays of charged pions and kaons, $\pi, K \rightarrow \mu X$. The solid line represent the sum of these four different contributions, i.e. muons coming from from light (pions and kaons) and also heavy quark decays. One must not forget that the theoretical uncertainties associated to the several theoretical parameters, as well as to the various parameterizations existing for the parton distribution functions inside the nucleon, shall be taken into account when comparing these theoretical predictions with our experimental results. These uncertainties, estimated to be about 25% for the central region, reaches about 40% in the forward region.

Another source of muons also studied, to check a possible contribution in the high- p_T region, was the Drell-Yan mechanism (production of virtual photons or weak vector bosons and their subsequent decays into muons). The simulation, based again on ISAJET model, pointed to a contribution of few pb/GeV for muons in the forward region, flat in the range 5 to 4 GeV/c. It is thus too small compared to the contributions from heavy quark decays, for muon transverse momenta below 30 GeV/c.

2.5 Motivations to this Work

The forward region of hadronic colliders is an extremely problematic region for data analysis, mainly due to the proximity of hadronic beams. This region is vulnerable not only to the hadron jets from spectator partons, but also to the hadronic beam halo itself. The extraction of a physics result in such a highly noisy region is a very interesting measurement in itself.

In our case, the excellent geometrical coverage of the DØ muon system allows, in principle, for the measurement of the pseudorapidity dependence of the bottom quark production cross section. However, as we shall see in chapter 3, the complete range of geometrical coverage in DØ spectrometer involves the observation of muons in four regions which are very different among them³. Each of these regions requires its own analysis, completely independent from other regions, taking into account its particularities. It is thus interesting to compare the experimental measurements obtained in each of these regions and check whether all results are compatible. Unfortunately this comparison could not be done so far, as due to many technical problems, the two intermediate regions still had not provided good quality data available for analysis.

Finally, it is important to note that despite the excellent agreement between theoretical expectations and experimental results in the central region ($|\eta| < 0.8$), we found in chapter 4 a small discrepancy between our experimental results and the theoretical expectations shown in Fig. 2.7. Such discrepancy may mean, for instance, that the parameterizations for gluon distribution functions inside the proton used in the ISAJET simulation are not appropriate, and maybe should be replaced by some other, more adequate parameterization. As mentioned in section 2.2.3, there is no direct experimental information about the gluon structure of the proton. Thus the possibility that the experimental measurement of the bottom quark production cross section in the forward region can provide more direct information about $G(x)$ in the proton for $x \sim O(10^{-3})$ is also an important motivation for the present analysis.

³As we shall see later, in chapter 3, the four regions mentioned here are WAMUS CF, WAMUS EF, SAMUS-WAMUS overlap and SAMUS.

Chapter 3

DØ Experiment

In this chapter we describe the experimental apparatus used in the present work. In a first part we briefly discuss the production of hadronic beams of protons and antiprotons, each of them with an energy of about 900 GeV. These beams are forced to collide head-on to produce the new particles we want to observe.

In a second part we describe how the particles produced in such head-on collisions are detected and studied, with the operation of the so-called **DØ spectrometer**. The main guidelines of the detector project and its component subdetectors will be discussed. Emphasis is given to the description of the Level 1 Muon Trigger system, in which development stage our group gave a significant contribution, particularly in the forward region. The performance of this system was essential for the present work.

This chapter is concluded with a brief description of all the data processing stages, except that part specific to our analysis, which is left to the next chapter.

3.1 The Beams

Fermilab is today the laboratory where one finds the highest energy subatomic particles in the world, thanks to the **Tevatron**, a synchrotron with about 6.28 km of circumference. Inside the Tevatron, protons and antiprotons can be accelerated to energies of up to 1000 GeV, and then kept in almost circular orbits by the action of magnetic fields produced in liquid helium cooled superconducting magnets.

Before being injected into the Tevatron, protons and antiprotons go over several pre-accelerating stages, which will soon be described. A simplified scheme of the Fermilab accelerator complex is shown in Fig. 3.1.

Tevatron can be operated in two different modes: **fixed target** and **collider**. In fixed target mode, after acceleration, protons are extracted and distributed among

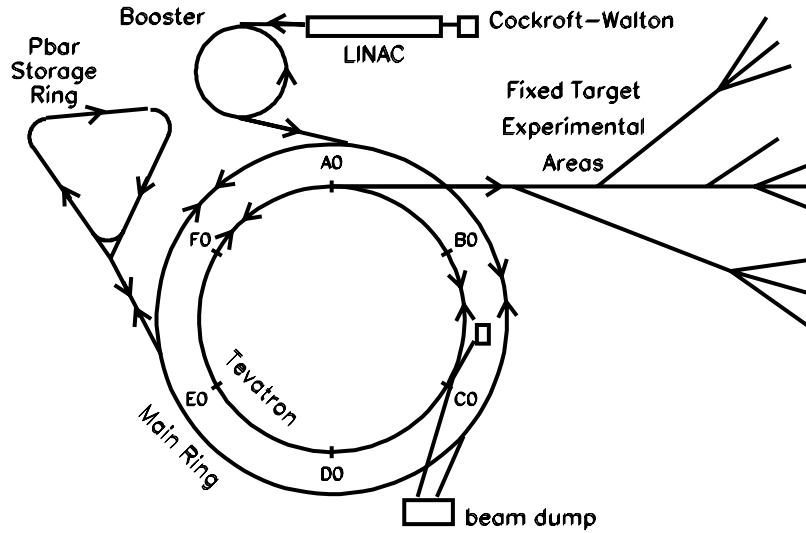


Figure 3.1: The accelerator complex at Fermilab. Tevatron and Main Ring have, actually, the same diameter and are located one above the other, in the same tunnel.

many experimental areas, as shown in Fig. 3.1, where they in general collide with stationary targets and produce new particles, to be studied using different experimental techniques.

In collider mode, used in our experiment, protons are used in a first stage for antiproton production. As they are produced, the antiprotons are continuously *stacked* in the Accumulator Ring, until reaching at least some hundred billions of antiprotons. Then, protons and antiprotons are injected in opposite directions into the Tevatron, for a last accelerating stage, and then forced to collide head-on. Such collisions release up to 2 TeV of energy.

When comparing fixed target and collider modes, with respect to beam production and also the detection of the particles produced in the collisions, we face many difficulties inherent to the collider mode, like:

- the technical difficulty of keeping two counter-rotating beams in the same accelerator tunnel.
- a smaller interaction rate in collider mode, as it replaces the target with another beam, necessarily rarefied.
- collisions are spatially spread, as they are not restricted to target dimensions.
- the produced particles and its decay products are well distributed over 4π of solid angle, as the laboratory frame coincides with the center of momentum frame. Therefore, a large geometrical acceptance requires much larger detectors, which surrounds the interaction region almost completely. This fact makes collider detectors much more expensive than those for fixed target mode.

On the other hand, collider mode provides us collisions with much higher energies than in fixed target mode, allowing us to explore energy regimes which today are technically impossible for fixed target mode. As a comparison, in Tevatron conditions we can produce collisions with energies of up to 43 GeV in fixed target modes, against 2 TeV in collider mode. Therefore collider mode must be used whenever highest possible energy is desirable. Note that 43 GeV pN is the highest energy experimentally available today in fixed target mode.

The preliminary accelerating stages are common to both operating modes: in a first stage, H_2 molecules are injected in an electrostatic field and ionized by an electron beam. H^- ions are accelerated by the electrostatic field to 750 keV, and directed to a 200 m long linear accelerator (LINAC). The LINAC strips off the electrons and accelerates resulting protons to 200 MeV by RF waves, which groups protons together in bunches, forming a pulsed beam.

In the following stage the bunches go into the **booster**, a synchrotron accelerator with final energy of 8 GeV, and are later injected into the **Main Ring**.

From the Main Ring, protons can be used:

- For the production of antiprotons. For this purpose protons are extracted from the Main Ring at 120 GeV and collide with a metal target. Among the large number of particles produced, antiprotons with energies of about 8 GeV are filtered and directed into the Accumulator Ring, where they are continuously stored until reaching few hundred billions of antiprotons. This amount is necessary to setup a new cycle of $p\bar{p}$ collisions, called *store*, which can last in average 24 hours. The Main Ring operates in this antiproton production mode in parallel to the stores, with the purpose of getting larger and larger stacks of antiprotons, for highest possible luminosities to be reached in the following store.
- As a pre-accelerator stage to the Tevatron. In this case protons from the booster (or antiprotons from the Accumulator Ring) are injected into the Main Ring at 8 GeV and then accelerated to 150 GeV, and then injected into the Tevatron. This operation mode is used just for a few times, once for bunch, during the shot setup.

During a shot setup, six equidistant bunches of protons are injected into the Tevatron, and then six equidistant bunches of antiprotons are injected in the opposite direction. Then these bunches are accelerated up to energies of 900 GeV.

There are six points on the Tevatron where it is possible to promote proton-antiproton collisions. These points are labeled A0, B0 ... F0. In two of these points large detectors were built, with the purpose of studying the outcome of $p\bar{p}$ collisions: CDF (*Collider Detector Facility*) is located at B0, and DØ detector is located at the point with same name. It should be noted that the trajectories of protons and antiprotons inside Tevatron are actually helicoidal, such that B0 and D0 are the only points where there

is a significant collision rate. Eventually other detectors could be built in other points, and then the trajectories would be adjusted, to permit collisions to occur in these other points.

In next section we describe the $D\bar{O}$ spectrometer, whose data we used in our analysis.

3.2 The $D\bar{O}$ Spectrometer

With the purpose of studying proton-antiproton collisions at energies of 2 TeV, the $D\bar{O}$ experiment was approved in 1983, and $D\bar{O}$'s design report was concluded a year later^[38]. Subatomic processes with so high energies had never been obtained in laboratory at that time, therefore there were big expectations that new phenomena would show up to this apparatus.

The $D\bar{O}$ detector design was optimized keeping in mind three main objectives:

- Provide excellent identification and energy measurement for electrons and muons, as one expects that new phenomena generally have large branching fractions into final states with one or more leptons. On the other hand, those processes typical of QCD, which are much more frequent, have comparatively lower semileptonic branching fractions.
- Allow the observation of parton jets with excellent energy resolution. Emphasis was given to the observation of parton jets instead of the individual particles, because the jets as a whole are more directly related to the fundamental processes occurring in a high energy collision than each isolated particle.
- Provide a good measurement of \cancel{E}_T , the missing energy necessary to transverse energy-momentum balance, as an indirect means of detecting neutrinos and other neutral particles with low interaction rate with matter.

From the above features, a final design project was reached with the following characteristics:

- Hermetic, thick (large number of radiation lengths), compact (small volume), radiation hard and finely segmented calorimetry, based in liquid argon ionization detection. The fine segmentation provides optimum spatial resolution of jets, allowing the study of its shape and evolution. Hermeticity favors neutrino detection through determination of missing energy. Calorimeters are also compact, so that muon chambers can be as close as possible to the interaction region, and thick, to minimize the punchthrough probability.

- Hermetic muon detection, with thick iron magnets for muon momentum measurement. These magnets also serve as absorbers for punchthrough and hadronic leakage into the muon system.
- Non-magnetic, compact tracking system, with emphasis in the suppression of background to electrons through a two-track resolution able to identify e^+e^- pairs from high energy photon conversion.

Fig. 3.2 shows an isometric view of the DØ spectrometer, where one sees the many concentric layers of its component subdetectors – **central detector**, **calorimeters** and **muon chambers**, which we will describe in the following subsections. A platform supports the detector components, keeps them in position, and also allows the whole system to be moved into and out of the collision hall. The platform also holds many components of fast trigger and signal processing electronics.

The electrical cabling coming from the several detection channels go over an articulated bridge to the *Moving Counting House* (MCH). The MCH holds the rest of the trigger and signal processing electronics, keeping these components far from the high radiation environment of the detector platform. The digitized electronic signals from MCH are collected, compressed and sent to a data acquisition farm, which composes the last trigger stage, performing event building and filtering tasks. Select events are sent to special processing nodes for on-line monitoring and storing in magnetic media. A small fraction of these kept events, those particularly interesting from a physics point of view, are directly sent to a special processing farm, the **Express Line**, where these potentially good events are immediately reconstructed and kept on disk, easily available to data analysis.

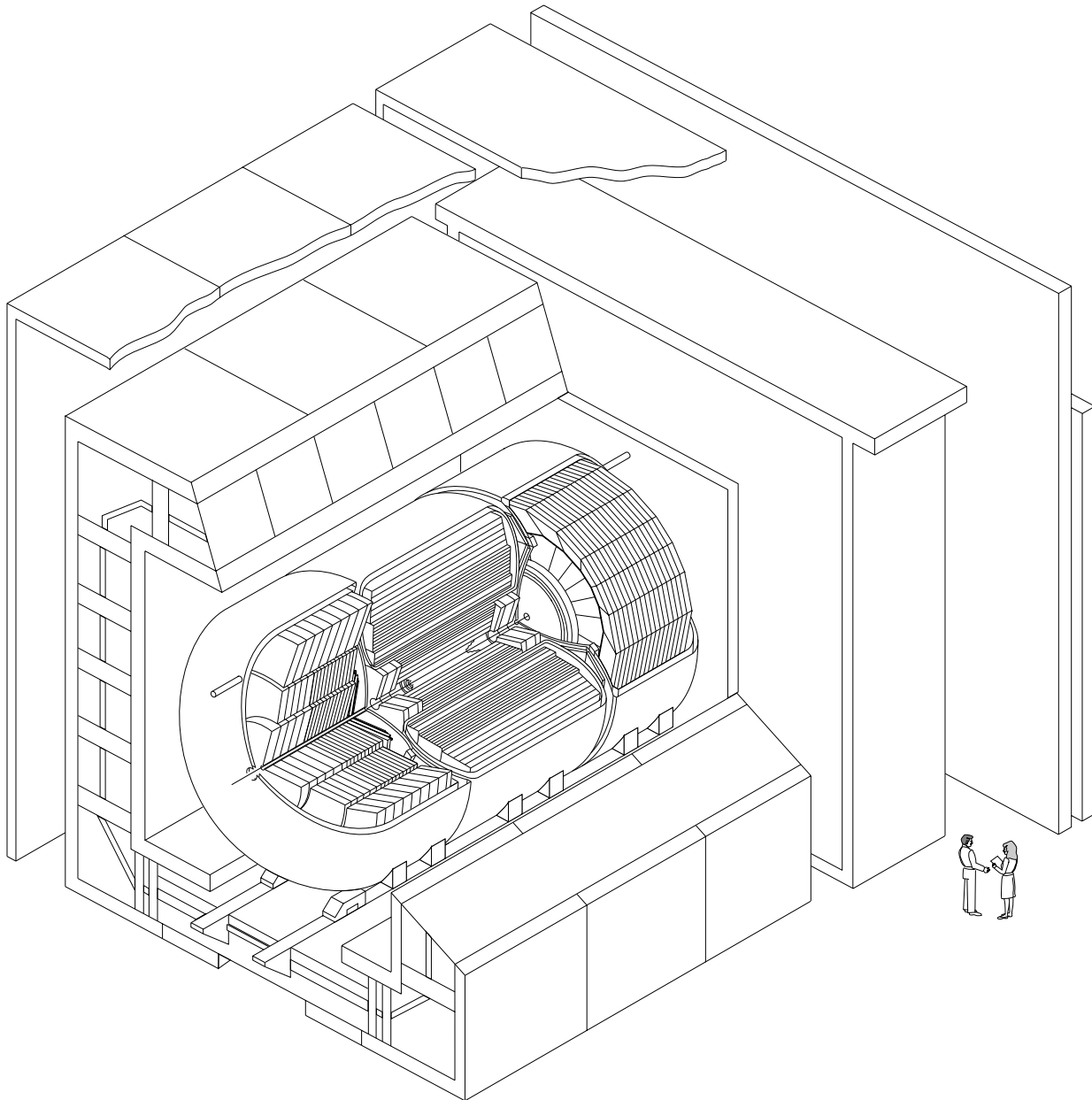
A detailed description of the DØ spectrometer can be found in Ref. [39]. In the following subsections we briefly describe the many component subdetectors, as extracted from the aforementioned paper. There are also two subsections dedicated to the Level 1 Muon Trigger, and to describe the contributions from LAFEX group, in both hardware and software, for the development of this important system.

The DØ global coordinate system is a right-handed one, with z -axis pointing into proton direction (from north to south), and y -axis upright.

In the following subsections we mention the geometrical coverage of each sub-detector in terms of the pseudorapidity (η), which is univocally defined as a function of the polar angle θ as:

$$\eta = -\ln\left(\tan\frac{\theta}{2}\right) \quad (3.1)$$

Pseudorapidity is a convenient approximation, in the limit $m/E \rightarrow 0$, of the real rapidity of a particle, $y = 1/2 \ln(E + p_z)/(E - p_z)$. Note that $\eta = 0$ for $\theta = 90^\circ$, and η is symmetrically negative in north side and positive in south side of the detector.



$D\bar{D}$ Detector

Figure 3.2: Isometric view of the $D\bar{D}$ spectrometer, with a cut showing the relative position of its component subdetectors.

3.2.1 The Central Detector

The Central Detector (CD) was designed with the purpose of tracking the charged particles coming from the $p\bar{p}$ collisions. It is subdivided in four subdetectors: the **Vertex Chamber (VTX)**, the **Transition Radiation Detector (TRD)**, the **Central Drift Chamber (CDC)** and the **Forward Drift Chambers (FDC)**. The first three subdetectors cover the central region, and they form concentric shells around the beam pipe, as shown in Fig. 3.3. The FDC's cover the small angle regions, so they are placed perpendicularly to the beam pipe, like caps for the other three subdetectors. The whole arrangement fits inside the calorimeters, in a cylindrical volume 270 cm long and with radius of 78 cm, free of magnetic fields and centered in the nominal collision point (center of the detector).

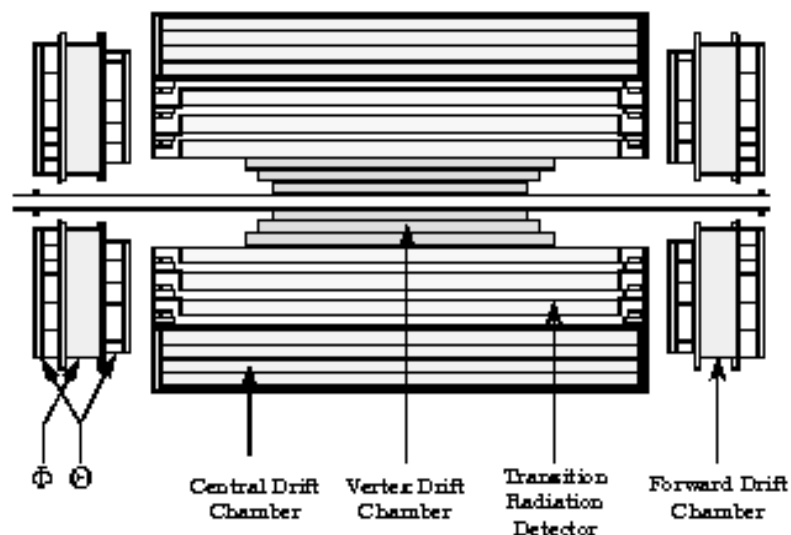


Figure 3.3: Longitudinal view of the Central Detector, showing the relative position of each component subdetector.

The design of CD subdetectors took into consideration the absence of magnetic field in the tracking, and emphasized the capability of resolving two neighbor tracks, to distinguish an individual electron from an e^+e^- pair from the decay of a high energy photon, where the tracks emerge very closely. The spatial resolution, optimized for the measurement of primary vertex position and for the matching of a CD track to a calorimeter tower, was designed to be better than 1 mm. The TRD was designed to provide a rejection factor of 50 for pions, in addition to the rejection from the calorimeter alone.

A deeper discussion on these and other design features of the central detector can be found in the $D\bar{O}$ Design Report^[38]. The design requirements could be fully

reached, as one can see briefly in the following sections for each subdetector. For more details, refs. [38] and [39] should be consulted.

The Vertex Chamber (VTX)

The VTX is the innermost detector in $D\bar{O}$, placed just outside the beam pipe. Its main purposes are the accurate tracking of charged particles, for determination of primary and secondary vertices. The VTX provides also a veto for photons which convert inside the TRD, as these do not leave tracks in the VTX.

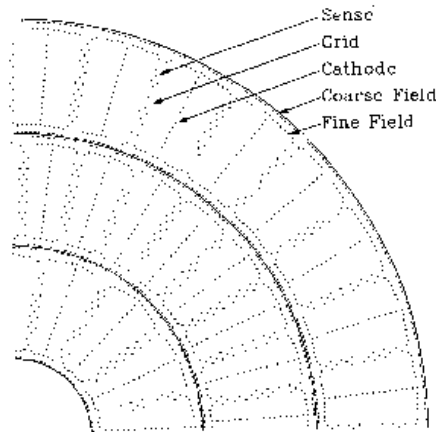


Figure 3.4: Transversal cut of a quadrant in the vertex chamber (VTX), showing the sense wires and the potential wires.

As one can see from Fig. 3.4, the VTX is composed of three concentric layers. The two outermost layers are subdivided into 32 cells, while the innermost layer has 16 cells. Cells from neighbor layers are misaligned in ϕ to simplify the pattern recognition. Each cell has 8 longitudinal sense wires, placed radially inside the cell. The sense wires collect electrons from the ionized gas molecules. To help solving left-right ambiguities, adjacent sense wires are slightly misaligned in $\pm 100\mu\text{m}$.

The electrostatic field inside the cell, which drives electrons to the sense wires, are shaped by cathode wires and by the grounded grid wires. A good knowledge of the electrostatic field inside the cell is essential to determine the drift velocity of the electrons to the sense wires, and therefore to reconstruct the trajectory of the ionizing particles.

The VTX performance was analyzed in test beams^[39]. We measured a typical spatial resolution of $50\mu\text{m}$, with an efficiency above 90% for resolving two neighbor tracks with a separation between them of at least 0.6 mm. Tab. 3.1 lists the main characteristics of the vertex chamber.

Inner Radius	3.7 cm
Outer Radius (sensitive)	16.2 cm
Geometrical Coverage	$ \eta < 2.3$
Number of cells in a layer	
VTX0	16
VTX1,VTX2	32
Sense Wires	
Material	Alloy of Co, Cr, Ni, Fe, Mo
Diameter	25 μm
Resistivity	1.8 k Ω /m
Tension	80 g
Cathode and Grid Wires	
Material	Gold-plated aluminum
Diameter	152 μm
Tension	360 g
Gaseous Mixture	$\text{CO}_2/\text{C}_2\text{H}_6/\text{H}_2\text{O}$ a (95:5:0.5)
Gas Gain in Sense Wires	$\sim 4 \times 10^4$
Average Drift Velocity	7.3 $\mu\text{m}/\text{ns}$
Spatial Resolution	$\sim 50 \mu\text{m}$
Two-track Resolution Efficiency	90%, for separations > 0.6 mm

Table 3.1: Main characteristics of the Vertex Chamber (VTX).

The Transition Radiation Detector (TRD)

The transition radiation is emitted by highly relativistic particles ($\gamma > 10^3$), when traversing the interface between two media with different dielectric constants[40]. In practice, transition radiation detectors are very used to distinguish electrons from pions at energies of few GeV, when contrary to pions ($\gamma \approx 10$), electrons are highly relativistic particles.

In $D\bar{O}$ spectrometer, the TRD provides an independent electron identification method, in addition to that given by the calorimeters. The TRD is placed just outside the vertex chamber just described. Like the VTX, the TRD is also composed of three concentric cylindrical layers, each one containing a radiator element, followed radially by an X-ray detection module, with 256 readout channels (or cells).

In Fig. 3.5 one can see the end view of one of such cells. The radiator stage is composed by 393 18 μm thick polypropylene foils, immerse in Nitrogen gas with a separation of about 150 μm between foils. The energy spectrum of the radiated X-rays is below 30 keV, with a peak around 8 keV. Following the radiator there are the conversion and amplification stages, where the X-rays are detected through the charge deposited in the sense wires due to the ionization of the gaseous mixture. These stages are separated by a grid, which serves to shape the electrostatic field inside the cell.

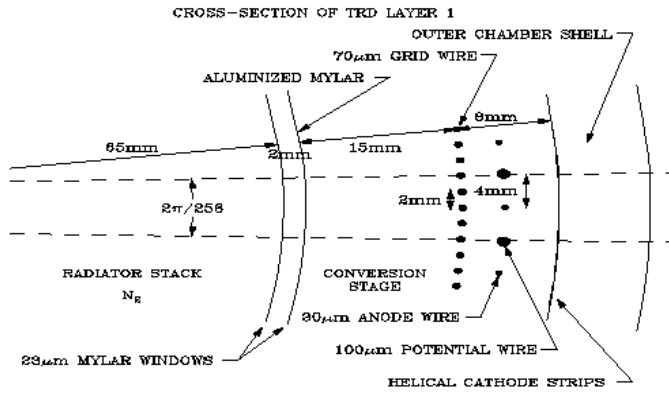


Figure 3.5: End view of some cells of the Transition Radiation Detector (TRD).

Inner Radius	19 cm
Outer Radius	47 cm
Geometrical Coverage	$ \eta < 1.6$
Length	~ 180 cm
Number of cells in a layer	
two innermost layers	256
outermost layer	512
Sense Wires	
Material	Gold-plated tungsten
Diameter	$30 \mu\text{m}$
Field Shaping Wires	
Grid Wires	
Material	Gold-plated tungsten
Diameter	$70 \mu\text{m}$
Potential Wires	
Material	Gold-plated Copper/Beryllium
Diameter	$100 \mu\text{m}$
Gaseous Mixture	$Xe/CH_4/C_2H_6$ at 91:7:2
Thickness at $\theta = 90^\circ$	
Radiation Length	0.081
Interaction Length	0.036

Table 3.2: Main characteristics of the Transition Radiation Detector (TRD).

Each layer has 256 readout channels, where the two innermost layers have 256 sense wires while the outermost layer has 512 sense wires. There, two adjacent sense wires correspond to the same readout channel.

The TRD was submitted to tests with 5 GeV electron and pions beams^[39], and allowed a pion rejection factor of 50, keeping an efficiency of 90% for electrons. Tab. 3.2 lists the main characteristics of the transition radiation detector.

The Central Drift Chamber (CDC)

Drift chambers are traditional, versatile detectors, used in almost every high energy physics experiments today, for the tracking of charged particles. It is very used also for the energy deposition (dE/dx) measurement, which can be used in the identification of the ionizing particles traversing the drift chamber.

In $D\bar{O}$ spectrometer, with the absence of magnetic field in the central detector volume, the energy deposition dE/dx is used to point out the presence of more than one MIP (*Minimum Ionizing Particle*) in the same cell, which allows us to distinguish electrons from e^+e^- pairs from photon conversion before the central drift chambers.

The Central Drift Chamber (CDC) has a cylindrical shape, centered at the beam line. It is placed just outside the TRD, described in the previous subsection.

As one can see from Fig. 3.6, CDC has four concentric layers, each one containing 32 cells distributed along the azimuth. Each cell contains seven sense wires parallel to the beam line, splitting the cell into two halves. Like in VTX, adjacent sense wires are slightly misaligned by $\pm 200\mu\text{m}$, to help solving left-right ambiguities. Besides that, neighbor layers are mutually displaced half a cell, to help in track pattern recognition. With this geometry, the largest drift distances are about 7 cm.

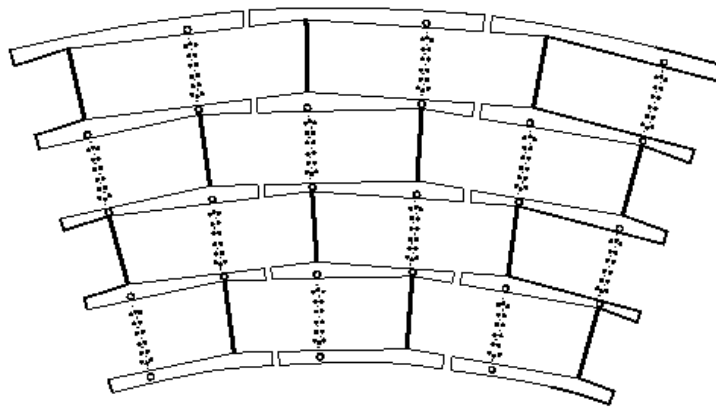


Figure 3.6: End view of some cells of the Central Drift Chamber (CDC).

Before the first and after the last sense wires in each cell there are delay lines, which propagate signals induced by the nearest sense wire. Measuring the difference in arrival times for these signals in each extremity of CDC allows the determination of the particle's longitudinal position, i.e. parallel to the beam line. The potential applied to the inner and outer sense wires in each cell is higher than the potential for the other sense wires, to induce stronger signals in the delay lines.

The CDC was tested with cosmic rays and test beams^[39], and its spatial resolution varies from $100\ \mu\text{m}$ to $200\ \mu\text{m}$ for drift distances of 1 cm and 5 cm respectively. The

Inner Radius	49.5 cm
Outer Radius	74.5 cm
Length	184.0 cm
Geometrical Coverage	$ \eta < 1.2$
Number of cells in a shell	32
Sense Wires	
Material	Gold-plated Tungsten
Diameter	30 μm
Potential	
inner and outer	1.58 kV
others	1.45 kV
Gains	
inner and outer	6×10^4
others	2×10^4
Gaseous Mixture	$Ar/CH_4/CO_2/H_2O$ at 92.5:4:3:0.5
Average Drift Velocity	34 $\mu\text{m}/\text{ns}$
Spatial Resolution	$< 230 \mu\text{m}$
Two-track Resolution Efficiency	90% for separations $> 2.5 \text{ mm}$

Table 3.3: Main characteristics of the Central Drift Chamber (CDC).

CDC's two-track resolution efficiency is about 50% for separations of 1.7 mm, increasing to 90% for separations of 2.5 mm. Finally, the dE/dx measurements allow rejections of 2 MIP's in the same cell by a factor of 95, with 95% efficiency for individual electrons.

Tab. 3.3 lists the main characteristics of the central drift chamber.

The Forward Drift Chambers (FDC)

Located in the ends of the other subdetectors previously described, the Forward Drift Chambers (FDC's) extend the charged particle tracking capability to distances of up to ~ 5 cm from the beam line, what corresponds to a geometrical coverage of $1.4 < |\eta| < 3.1$.

In each extremity, the FDC is composed of three chambers: one Φ chamber, with radial sense wires adequate to the measurement of the azimuthal angle ϕ , physically located between two Θ chambers, which have sense wires arranged appropriately to the measurement of the polar angle θ . This arrangement of chambers is shown in Fig. 3.7. Its radial dimensions are a little smaller ($r \sim 61$ cm) than the outer radius of the CDC's, leaving room for the cables carrying electronic signals from the inner chambers (VTX and TRD).

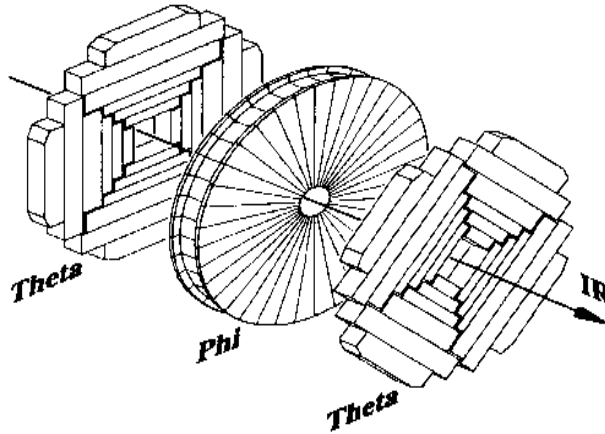


Figure 3.7: View of the Θ and Φ modules, which compose the Forward Drift Chambers (FDC) in one of the extremities of the central detector.

Each Φ module has 36 wedge-shaped cells. Each cell contains 16 sense wires longitudinally aligned. There is a grounded potential wire between each pair of adjacent sense wires, which shapes the electrostatic field inside the cell.

The Θ modules are composed of mechanically-independent quadrants, each one containing six rectangular cells at increasing radii. Each cell contains eight longitudinal sense wires, and a pair of grounded guard wires between adjacent sense wires similarly to CDC. Both Θ modules in the same endcap are mutually rotated by 45° in ϕ with respect to each other.

In any module (Θ or Φ), adjacent sense wires are staggered by $\pm 200\mu\text{m}$, to help solving left-right ambiguities. The gaseous mixture is identical to that of CDC, with similar values for the drift field and gas gains. The maximum drift distance, at the outer portion of the Φ chamber, is 5.3 cm.

The Θ chambers were tested with pion and electron test beams^[39]. The test results indicate a spatial resolution varying from $160\mu\text{m}$ to $240\mu\text{m}$ for drift distances from 0.5 cm to 5.0 cm respectively, and the longitudinal resolution is about 2 mm, with a 95% detector efficiency for single tracks. The two-track resolution is about 90% for separations of 2.5 mm. The rejection factor for photons converted into e^+e^- pairs is between 31, for high multiplicity events, and 85 for isolated tracks.

3.2.2 The Calorimeters

Calorimeters are one of the most common detector pieces in modern High Energy Physics experiments. The main purpose of a calorimeter is the measurement of the energy for the incident particles, but it can also be used in conjunction with other detectors, to provide some particle identification capability, e.g. for electrons, photons,

neutrons, neutral kaons, etc. However, calorimeters are destructive detectors, since a particle needs to deposit all its energy in the calorimeter in order to have this energy accurately determined. The incident particle is then absorbed in the calorimeter.

The interaction of incident particles with the material of the calorimeter produces small particle showers. Since leptons and photons are not affected by strong interactions, these particles produce *electromagnetic showers*, with very distinctive characteristics from the more common *hadronic showers* produced with any other particles.

Electromagnetic showers are produced from two dominant processes: *bremsstrahlung* ($e^\pm \rightarrow e^\pm\gamma$) and pair production ($\gamma \rightarrow e^+e^-$). Both processes are induced by the sub-atomic electromagnetic field inside matter, and tend to privilege small angles between final particles. On the other hand, hadronic showers are produced by the strong interactions in collisions of hadrons with atomic nuclei existing in matter. Thus, hadronic showers have average transverse dimensions larger than electromagnetic showers, which are usually more collimated.

Another feature which helps in distinguishing these two kinds of showers is the velocity in which the energy of the incident particle is absorbed in the material media. The average depth of the longitudinal development of an electromagnetic shower is much smaller than that for hadronic showers.

These distinguishing features between electromagnetic and hadronic showers are very used with identification purposes, and the calorimeters are usually optimized to efficiently distinguish electromagnetic from hadronic showers. Therefore, electromagnetic calorimeters are usually thinner and finely segmented longitudinally, absorbing almost totally the energy of incoming electrons and photons, while only a small fraction of the energy of incoming hadrons is absorbed. Hadronic calorimeters are positioned right after electromagnetic calorimeters, and are usually thicker and less segmented longitudinally. Hadronic calorimeters point out the presence of hadrons and measure their energies.

Concerning the operation philosophy, there are two kinds of calorimeters. The so-called *total absorption calorimeter* is designed to measure all the energy deposited by incident particles. These calorimeters are composed of active materials, which allow the direct measurement of all the energy from incident particles.

A second kind is the so-called *sampling calorimeter*, where only part of the absorbed energy (called sampling fraction) is detected in the active medium. The rest is absorbed in some absorbing material (*absorber*). In such a case, the detected energy should be corrected to provide the total energy absorbed from the incident particle. A sampling calorimeter is usually made of dense materials as absorbers, so that they can be more compact than total absorption calorimeters.

In a sampling calorimeter, the fractional energy resolution $\sigma(E)/E$ is usually expressed^[41] as

$$\left(\frac{\sigma}{E}\right)^2 = (C)^2 + \left(\frac{S}{\sqrt{E(\text{GeV})}}\right)^2 + \left(\frac{N}{E(\text{GeV})}\right)^2 \quad (3.2)$$

where C is due to calibration errors, S represents shower shape fluctuations and N reflects noise contributions.

Due to the absence of central magnetic field in $D\bar{O}$, the calorimeter must provide a good resolution for the measurement of electron, photon and jet energies. Its information is also used to help in the identification of muons and to establish the transverse energy balance in an event. The need for a compact detector made the sampling calorimeter option the best one for $D\bar{O}$. Uranium, copper and steel are used as absorbing materials, while liquid argon (LAr) was chosen for the active material.

The $D\bar{O}$ calorimeter is divided into three parts: one central calorimeter (CC) covering the region $|\eta| < 1.2$, and two endcap calorimeters (EC) covering the region $1.1 < |\eta| < 4.5$, as shown in Fig. 3.8.

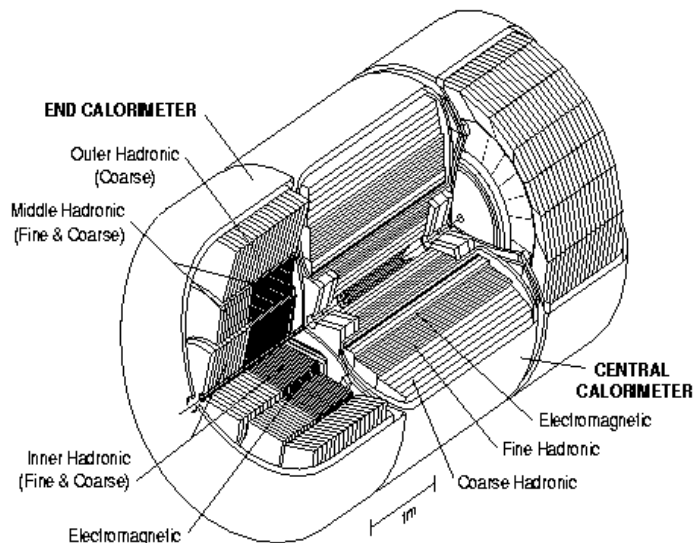


Figure 3.8: Isometric view of the central and endcap calorimeters.

The calorimeters are finely segmented, with the basic readout cells, each covering $\Delta\eta = 0.1$ and $\Delta\phi = \frac{2\pi}{64} \sim 0.1$, allowing jets to be observed individually, and more than that: allowing the jet shape evolution to be analyzed. The readout cells are radially aligned, forming the so-called “pseudo-projective towers”^[39]. This fine segmentation is shown in Fig. 3.9. Note that the third layer of the electromagnetic calorimeters have even finer segmentation ($\Delta\eta \times \Delta\phi = 0.05 \times 0.05$), to provide better spatial location of the shower centroids.

There are also the ICD (*Intercryostat Detectors*) and MG (*Massless Gaps*) detectors, which were designed to help in the energy correction due to energy lost in uninstrumented regions of the calorimeters, mostly in the region $0.8 < |\eta| < 1.4$. These detectors can also be seen in Fig. 3.9.

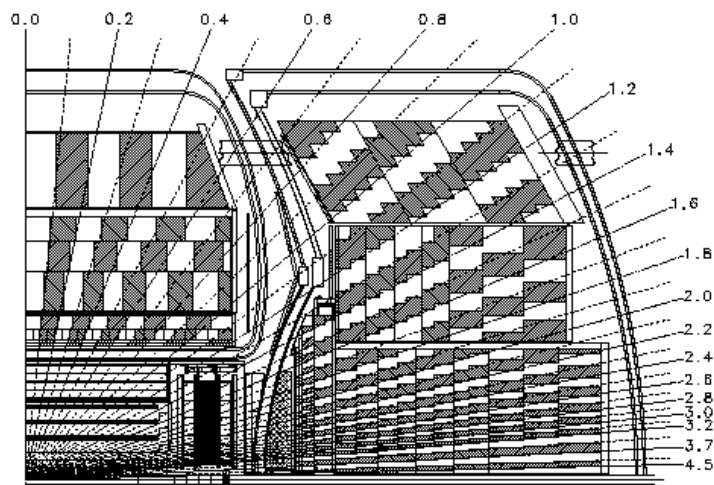


Figure 3.9: Longitudinal cut of the calorimeters, showing the fine segmentation of the central and endcap calorimeters. The numbers shown are values of pseudo-rapidity, η .

More details about the central and endcap calorimeters are described in the following subsections.

Central Calorimeter (CC)

The central calorimeter is subdivided into three concentric cylindrical layers, centered in the beam line, as can be seen in Fig. 3.10. These layers are labeled CCEM (Central Calorimeter – ElectroMagnetic), CCFH (Fine Hadronic) and CCCH (Coarse Hadronic). Note the misalignment between adjacent layers, so that no track coming from the interaction region can pass through more than one intermodule gap.

Figure 3.10: End view of the Central Calorimeter. The hole in the upper part is for the passage of the Main Ring pipe.

The CCEM, with a total depth of more than 20 radiation lengths¹ (X_0), absorbs more than 97% of the energy of incident electrons or photons. The energy resolution for electrons in the CCEM was studied in test beams^[39], and it is well represented by:

$$\left(\frac{\sigma}{E}\right)^2 = (0.003)^2 + \left(\frac{0.162}{\sqrt{E(\text{GeV})}}\right)^2 + \left(\frac{0.140}{E(\text{GeV})}\right)^2 \quad (3.3)$$

The central hadronic calorimeters, CCFH and CCCH, have a total depth of 3.2 interaction lengths² (Λ) each, for the development of hadronic showers, which in general are initiated in the CCEM itself, which corresponds to 0.76 Λ .

The central calorimeter has about 14,600 electronic channels. Its weight is about 331 *ton* when filled with liquid argon, including the support structure. The main characteristics of the central calorimeter are summarized in Tab. 3.4.

Central Calorimeter	CCEM	CCFH	CCCH
Inner Radius (cm)	84.1	105.7	170.8
Outer Radius (cm)	105.0	170.1	224.0
Length (cm)	264.8	266.1	266.4
Total Weight (<i>ton</i>)	19.2	132.8	115.2
Number of modules	32	16	16
Absorber Material	Uranium	Uranium	Copper
Absorber Thickness (cm)	0.3	0.6	4.65
LAr Thickness (cm)	0.23	0.23	0.23
Total Radiation Length (X_0)	20.5	96.0	32.9
Total Inter. Length (Λ)	0.76	3.2	3.2
Sampling Fraction (%)	11.79	6.79	1.45
Number of Readout Cells	10368	3456	768
Geometrical Acceptance	$ \eta < 1.2$	$ \eta < 1$	$ \eta < 0.7$

Table 3.4: Main characteristics of the Central Calorimeter (CC)^[39, 42]. X_0 and Λ are the radiation and interaction lengths respectively.

¹The radiation length X_0 of a material is defined as the average distance in which an incoming electron or photon would loose a fraction of $(1 - e^{-x/X_0})$ of its initial energy, absorbed through electromagnetic interaction with the material medium.

²The interaction length Λ of a material is defined as the average distance in which an incoming hadron would loose a fraction of $(1 - e^{-x/\Lambda})$ of its initial energy, absorbed through strong interaction with the material medium.

Endcap Calorimeters (EC)

The two endcap calorimeters, ECN and ECS (Endcap Calorimeter North and South), cover the pseudo-rapidity region $1.1 < |\eta| < 4.5$, like caps for the central calorimeter barrel (see Fig. 3.8). Each one is subdivided into four different kinds of modules: the ECEM (Endcap Calorimeter ElectroMagnetic) in the inner part of the EC's; the ECIH (Inner Hadronic) behind the ECEM and just around the beam pipe; the ECMH (Middle Hadronic) concentrically around the ECIH; and the ECOH (Outer Hadronic) around the ECMH, is the farthest from the beam pipe.

There is also one more subdivision level: the ECIH splits into IFH (Inner Fine Hadronic, closer to the interaction region) and ICH (Inner Coarse Hadronic), while the ECMH similarly splits into MFH (Middle Fine Hadronic) and MCH (Middle Coarse Hadronic).

Each endcap calorimeter has about 15,520 electronic channels and, when filled up with LAr , it weights about 238 *ton*, including the support structure. The main characteristics of the different EC modules are summarized in Tab. 3.5.

Endcap Calorimeters	ECEM	IFH	ICH	MFH	MCH	ECOH
Inner Radius (cm)	5.7	4.0	4.0	90	90	161
Outer Radius (cm)	104	86.4	86.4	159	159	224
Longitudinal Length (cm)	23.8	97.1	74.0	72	79	178
Total Weight (<i>ton</i>)	5.0	32.0 ^a		68.8 ^b		88.0
Number of modules	1	1	1	16	16	16
Absorber Material	U	U	aço	U	aço	aço
Absorber Thickness (cm)	0.4	0.6	0.6	0.6	4.65	4.65
LAr Thickness (cm)	0.23	0.21	0.21	0.22	0.22	0.22
Total depth (X_0)	20.5	122.	32.8	116.	38.0	65.1
Total depth (Λ)	0.95	4.9	3.6	4.1	4.1	7.0
Sampling Fraction (%)	11.9	5.66	1.53	6.68	1.64	1.64
Number of channels	7488	5216 ^c		1856 ^d		960
Minimum $ \eta $	1.4	1.6	2.0	1.1	1.3	0.7
Maximum $ \eta $	4.0	4.5	4.5	1.7	1.9	1.4

Table 3.5: Main characteristics of the Endcap Calorimeters (EC)[39, 43]. X_0 e Λ are respectively the radiation and interaction lengths. (a) Total weight of IFH+ICH. (b) Total weight of MFH+MCH. (c) Total number of channels for IFH+ICH. (d) Total number of channels for MFH+MCH.

The EC performance was analyzed in test beams^[44]. The fractional energy resolution for electrons in the ECEM is described by:

$$\left(\frac{\sigma}{E}\right)^2 = (0.003)^2 + \left(\frac{0.157}{\sqrt{E(\text{GeV})}}\right)^2 + \left(\frac{0.29}{E(\text{GeV})}\right)^2 \quad (3.4)$$

while for pions in the ECEM+ECIH, the fractional energy resolution is represented by:

$$\left(\frac{\sigma}{E}\right)^2 = (0.047)^2 + \left(\frac{0.439}{\sqrt{E(\text{GeV})}}\right)^2 + \left(\frac{1.28}{E(\text{GeV})}\right)^2 \quad (3.5)$$

3.2.3 The Muon System

Lepton identification (muons and electrons) is a powerful method very used as a tag for production of heavy quarks and weak vector bosons W^\pm and Z . Muon identification is usually simpler than electron identification, because besides muons, less than 0.2% of the hadronic energy escapes the calorimeters, while electron signals have to be extracted from a large number of particles which emerge from the $p\bar{p}$ collision and reach the inner part of the calorimeter.

The muon detection system in DØ consists of a set of three layers of *Proportional Drift Tubes* (PDT), providing electronic signals for the tracking of muons coming from the interaction region at angles up to 3° from the beam pipe ($|\eta| < 3.4$). These layers are labeled A (innermost), B and C (outermost). The muon system is divided into two parts: WAMUS (*Wide Angle Muon System*) covers the region $|\eta| < 2.4$, and SAMUS (*Small Angle Muon System*) covers the forward regions ($1.7 < |\eta| < 3.4$). A schematic view of the several chambers and stations which compose the DØ muon system is shown in Fig. 3.11.

There are also five toroidal magnets, placed between A and B layers. These magnets generate a local magnetic field restricted to their volumes, which allows the muon momentum measurement. The central toroid (CF) weights 1970 *ton* and covers the region $|\eta| < 1$. The two endcap toroids (EF) weight 800 *ton* each, and cover the region $1 < |\eta| < 2.5$. These three toroids are connected in series, receiving a nominal electrical current of about 2500 A, for a generated magnetic field of about 2 Tesla. The SAMUS toroids weight 32 *ton* each, covering the region $2.5 < |\eta| < 3.6$, and receive electrical currents of about 1000 A. All magnets, muon chambers and SAMUS stations are placed outside the calorimeters, as can be seen in Fig. 3.12.

The accurate determination of p_{T_μ} requires the determination of muon trajectories before and after the toroids. The innermost segment is determined from the primary vertex, central detector information and muon data from A-layer. The outer segment is determined from the signals left by the muon in the outer layers, B and C.

Figure 3.11: Schematic view of the $D\bar{D}$ muon detection system, showing the relative position of the several WAMUS chambers and SAMUS stations. This figure also shows the definition of the $D\bar{D}$ global coordinate system.

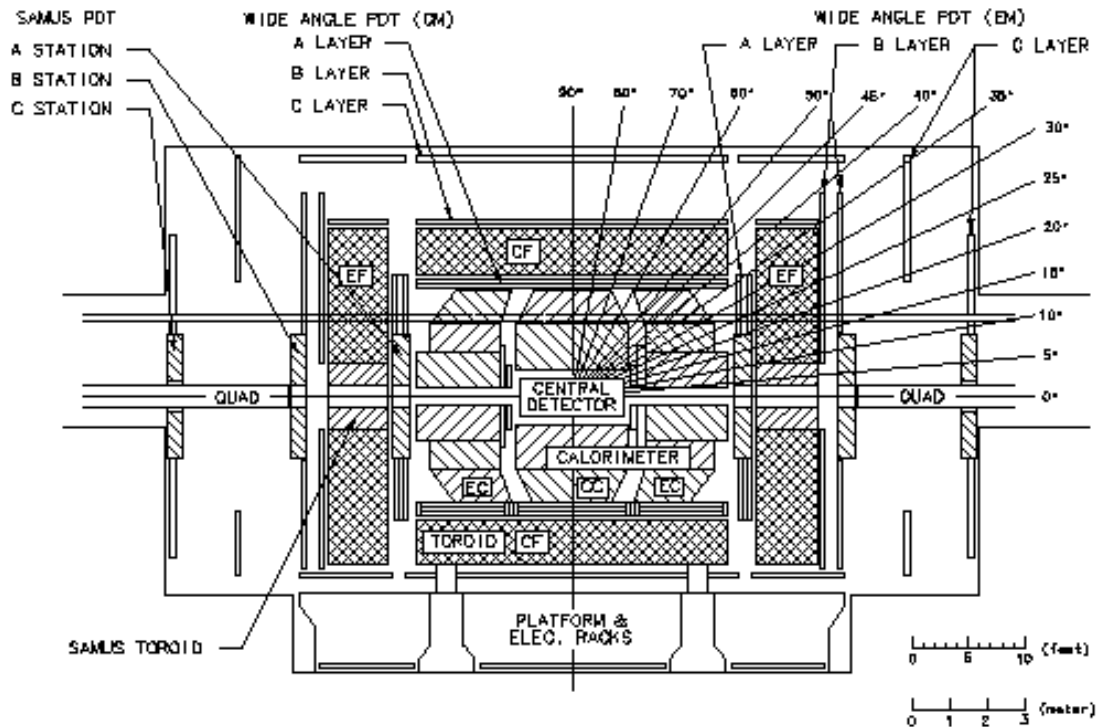


Figure 3.12: Side view of the $D\bar{O}$ detector, showing the muon chambers, SAMUS stations and toroidal magnets, components of the muon detection system. In the right half of the figure the numbers represent polar angles (θ), while in the left side the numbers are the corresponding pseudo-rapidity values (η).

WAMUS System

The 164 chambers of the WAMUS system are formed by three decks of cells (four decks, in the case of A-layer chambers), in an aluminum structure, as depicted in Fig. 3.13. The number of PDT's per plane varies from 14 to 24, and the chamber length goes from 335 cm to 579 cm, depending on the chamber localization. The total number of WAMUS PDT's is 11,386, and the cell geometry is uniform in any chamber, namely 10 cm wide and 5 cm high, which corresponds to a maximum drift distance of about 5 cm.

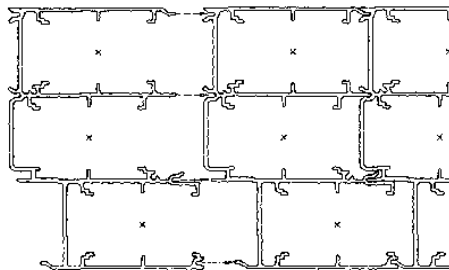


Figure 3.13: End view of a WAMUS chamber, showing the geometry of B- and C- layers. A-layer chambers have a similar structure, but with 4 PDT decks instead of 3.

The WAMUS chambers are filled with a gaseous mixture composed of $Ar(90\%) / CF_4(5\%) / CO_2(5\%)$, which is ionized by the passage of a muon. In the center of a PDT, the anode wire is kept at an electrostatic potential of +4.56 kV, while the cathode pads in both wider PDT's faces are kept to +2.3 kV. The anode wires of two neighbor PDT's are ganged together in one extremity of the chambers, and the electronic signals are readout in the other extremity, from both ganged anode wires. In normal operating conditions, the drift velocity is about $65 \mu\text{m}/\text{ns}$, with a variation of 3% for a 10% variation in the electrostatic field inside the PDT.

In order to improve muon momentum resolution, all WAMUS chambers have their anode wires aligned parallel to the magnetic field, so that we have the best resolution in the measurement of the deflection in the muon trajectory, due to the magnetic field.

The drift time of electrons to the anode wires gives us the transverse coordinate, with a resolution of about 0.5 mm. The determination of the longitudinal coordinate ξ is performed in two stages. First, from the difference (ΔT) in arrival times of electronic signals in opposite extremities of the anode wire, we determine ξ with a resolution of 9 (23) cm along the wire, for muons incident close (far) to the chamber extremity containing the readout electronics. In a second stage, with the analogic information from the cathode pads, we obtain a finer determination of ξ , as described next.

The cathode pads are composed of two electrodes with complementary geometry, like repeating diamond patterns. The pattern is repeated every 61 cm along the pad (see Fig. 3.14). The first stage in the determination of the longitudinal coordinate ξ is enough to resolve in each pattern the muon hit the pad. The second stage compares the amounts of charge (Q_a and Q_b) deposited in each of the two electrodes in a pad, providing a finer determination for ξ . This procedure has a spatial resolution better than $2 \text{ mm}^{[39]}$, independent on the longitudinal distance from the anode wire extremities.

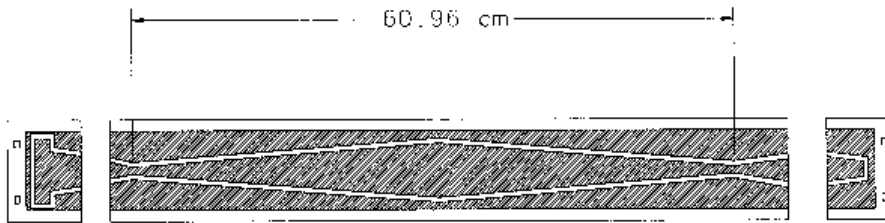


Figure 3.14: Design of the cathode pads in WAMUS PDT's, showing the complementary and periodic geometry of its two electrodes.

The WAMUS system is divided into two parts, labeled CF and EF, which cover pseudo-rapidity ranges very similar to those corresponding to the WAMUS toroids. Therefore we can say that CF is the central region of the muon system, while EF is the transition region between the central and the small angle (SAMUS) regions. The main characteristics of the WAMUS system are summarized in Tab. 3.6.

Maximum External Dimensions	
Length	335-579 cm
Width	142-254 cm
Number of PDT's per chamber	
A-Layer (4 decks)	≤ 96
B- and C-Layers (3 decks)	≤ 72
Total Number of WAMUS PDT's	11386
Anode Wires	
Material	Gold-plated tungsten
Diameter	50 μm
Tension	300 g
Potential	+4.56 kV
Cathode Pads	
Material	Copper-clad Glasteel
Repeating distance	609.6 mm
Potential	+2.30 kV
Maximum Drift Distance	5 cm
Run 1a	
Gaseous Mixture	$Ar/CF_4/CO_2$ at 90:5:5
Average Drift Velocity	65 $\mu\text{m}/\text{ns}$
Maximum Drift Time	770 ns
Run 1b	
Gaseous Mixture	$Ar/CF_4/CO_2$ at 90:6:4
Average Drift Velocity	67 $\mu\text{m}/\text{ns}$
Maximum Drift Time	750 ns
Spatial Resolution	
Transversal	± 0.5 mm
Longitudinal	± 1.6 mm

Table 3.6: Main characteristics of the wide angle muon detection system (WAMUS).

SAMUS System

The Small Angle MUon System (SAMUS) was designed specially for operation in a high-background environment, with high occupation rate, typical of small angles in hadronic colliders. SAMUS is based in cylindrical PDT's, with inner diameter of 29 mm.

There are three SAMUS stations in each extremity of the detector, one for each layer. Each station has external dimensions $312\text{ cm} \times 312\text{ cm}$, with a square hole in the center, where the beam pipe gets into the detector. The hole dimensions are $61\text{ cm} \times 61\text{ cm}$ ($86\text{ cm} \times 86\text{ cm}$, in the case of C-layer stations). Each station is composed of vertical and horizontal planes of PDT's (labeled X and Y respectively), which combine to provide cartesian coordinates of hits. A third plane, labeled U, has PDT's at 45° from the horizontal direction, to resolve ambiguities in the associations of X and Y hits for multihit events. In any given plane, the PDT's are arranged so that the division between two cylindrical PDT's is covered by a third PDT, avoiding the existence of blind regions, and making sure that all incident muons will necessarily leave hits in the system, as can be seen in Fig. 3.15. There is a total of 5,232 PDT's in SAMUS system.

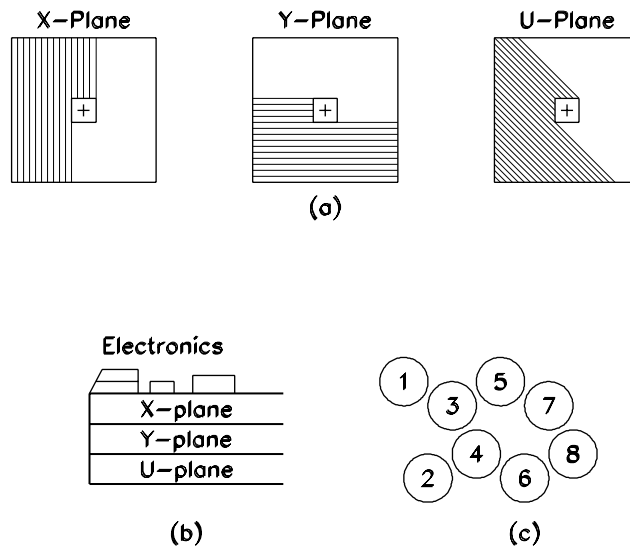


Figure 3.15: Geometry of SAMUS stations. (a) different orientations of x , y and u planes of PDT's. (b) transverse view of a SAMUS station. (c) relative arrangement of PDT's in any plane.

The SAMUS system operates with a gaseous mixture of $CF_4(90\%)/CH_4(10\%)$, with average drift velocity of $97\ \mu\text{m}/\text{ns}$ and maximum drift times of 150 ns. Performance studies for an isolated PDT showed that the transverse position from the anode wire is measured with a spatial resolution of 0.35 mm. The main characteristics of SAMUS system are summarized in Tab. 3.7.

Outer Dimensions		312 cm
Hole Dimensions	A, B	61 cm
	C	86 cm
Number of PDT's in a plane	x, y	512
	u	720
Anode Wires		
Material		Gold-plated tungsten
Diameter		50 μm
Tension		208 g
Gaseous Mixture		$CF_4(90\%)/CH_4(10\%)$
Average Drift Velocity		97 $\mu\text{m}/\text{ns}$
Maximum Drift Time		150 ns
Spatial Resolution		$\sim 50 \mu\text{m}$

Table 3.7: Main characteristics of the small angle muon detection system (SAMUS).

3.3 Data Acquisition and Trigger Systems

The Data Acquisition System (DAQ) is the system responsible for receiving the many electronic signals from the detector, encode them and store these packed data into magnetic media, for posterior processing³ and analysis.

The amount of digitized electronic signals coming from the many detector readout channels, and from the signal processing electronics in $D\emptyset$, corresponds to a typical event size of about 500 kb/event. The $D\emptyset$ detector had a typical $p\bar{p}$ collision rate of 120,000 per second in Run 1a (March/92 to March/93). For Run 1b (started in December/93), the typical rate grew to about 500,000 collisions per second. However, only a very small fraction of such collisions really produce interesting final states, from the point of view of the physics studied at $D\emptyset$. Even if all these collisions were actually interesting, the DAQ system would not have capability of recording all the events to tape at so high a rate. The trigger system is responsible for the on-line selection of the best events, using physics criteria, making sure that the DAQ capacity is effectively used to record the best events, for posterior analysis.

The trigger system at $D\emptyset$ is subdivided into some levels. The first of them, labeled **Level 0**, signals the occurrence of inelastic $p\bar{p}$ collisions. After that, the **Level 1** trigger looks for electronic signals in the muon chambers, geometrically aligned like a muon coming from the interaction region. The Level 1 also looks for showers in the calorimeters, signaling the presence of electrons, photons or hadronic jets in the event. The answers from the Level 1 trigger must be ready in about 2.6 μs , before the next beam crossing, so that the system can decide if it needs more time to register the last event,

³The many data processing stages are described later in this chapter.

or discard it and get ready for the next one to come. The last trigger level, called the **Level 2**, performs a quick event reconstruction, confirming the previous trigger levels, but applying more sophisticated criteria in its decision. Therefore, the event rate at the output of Level 2 have to be adjusted to the storing rate of the data acquisition system.

There is an additional trigger level, called **Level 1.5**. Its trigger logic is very similar to that used at Level 1, but it is necessary whenever the output rates from Level 1 are so high to feed Level 2 directly (see Fig. 3.16). Level 1.5 has a larger decision time than Level 1, therefore its use introduces a dead time into the system. This means that, while the Level 1.5 trigger system is calculating its decision, the detector systems cannot detect any other collision to come.

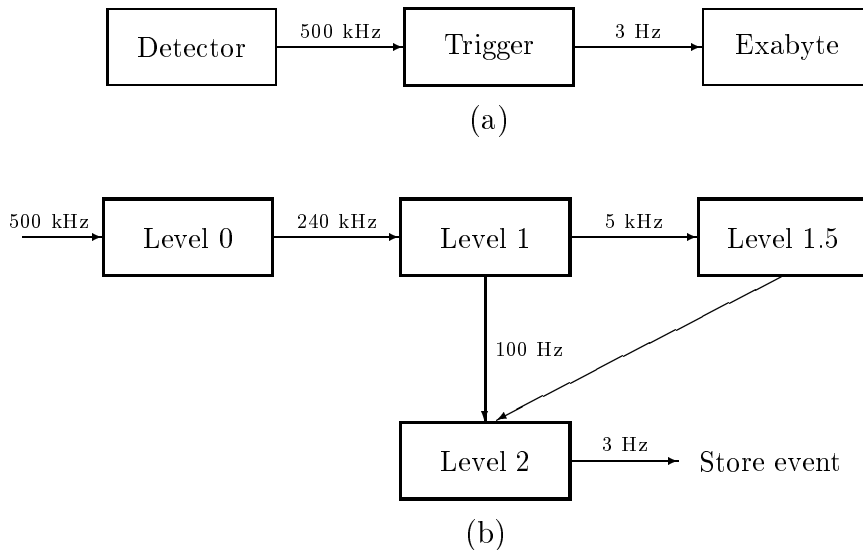


Figure 3.16: Simplified diagrams of the trigger system at $D\bar{O}$. (a) the trigger function as an event filter; (b) maximum event rates acceptable at the input of each trigger level.

In the following subsections we briefly discuss all trigger levels we have just mentioned.

3.3.1 Level 0 Trigger

The Level 0 Trigger signals the presence of inelastic collisions, points out the likelihood of multiple interactions in a single beam crossing, provides a first estimation on the longitudinal coordinate of the primary vertex to be used in trigger decisions, and it is also used for luminosity monitoring at $D\bar{O}$. The Level 0 output rate, which depends on the instantaneous luminosity, is typically of 200 kHz.

The Level 0 hardware consists of two scintillator hodoscopes mounted in front of the inner surfaces of each endcap calorimeter, in both ends of the central calorimeter. Each hodoscope is formed by the superposition of two identical planes of scintillator

elements, with a relative rotation of 90° , as shown in Fig. 3.17. Each hodoscope contains 20 short ($7\text{ cm} \times 7\text{ cm}$) and 8 long scintillator elements ($7\text{ cm} \times 65\text{ cm}$).

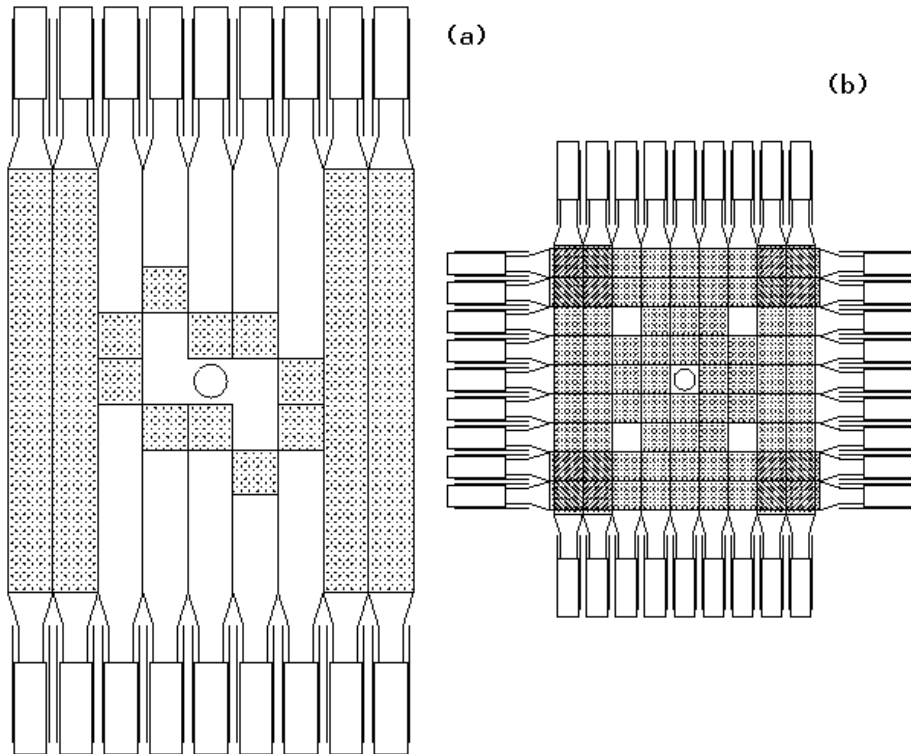


Figure 3.17: Geometry of the Level 0 hodoscopes: (a) Geometry of each one of the two scintillator planes which compose a hodoscope. (b) Final lay-out of the whole system.

The coincidence of signals from both hodoscopes is more than 99% efficient for non-diffractive inelastic collisions. The estimation of longitudinal coordinates of primary vertices is calculated at hardware level, from the difference in average arrival times of particles in each hodoscope. The root-mean-square (RMS) deviations of arrival times in each hodoscope are added in quadrature to determine the total deviation σ_0 , used to identify the presence of multiple interactions. Finally, the instantaneous luminosity is determined with 12% uncertainty, from the rate of non-diffractive inelastic collisions, identified by the coincidence of Level 0 signal with $|z_{\text{vtx}}| < 97\text{ cm}$.

We should note that the determination of z_{vtx} is done at hardware level, so that this result can be used in other trigger levels. In particular, the measurement of the transverse energy (E_T) of showers in the calorimeters must be corrected due to the large spreading in the longitudinal position of primary vertices (typically $\sigma_z = 30\text{ cm}$). A fast estimation (z_{fast}) of primary vertex position, with 15 cm resolution, available 800 ns after beam crossing, is used in Level 1 calculations (see next subsection). A slower but much better estimation, z_{slow} , with longitudinal resolution of 3.5 cm, is available in 2.1 μs and is used for Level 2 calculations.

3.3.2 Level 1 Trigger

Tevatron operation with six bunches of protons and antiprotons corresponds to a time interval of $3.5 \mu\text{s}$ between crossings. Any trigger decision taken in this time interval does not introduce dead time in the system.

Level 1 Trigger consists of a collection of hardware elements disposed in a flexible architecture, with software-programmable capability. The whole system is coordinated through the *Level 1 Trigger Framework* (L1TF), which receives digital signals from many trigger elements, each one corresponding to a subdetector or their subdivisions, and combines these digital signals according to programmable logic, based on physics criteria.

The L1TF has veto and prescaling capabilities. Vetos are associated to undesirable features of an event, and the presence of any such feature inhibits triggers, which would otherwise be inevitable. Prescaling can be applied to triggers with very high passing rate, to reduce the output rates by an integer factor, in order to feed subsequent trigger levels. Prescaling is very used in $D\bar{O}$ for adjusting the many trigger configurations as a function of the instantaneous luminosity, in order to avoid overloads in Level 2. Level 2 processing capacity was about 100 Hz in Run 1a. Choosing the prescaling factors is the role of a committee, with representatives from all physics groups in $D\bar{O}$, with the purpose of optimal distribution of the system bandwidth among the several analysis groups, taking into account the physics analysis priorities of the collaboration.

The Level 1 trigger decision is based in a set of 256 AND-OR terms, each one corresponding to a specific part of the spectrometer. The final decision is coded in a 32-bits word, called *trigger bits*. Each trigger bit is defined by a boolean pattern which indicates, for each AND-OR term, if it should be satisfied, negated (veto) or ignored for that particular trigger bit. Any trigger bit, when satisfied, fires the DAQ for readout of all analog information for that event. All this information is digitized and sent to Level 2 processors. If Level 1.5 confirmation is required for that trigger bit, this confirmation is calculated before the event is sent to Level 2, and the result is communicated to DAQ. The L1TF also mounts a data block summarizing all trigger conditions (AND-OR terms) which led to the results of each trigger bit. This data block is also appended to the final event data, and can be used later for off-line trigger system debugging and performance analysis.

The Level 1.5 trigger philosophy is very similar to that from Level 1, except regarding decision time. Level 1.5 is not restricted to the time limit of $3.5 \mu\text{s}$ of beam crossings, so that it can be more elaborated and demanding than level 1, thus allowing this latter to be more efficient, with higher output rates, which will have then to be confirmed by level 1.5 decision. In other words, Level 1.5 is an advantageous alternative to avoid prescaling at level 1, as it chooses the best events to be sent to level 2, instead of the mere drawing of prescaling.

The Level 1 Muon Trigger

The Level 1 Muon Trigger (L1MU) is particularly interesting in the development of the present work, not only for the fact that it is the main requirement at trigger level for collecting the data samples used in this analysis, but also because the LAFEX group gave a significant contribution, in both software and hardware, to the development of this system.

Fig. 3.18 shows a block diagram of the muon trigger system. The basic unit given to L1MU by WAMUS and SAMUS systems are the so-called *trigger latches*. Each trigger latch is a single bit corresponding to a single PDT out of the 16,618 PDT's which compose the DØ muon system. The trigger latches correspond to a granularity of 10 cm for WAMUS and 3 cm for SAMUS. Whenever a muon traverses a PDT, a corresponding bit is fired and we have a *hit*.

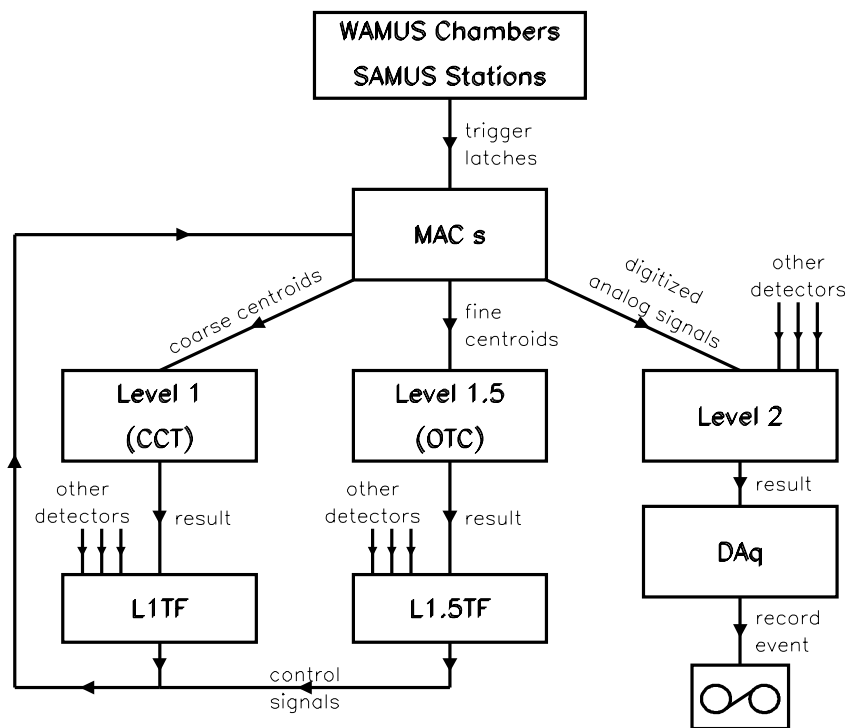


Figure 3.18: Block diagram of the muon trigger system.

The trigger latches are sent through cables to the *Moving Counting House* (MCH)⁴, where most of the muon trigger electronics⁴ is located. In the MCH, the trigger latches arrive at the MAC (Module Address Card) cards, which combine neighbor hits in *fine centroids* using a pre-programmed coincidence logic. For WAMUS system, there is a

⁴Most of L1MU cards are designed according to a modified VME protocol.

one-to-one correspondence between chambers and MAC cards, totalling 164 MAC's. For SAMUS, the need for higher granularity for background rejection requires two MAC's per plane, or six MAC's per station, totalling 36 MAC's. The whole system has a total of 200 MAC's.

To avoid spurious noise, we demand hits in a minimum of two decks for the definition of a centroid in each layer. This minimum is set to three decks in regions with higher background level (EF). The fine centroids have granularity of half a cell (5 cm for WAMUS and 1.5 cm for SAMUS), and constitute the basic unit for level 1.5 muon trigger. Each MAC is able to calculate up to 48 fine centroids, which can be sent to the *Octant Trigger Cards* (OTC's), which are the electronic boards for level 1.5 muon trigger calculations.

MAC cards also calculate the boolean OR of three adjacent fine centroids, producing the *coarse centroids* (CC's). The CC's have granularity of 15 cm in WAMUS and 12 cm in SAMUS. Coarse centroids are the basic units for L1MU, which is therefore also called *Coarse Centroid Trigger* (CCT). Once calculated, these coarse centroids are sent in parallel to a sequence of boards programmed with different coincidence logics, according to the block diagram shown in Fig. 3.19. There are different sets of coincidence logic:

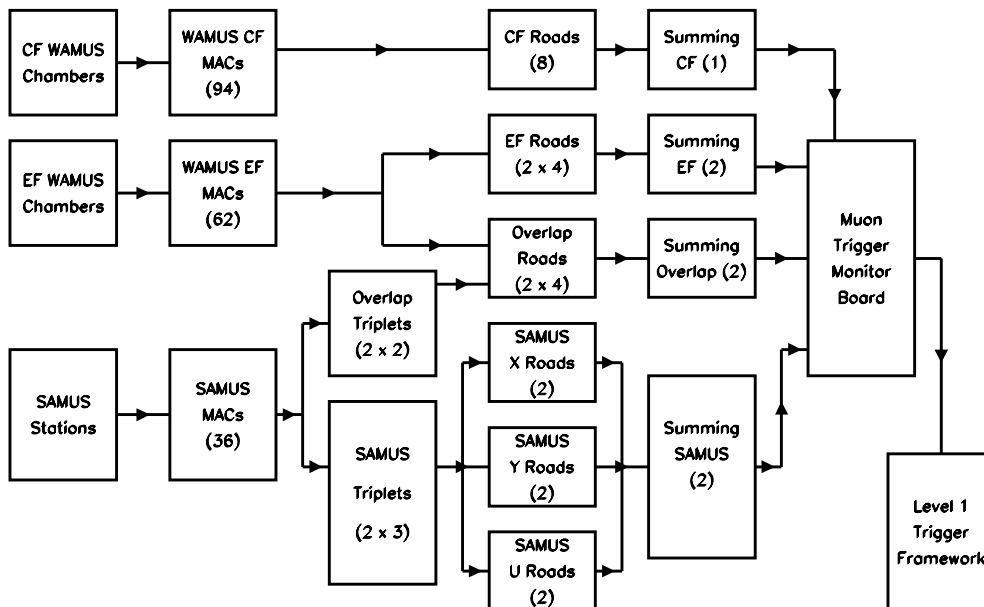


Figure 3.19: Block diagram of the Level 1 Muon Trigger (L1MU). LAFEX group gave a significant contribution to the development of all the trigger logic, and also to the fortran trigger simulator package, MUSIM. One can see in parenthesis the number of each kind of board in the trigger system.

- **Road Finders** – searches for $A \cdot B \cdot C$ coincidences, which mean at least one centroid in each layer. This is the logic where we look for a set of hits compatible with the trajectory of a muon coming from the interaction region.
- **Triplet Finders** – used for SAMUS stations only, it comes before the road finders. It searches for $X \cdot Y \cdot U$ coincidences. U-plane is used to resolve ambiguities. Each triplet corresponds to a small square with sides of 12 cm.
- **Summing Boards** – count how many $A \cdot B \cdot C$ survived, in each trigger region. Each of these boards provide a two-bit counter, and also a set of bits informing the presence of muons in each octant or quadrant of any region (see below for the definition of trigger regions).

The L1MU system operates independently in seven different regions of the detector: CF (central), EFN, EFS (EF North/South), ON, OS (overlap North/South), SN e SS (SAMUS North/South). The regions ON and OS are mixed regions, where the muon traverse both SAMUS stations (A and B layers) and WAMUS chambers (B and C layers), therefore the informations from these two different systems need to be combined in the trigger logic. The central region is subdivided into 8 octants, while all other trigger regions are subdivided in four quadrants each. The coincidence logics (roads and triplets) operate independently in each quadrant/octant. Each region has its own summing board, which summarizes the trigger status for that region, providing in the output a two-bit counter and also a set of bits (one per quadrant/octant) signaling which quadrant/octant had triggers. This information is used to save processing time at level 2, by reconstructing only those regions which had a trigger fired in level 1.

The output two-bit counters from all the summing boards are sent to the *Trigger Monitor Board*, which converts those bits into the so-called *physics bits*. The physics bits depend on the global trigger configuration, through a pre-programmed mapping downloaded at the start of each run, and they are sent to the L1TF as a group of up to sixteen AND-OR terms, which will be used in the definition of the trigger bits, i.e. the final decision of the whole level 1 trigger system. Examples of common definitions for these AND-OR terms are:

- Two muons in the central region ($|\eta| < 1$);
- One muon in WAMUS ($|\eta| < 1.7$);
- One muon in SAMUS ($2.2 < |\eta| < 3.4$);

LAFEX contribution to L1MU System

We shall not leave unmentioned here the important contributions from LAFEX group to the development and implementation of the L1MU system, specially in the forward regions, as described below.

During the first tests of the L1MU system, only CF and EF regions had a temporary logic for cosmic ray commissioning. Data integrity problems were detected in the communication between MAC's and OTC's. The problem was traced to be due to synchronization and control signals, the fix involved reprogramming some *Programmable Logic Devices* (PLD).

After that, there was a total reevaluation of the trigger logic, with the purpose of reducing the firing rates due to cosmic radiation in the CF and EF regions.

After this study, we assumed the responsibility of developing all the trigger logic for the forward regions. The aim was to reach a rejection factor of at least 100 for the overlap and SAMUS regions at level 1. One should note that $D\bar{O}$ was not the first experiment who tried to build a muon trigger at small angles, but all the previous experiments failed due to extremely high background levels, typical of forward regions in hadronic colliders.

The first stage involved the development of a trigger simulator package, which was extensively used in viability studies with real minimum bias events collected in $D\bar{O}$ spectrometer. These studies showed that the original design would not be capable of reaching the planned rejection. A higher granularity design was called for, and the simulator proved useful once more in performing these studies.

The final project involved the design of a new electronic board, called *SAMUS Trigger Card* (STC), specially projected to be a triplet finder board for SAMUS stations. However, this board proved to be so versatile that it could be used, with minor modifications, for many other coincidence logics needed for triggering in the forward regions. The STC board allowed the use of a much larger number of input bits (16 per MAC, 6 MAC's per STC board) than the CCT board (4 per MAC, 13 MAC's per CCT board), used in CF and EF regions. This higher granularity was essential to strongly reduce the trigger rates in the forward regions, but the rejection factor was still around 40 in overlap and 5 for SAMUS.

More trigger studies suggested the implementation of cuts on centroid multiplicity in SAMUS stations, as well as using more restrictive logics for coarse centroids in EF WAMUS chambers. These two criteria were the best options we found to reach the rejection factors we needed. Both of them were indeed implemented.

At this point we had the optimal set of equations to be used in the trigger logic for the forward regions. All LAFEX people at $D\bar{O}$ participated of the effort for implementation of these equations in hardware. This effort included programming of PLD's, debugging of STC boards, development and debugging of pascal programs for the standalone testing of STC and CCT boards, installation and cabling of all the boards in the system, *in loco* debugging of the trigger system after installation, using data collected in real $p\bar{p}$ collisions, and using both the $D\bar{O}$ event display package for visualization and the trigger simulator for certification of the proper working of the L1MU system as a whole. All this scheme was successfully implemented, thanks to the intense participation of

LAFEX people. The L1MU system has proven to be very stable, with small problem rate, and LAFEX people has been continuously involved in the activities related to the level 1 muon trigger, including its maintenance and debugging in case of eventual problems.

As a final remark, the analysis of the present work atests the proper working of the L1MU system in the forward region, as it provided good quality data to be used in our analysis, leading to the extraction of important physics results.

3.3.3 Level 2 Trigger

Also called *level 2 filter* and *software trigger*, it was composed of up to 128 VAXStation 4000-60 processors, which receive all the event raw data from the many VME digitizing crates. The level 2 trigger is the place where all the information for a single event is put together for the first time, and therefore all this information can be used for more sophisticated algorithms for trigger decision. Level 2 trigger must have the capability of reducing its ~ 100 Hz of input rate to ~ 3 Hz of output rate, which corresponds to the DAq capacity of writing events to magnetic media.

Level 2 algorithms are based in a set of *filter tools*, each one related to a given physical object, or event characteristics. Examples of such physical objects are: jets, muons, electromagnetic showers (photons or electrons) and total transverse energy. Each filter tool executes one of the standard algorithms for the reconstruction of those objects, in a very similar way as the reconstruction package does it. But only those physical objects which have been seen at level 1 trigger can be confirmed at level 2. Therefore level 2 trigger does not waste time in a full reconstruction of the event. Instead, it only reconstructs those regions needed to confirm objects which fired level 1 trigger (or level 1.5, when it is required).

Each global trigger configuration associates each one of the trigger bits to one or more sets of filter tools, in previously defined combinations programmed via software. As an example of such combinations, a trigger bit associated to two muons at level 1 is associated to one or more filters: one filter may confirm the presence of two muons; a second filter may look for at least one of the muons with transverse momentum above a given threshold, and so on.

Each combination of a trigger bit and a given set of filter tools is assigned a filter bit. The filter bits correspond in level 2 to what the trigger bits are in level 1. We can define a maximum of 128 filter bits in a given global trigger configuration.

3.3.4 Data Acquisition System

Once the level 2 requirements are satisfied, all the event data is sent to the host cluster, which stores the events on tape. The host cluster is composed of the following processors:

- **VAX 6620** receives the events sent from level 2 processors and writes them on disk, sending part of these events for on-line monitoring. The maximum recording rate is about 1.5 Mb/s, which represents about three typical events (500 kb each) in a second.
- **VAX 6410** is the primary machine responsible for spooling events from the staging disk to 8 mm tapes. It also performs downloading operations, sending operational parameters needed to control the signal processing electronics.
- **VAX 8810** is devoted primarily to hardware monitoring, but also participates in downloading operations.
- **13 VAXStations** are the human interfaces to the DAq system. These stations coordinate all control and monitoring operations of the DAq and detector systems, including on-line visualization of part of the collected events with the purpose of assuring the good quality of collected data.

All these complex data acquisition and detection systems are totally controlled by a sophisticated set of software packages, whose main elements are shown in Fig. 3.20. The process COOR is the responsible by the global coordination of all DAq and detector processes, like a server process, to which all client processes are connected, and have to ask for specific detector configurations, changes of operational parameters, etc.

Figure 3.20: Working scheme of the main software packages in the host cluster of $D\bar{O}$ data acquisition system.

3.3.5 Monitoring System

In such a complex set of subsystems like the DØ spectrometer, there is a very large number of conditions which can damage the quality of collected data, or even damage the hardware of these subsystems. These conditions are generally easy to be monitored through measurable parameters (like temperature, high voltage, current, humidity, etc.). Whenever any of these parameters go beyond certain limits considered normal, warning signals or messages are dispatched to a central process, which notifies the operators appropriately. This software process, called *Alarms*, written in Pascal, was developed specially to satisfy these monitoring needs.

This monitoring process is executed in the DAq server. It receives alarm signals from many sources, and dispatches them appropriately to many client processes. Hardware components are monitored at rates of 15 Hz. Even the software processes whose proper working is essential are constantly monitored through heartbeats which are periodically sent from each monitored process to the alarm server. The absence of these heartbeats are generally caused by a crash of that process, and therefore alarms can be generated and dispatched to the appropriate client processes.

Some of the alarms are considered to be high-priority. The occurrence of such alarms interrupts an on-going run, or inhibits the start of a new one while the problem is not fixed. Examples of such high-priority alarms are the excess of electrical current or high-voltage trip in detector readout channels, or high temperature and/or humidity in any of the signal processing VME crates.

3.4 Data Processing

As any other high energy physics experiment, the collected data in DØ undergoes a chain of data processing stages. Typical data processing stages are the data acquisition, reconstruction, monitoring, physics data analysis and Monte Carlo simulation.

Due to the large number of people involved in all steps of software development, a rigorous discipline procedure must be applied in order to keep track of all the documentation and specifications of the produced software.

3.4.1 Utilities

A huge amount of data is daily produced in such a big experiment. The data management in DØ is mainly based in two products, RdB and ZEBRA. RdB^[45] is a database manager used in the on-line environment, for documentation, monitoring, control, maintenance and recovering of all relevant information relative to the collected

data and also the analysis procedures. ZEBRA^[46] is part of CERN software library, and provides a standard environment of hierarchical banks for common data storage, as well as a set of tools to support the use of pointers which associate banks holding related informations. ZEBRA system is used for the management of the many different data types, including real detector data, detector geometry parameters (geometry, positioning and alignment), calibration constants, graphics interface control and data taking control parameters, histograms, etc.

The event is arranged in ZEBRA format by the level 2 processors themselves, even before any on-line calculation. Various standard utilities are required to be supplied before any new ZEBRA bank is included in the $D\bar{O}$ official library. They include documentation files, a parameter file giving the structural link, a bank booking routine, a function returning the pointer to the bank, a routine which returns the values of the bank data words, and a dump-printing routine, for debugging purposes.

Parameters controlling program behavior (such as values of cuts to be used on off-line analysis) are kept in ASCII RCP (Run Control Parameter) files. A set of utilities have been developed which read these RCP files, storing the information in ZEBRA banks, where these data can be easily accessed, also using utility routines.

The $D\bar{O}$ official software is grouped into many separated libraries. These libraries are maintained by a set of procedures based in CMS (Code Management System). There are about 50 different subdirectories in the $D\bar{O}$ library, each one associated to a specific software package, like D0GEANT ($D\bar{O}$ detector simulation), ZEBRA_UTIL (ZEBRA bank handling utilities), etc. Each subdirectory is maintained by a *Czar*, a specialist responsible for the control, update and documentation of each software package.

People involved in software development periodically update the software packages, always under the coordination of the czar. Library updates generally occur in two steps. At first, a test version is released, and everyone is notified on the update and encouraged to test it. After this test period, the approved version is then declared official, replacing the previous version.

The source codes and object libraries are automatically distributed to many VAX computers in remote sites of collaborating institutions, in order to keep the same software environment in all institutions. Porting software to other computing platforms usually requires intermediate steps of source code conversion.

An event display package in $D\bar{O}$ was developed based on DI3000 graphics system^[47], with an interface package called PIXIE, developed at $D\bar{O}$ ^[48]. This package offers the capability to make 2- and 3-dimensional views of the detector, with electronic signals and reconstructed tracks and other objects superposed on the picture. Fig. 3.21 shows a typical example of a side view of the $D\bar{O}$ detector. The event shown is a typical top event candidate, where a high- p_T reconstructed muon and a high- E_T electromagnetic shower compose one of the most promising signatures for such $t\bar{t}$ events.

Another important utility for simplifying and standardizing the software tools

Figure 3.21: Side view of a $t\bar{t}$ candidate, as seen by the DØ detector. The presence of two high- p_T leptons, a muon and an electron, is a characteristic topology for events with a pair of top quarks.

used in the data analysis is the so-called *Program Builder* (PBD). The program builder forces any package to follow certain strict rules before they can become official in $D\bar{O}$ library. These rules are developed specially to keep all packages with some degree of uniformity, and also make some repetitive tasks (like event reading, output file creation, RCP file reading, etc) completely transparent to the common user.

The program builder has a small set of standard environments (called *frameworks*), which work like the main processing flow, and are associated to groups of typically used in high energy physics processing tasks, namely: D0Geant (detector simulation), D0Reco (event reconstruction), D0User (off-line data analysis) and Examine (on-line monitoring).

Each framework has a number of hooks, which shall/must be provided by each software package, so that they can be executed by the framework. The hooks correspond to typical processing tasks, like job initialization, event processing, job summary, histogramming, event display, event dump, etc. Some of these hooks are specially reserved for the user to introduce their own analysis programs, to be concatenated with other packages.

Each software package has a descriptive ASCII file, which informs PBD which routines should be called in each processing stage. Special object libraries and RCP files needed by the package are also informed in this descriptive file.

The program builder is invoked with a single command, which indicates the required framework, the software packages to be concatenated, as well as any other options needed. The PBD generates the Fortran source code with the necessary calls to concatenate the many packages, according to the command entered. Some command files needed for linking and execution are also created in the process. The PBD allows therefore that complex application packages can be built from two or more simpler packages. All the communication between different software packages should only occur through ZEBRA banks and their utilities.

3.4.2 Event Reconstruction

One calls *event reconstruction* to the process of decoding and interpreting the many electronic signals (raw data) collected in the detector, and its translation in terms of physical quantities like trajectories, energies, momenta, particle identification, etc.

All the raw data decoding and interpretation, noise rejection, correction for non-instrumented regions, etc., generate some characteristic objects like CD tracks, energy deposition in calorimeters and tracks in muon chambers. These algorithms are written by the specialists in each subdetector. In a later stage, other algorithms associate the aforementioned objects with physical objects, like electrons, photons, hadronic jets and muons, but also tries to reject backgrounds to these physics objects whenever possible.

The amount of collected data in a typical 12 months period of data taking is about 2.0×10^7 events, or 10 terabytes of data. About 10% of these events, chosen to be the best ones based on physics criteria, are directly sent to the so-called *Express Line*, to be immediately reconstructed and available for data analysis. The total sample is reconstructed in large farms of Unix processors (Silicon Graphics 4D/35). This reconstruction farm has a production capacity of almost 100,000 events per day, enough to keep the off-line reconstruction up with the data taking.

For each raw data file, two reconstructed data files are produced by the reconstruction program. STA files keep all the raw data, and adds to it the information generated in the reconstruction process. This kind of data can be used later in forthcoming reconstruction stages which become needed for any reason. Each STA event corresponds in average to 600 kb. DST files contain a reduced version of each event, keeping only those variables relevant to off-line data analysis, like reconstructed muon, electron and jet parameters, and discarding most of the raw information from the detector. In DST format, each event contains in average 20 kb. The STA files are kept on tape only, while DST files stay available on disk for a large time period, on the so-called *File Serving Cluster* (D0FS). The D0FS cluster has about 300 Gb of disk storage capacity, with the purpose of keeping most of the DST data permanently on disk.

A full catalog with all output files generated by the reconstruction process is kept in a production database, based on RdB. The production database also keeps informations about tapes, trigger and filter versions, reconstruction program versions, etc. Consult utilities can be used to build lists with subsets of data according to specific conditions. In this catalog, each data file has a generic name, which defines it univocally. With the help of FATMEN system^[49], these generic names can be directly ordered by the off-line analysis programs, to access any data file (raw data, DST or STA) from any collected run, wherever the data is stored (D0FS disk, or vaulted tape), with read time scales from few seconds (for files stored on disk) to few hours (for data files kept only on vaulted tapes).

The SAMUS muon reconstruction part of the reconstruction process is particularly interesting to the present analysis, and its algorithm is described in section 4.2.

3.4.3 Monte Carlo Simulation

The Monte Carlo simulation is, undoubtedly, one of the most important tools for experimental high energy physics. A detailed simulation allows us to evaluate the performance of any detector in the study of any physical process, even before the first screw is on place.

We can subdivide the many stages of Monte Carlo simulation in two big groups: first, the simulation of physical processes, involving all the features relevant to each process; second, the detector simulation, which shows us how the detector “sees” each

event, or process, etc.

In our particular case, to simulate $p\bar{p}$ collisions and the physical processes involved in the production of new particles in these collisions, we used ISAJET model, which was already described in section 2.4. Therefore, in this section we are restricted to discuss the simulation of the detector itself.

Besides being essential during the stage of physics analysis of collected data, the Monte Carlo simulation of the $D\bar{O}$ detector has been extremely important since the design and construction stages. For instance, the development of the complete event reconstruction code before the detector commissioning with real collisions required the complete and detailed simulation of the $D\bar{O}$ detector, to the level of digitization of all electronic analog signals received at the ADC's, and including all physical processes of scattering and interactions with all the materials used in the real detector.

The $D\bar{O}$ detector simulator package, called $D\bar{O}$ Geant, is based on GEANT^[50], developed at CERN. GEANT provides convenient means of specifying volumes of particular materials, and properly simulates the passage of particles through these materials, including all possible scatterings and interactions of the incident particle with the traversed material. Processes such as multiple Coulomb scattering and evolution of electromagnetic and hadronic showers are accurately simulated by the GEANT package, and the energy deposits in any specific volume are later digitized, similarly to the processing of real data through the digitizing boards.

The geometrical simulation of the $D\bar{O}$ detector is very rich. The central detectors and muon chambers are detailed to the level of sense wires, cathode materials, support structures, etc. The simulation of the calorimeters is, however, less detailed due to the large CPU time involved in the detailed simulation of shower evolution. The detailed simulation of calorimeter showers is replaced by a parameterization based on the complete and detailed simulation of more than 1 million showers. Besides of being in excellent agreement with the detailed simulation, this parameterization process for the average shower evolution speeds up the simulation process by a factor of about 3000^[51], in the simulation of the calorimeter showers.

3.4.4 Trigger Simulation

The $D\bar{O}$ trigger system was briefly described in section 3.3. To properly consider the trigger effects in our data sample, we need to do a detailed study on the effect of trigger criteria on those events we are looking for. The trigger simulation includes all trigger levels mentioned previously.

Contrary to the Monte Carlo simulation, which is a random simulation, the trigger simulation is exact. It starts from the raw data from the detector, simulates all calculation involved in the trigger logic, and provides the trigger system decision in terms of trigger and filter bits, like in real life. The trigger simulator allows a precise

determination for the trigger efficiency in the selection of our data sample.

We could give a significant contribution for the development of this important software tool, due to our expertise acquired in the design and implementation on the L1MU hardware. Our contribution to this system included the overlap and SAMUS regions as a whole, and then had a great impact in this analysis, for the estimation of the muon detection efficiency, which is going to be discussed in details later, on chapter 3.

The L1MU hardware was described in subsection 3.3.2. My contribution for the development of the trigger simulator was basically in writing the many routines to simulate the coincidence logic of each electronic board used in the level 1 muon trigger system: road finders, triplet finders and summing boards. Actually the trigger simulator was developed even before the implementation of all these boards into the system. The trigger simulator was indeed used on the many studies which preceded the hardware implementation. The initial project had to be modified a few times, due to the results we found during our viability studies^[52].

Once implemented, the level 1 muon trigger system proved to be a very robust system, with low failure rate at hardware level. The worst problem is at the time needed for the L1MU decision for overlap regions and SAMUS regions, both in south, where we find the longest electric cables bringing trigger latches to the trigger electronics, and also due to an extra level of coincidence logic, needed to search for triplets in SAMUS stations.

3.4.5 Off-line Analysis Packages

The off-line data analysis programs constitute the final part of all the data processing. In this stage we make all the studies specific to a given physics topic.

In general, DST files contain all the information needed to the data analysis stage, so we usually can access the data in few minutes. The user can make his analysis programs any way he likes it. There are utilities for stripping (to select specific trigger and/or filter bits for analysis), for histogram filling or N-tuple building. The event ZEBRA structure allows the creation of user-defined ZEBRA banks, for more sophisticated analysis methods, where the user defined information can be stored along with the rest of the DST information.

In the present thesis, most of our analysis was performed using N-tuples. Therefore, this processing stage consisted basically in filling N-tuples appropriately, with the variables relevant to our analysis. These variables were carefully analyzed interactively using a powerful analysis tool, called PAW^[53]. The details of the interactive data analysis are described in the next chapter.

Chapter 4

Data Analysis

Along this chapter we describe all the treatment of data collected in our experiment, with the purpose of measuring the muon production cross section in the forward region. The first section has a discussion about the Monte Carlo sample, which guided us through the choice of selection criteria for our data.

Then we start to describe the experimental determination of the inclusive muon cross section from the observed muon distributions. The selection criteria at both trigger level and off-line cuts are enumerated. The procedures for estimating the muon detection and reconstruction efficiencies are described. The background contamination in the final data sample is also estimated.

Section 4.8 shows how the systematical errors, associated to the many procedures involved in the determination of σ^μ , are estimated.

By the end of this chapter, our results are presented, discussed and compared to the theoretical predictions shown at the last section of chapter 2.

4.1 The Simulation of Forward Muons

Our first attempt to generate a Monte Carlo sample for muons in the forward region consisted in using the ISAJET event generator for the simulation of strong interaction processes in $p\bar{p}$ collisions, according to ISAJET's model for unbiased NLO QCD processes^[31]. The events were classified into two basic muon samples, based on whether the muon comes from bottom quark or from charm quark decays.

However, this generation procedure was judged impractical to be used in our analysis, basically due to two facts: first, only a small fraction of the muons produced in this scheme go through the kinematical region of our analysis, i.e. forward SAMUS region. Among these few forward muons, hardly we get one with transverse momentum

high enough to satisfy trigger criteria.

The second fact is that complete events generated by ISAJET have an average multiplicity of charged particles in SAMUS region much smaller than the typical average multiplicity of real $D\bar{O}$ events. It means that this Monte Carlo sample would not be a good representation of real data. Actually this problem could be solved by the proper treatment of simulated events, in a simulation stage posterior to $D\bar{O}$ Geant, called MuSmear. This stage has the purpose of simulating the technical background of the detection process, reproducing characteristic noise, inefficiencies, beam halos, etc. However, this package has not yet been properly tuned for SAMUS region, so this situation lead us to look for alternative solutions, for a better representation of typical events in SAMUS region.

An alternative which seemed very reasonable and practical was to simulate isolated muons, with kinematic variables generated randomly according to uniform distributions. Then these muons are processed through $D\bar{O}$ Geant, and the resulting raw data is combined to the raw data of real MINBIAS¹ events. The idea here is that there is no reason why those partons not directly involved in the hard scattering should behave differently in events containing heavy quark pairs. Therefore, this combination of a simulated isolated muons into real MINBIAS events (from now on called *merged sample*) should be a better representation of bottom quark production, as far as we keep in mind the limitations of the procedure. For instance, this sample would not be adequate to study muon to jet correlations in $b\bar{b}$ events.

Therefore we generated Monte Carlo samples with about 20,000 muons uniformly distributed in transverse momentum and pseudorapidity, in the kinematical region:

$$\begin{aligned} 1\text{GeV} < p_{T_\mu} < 30\text{GeV} \\ 2.2 < |\eta_\mu| < 3.3 \end{aligned} \tag{4.1}$$

These events were then processed through the detector simulation package, $D\bar{O}$ Geant, and combined with real MINBIAS events collected in dedicated runs, with instantaneous luminosity around $3 \times 10^{30} \text{ cm}^{-2}\text{s}^{-1}$, similar to the luminosity values of the data samples collected for the present analysis. The sample thus generated was reconstructed and could be used in many of the analysis stages, described in the following sections.

4.2 On-line Event Selection

Due to the high trigger rates for forward muons in $D\bar{O}$, the events for our real data sample were collected in dedicated runs of the $D\bar{O}$ detector, with low instantaneous luminosity: around $O(3 \times 10^{30} \text{ cm}^{-2}\text{s}^{-1})$.

¹MINBIAS events are those which satisfy a level 0 trigger (inelastic collision) with good spatial location of primary vertex ($z_{\text{fast}} < 97 \text{ cm}$).

The trigger demands a good muon candidate at level 1, which means a candidate with hits in all three planes of each layer of SAMUS stations, followed by the confirmation by the level 1.5 trigger. The surviving candidates were sent to the level 2 filter, where more sophisticated algorithms were used in the muon identification. Among these criteria one cites:

- a good fit of hits into a muon trajectory (track);
- a minimum number of hits in the track fit (twelve hits);
- calorimeter confirmation of tracks, by a minimum energy deposition in the calorimeter along the muon trajectory;
- a trajectory deflection inside magnets, compatible to the local magnetic field (this means that $\Delta\vec{P}$ must have radial direction with respect to the beam line, not changing the track azimuth);
- a minimum transverse momentum of 1 GeV/c.

In addition to these requirements, sometimes a prescaling was needed to reduce the trigger rates to an acceptable level for event recording in magnetic media. These prescales are taken into account in the determination of the integrated luminosity of the collected data sample. Our analysis is based on a data sample corresponding to a total integrated luminosity of $\int \mathcal{L}(t) \cdot dt = (37.7 \pm 4.5) \text{ nb}^{-1}$, with about 30,000 events stored in magnetic tapes.

The collected events were submitted to the official data reconstruction package. After discarding bad hits (like hits with unphysical drift times), the SAMUS muon reconstruction algorithm searches for groups of hits forming triplets ($x \cdot y \cdot u$ combinations) on B and C stations. Two triplets with same azimuth in both B and C stations are combined into a straight track segment, which defines a point M in the XY plane which divides SAMUS toroid in the middle (see Fig. 4.1). A second straight track segment, connecting the point M to the primary vertex, is used to select close hits in each plane of A station.

The next step is a full track reconstruction, from two independent straight segments, before and after SAMUS magnet, taking into account the spatial location of each SAMUS hit from their drift time information. Eventually, the informations from other subdetectors (VTX, FDC and EC) is also used. The muon momentum is estimated using the deflection of the muon trajectory inside the SAMUS magnet. The energy losses in the calorimeter and magnets, estimated from the amount of material traversed by the muon, are used to correct the muon momentum.

All the relevant information resulting from the muon reconstruction calculations are stored in ZEBRA banks, and are therefore available in any posterior stage of analysis. In our data sample a total of 10,719 muons were reconstructed.

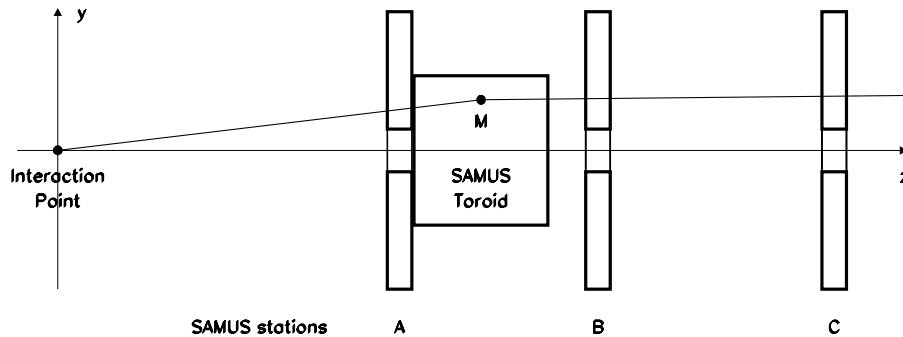


Figure 4.1: Illustration of reconstruction algorithm for SAMUS muon tracks.

4.3 Off-line Event Selection

At the experimental conditions in $D\bar{O}$, about 5% of all beam crossings contain more than one $p\bar{p}$ collision (multiple interactions). In our analysis we avoided the complications due to the possibility of such multiple interaction events, by discarding any event where two or more primary vertices were reconstructed. This procedure introduces a correction for the analyzed integrated luminosity:

$$\int_{\text{analyzed}} \mathcal{L} dt = f_{\text{si}} \int_{\text{collected}} \mathcal{L} dt \quad (4.2)$$

where f_{si} is a correction factor which depends on the average instantaneous luminosity during the data collection. In our case, we assume:

$$f_{\text{si}} = \frac{\text{events with 1 primary vertex}}{\text{Total of events}} \quad \text{for each run} \quad (4.3)$$

Fig. 4.2(a) shows the distribution of the number of reconstructed primary vertices per event (N_{vert}), and Tab. 4.1 describes the corrections introduced in the determination of the total integrated luminosity of our analyzed data sample, which will be used for the determination of $d\sigma^\mu/dp_{T_\mu}$.

During off-line analysis, additional selection criteria were applied to the data sample:

- Kinematical cuts: $2.2 < |\eta_\mu| < 3.3$ and $1 \text{ GeV}/c < p_{T_\mu} < 30 \text{ GeV}/c$. The pseudorapidity cut restricts the analysis to the SAMUS region we are interested in. The

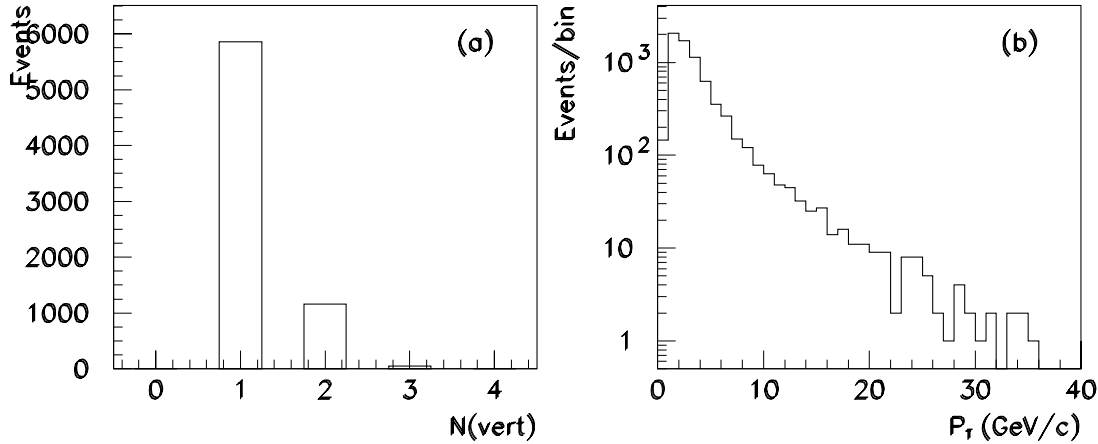


Figure 4.2: Some distributions for collected events: (a) Number of reconstructed primary vertices per event; (b) Transverse Momentum.

Run #	Integrated Luminosity (nb^{-1})			
	Collected	Analyzed	# muons	muons/ nb^{-1}
81349	5.6	4.8	564	117
81352	10.8	9.0	1120	125
81354	21.3	18.2	2026	111
Total	37.7	32.0	3710	116

Table 4.1: Average number of muon candidates in real data, per unit nb^{-1} of integrated luminosity.

lower limit on transverse momentum only confirms off-line the momentum threshold set at level 2 filter. And finally, $p_{T\mu} < 30 \text{ GeV}/c$ only discards a few events with SAMUS high- p_T muons (see Fig. 4.2(b)). The momentum measurement for these muons is probably very affected by poor momentum resolution anyway, as it is worse for high- p_T muons, as we shall see later.

- Number of hits (N_{hits}) used in the muon track fit. As shown in Fig. 3.15, the geometry of each plane of SAMUS PDT's was designed so that no track can pass unnoticed in every plane of a SAMUS station, leaving at least two hits per plane, or a total of 18 hits for each muon. Fig. 4.3 compares distributions for the number of hits used in muon track fits, for both Monte Carlo and real data. In our analysis, all muon candidates with less than 16 hits in the track fit are discarded, where this value was set to leave some room for inefficiencies or from hit “adulteration” by the presence of two or more hits in the same PDT.
- Calorimeter confirmation: to be observed at the SAMUS stations, muons have to traverse the endcap calorimeters and the SAMUS toroids, thus losing part of their energy in the material along its path. The endcap calorimeters are instrumented to detect part of the energy deposited inside them, therefore they can be used to confirm the reconstructed muon tracks. The calorimeter confirmation requirement

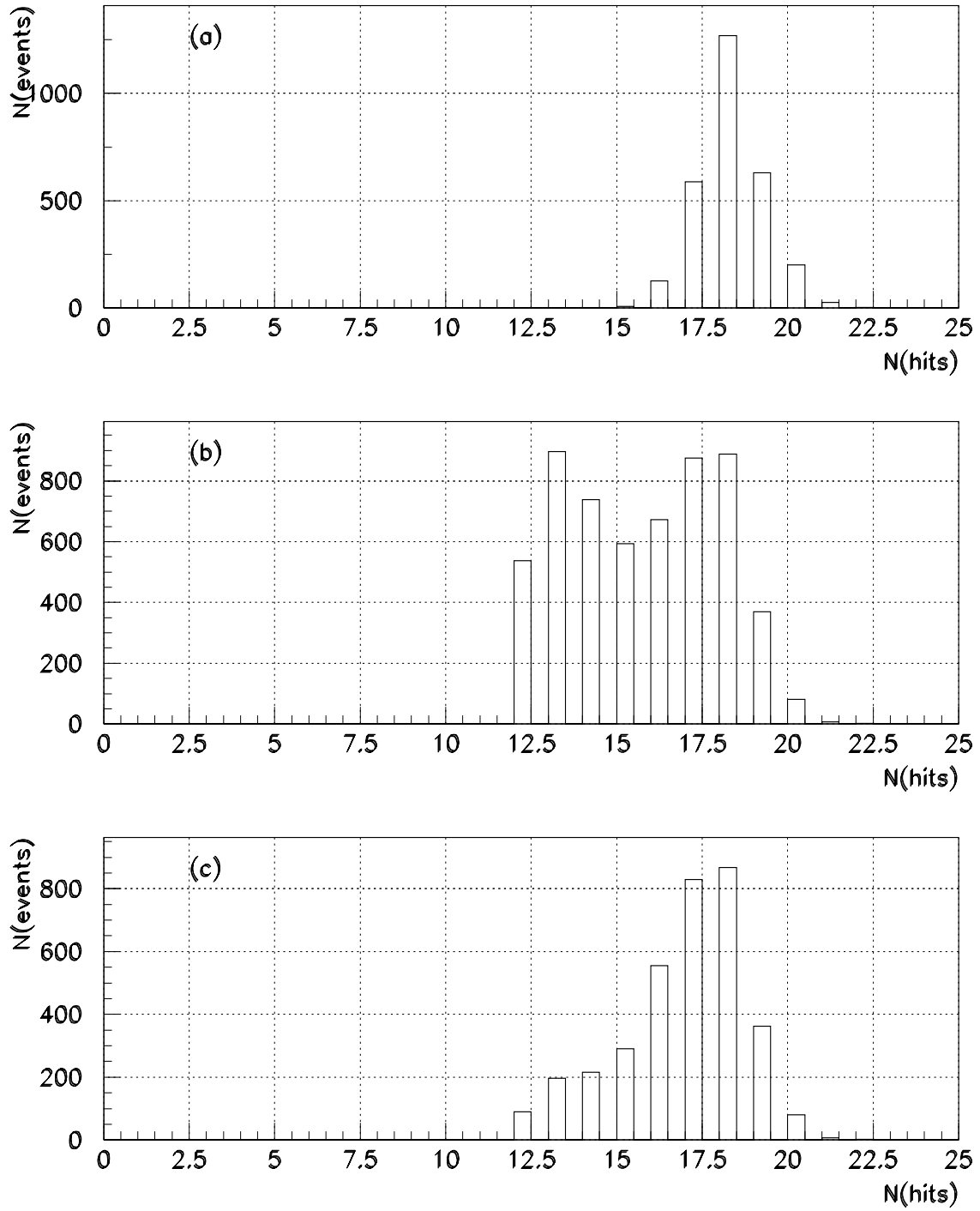


Figure 4.3: Comparison for the number of hits on a muon track. (a) Monte Carlo; (b) Real data, before off-line cuts; (c) Real data, after off-line cuts.

is very useful for the rejection of fake tracks formed by the accidental combination of spurious hits (combinatorial background), as in this case there is no energy deposition along the reconstructed muon path inside the calorimeter. The calorimeter confirmation is demanded by requiring a minimum energy (E_{had}) to be deposited by the muons through the hadronic calorimeters, compatible with the passage of a *minimum ionizing particle* (MIP). In Fig. 4.4 we can see the comparison between the energy deposited in the hadronic calorimeter, by simulated muons and by good muon candidates in real data.

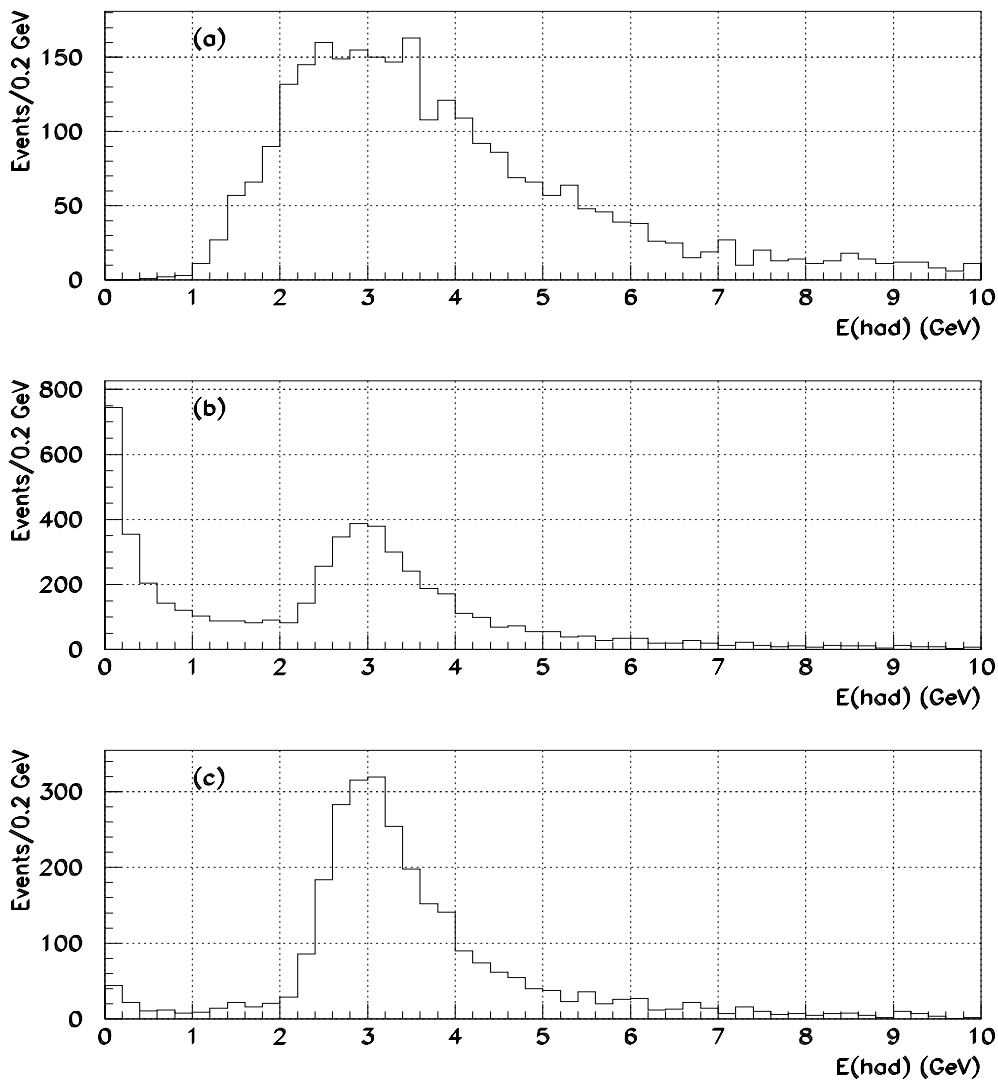


Figure 4.4: Comparison between the energy deposited in hadronic calorimeters. (a) Monte Carlo; (b) Real data, before off-line cuts; (c) Real data, after off-line cuts.

- χ^2 of muon track fit. In Fig. 4.5 one can see the χ^2 distributions for real data and Monte Carlo. One can notice that the Monte Carlo sample does not represent accurately the χ^2 distribution observed in real data. This is a nice example which shows that many adjusts are still needed on the simulator packages, in order to make our Monte Carlo simulation in better agreement to the data sample.

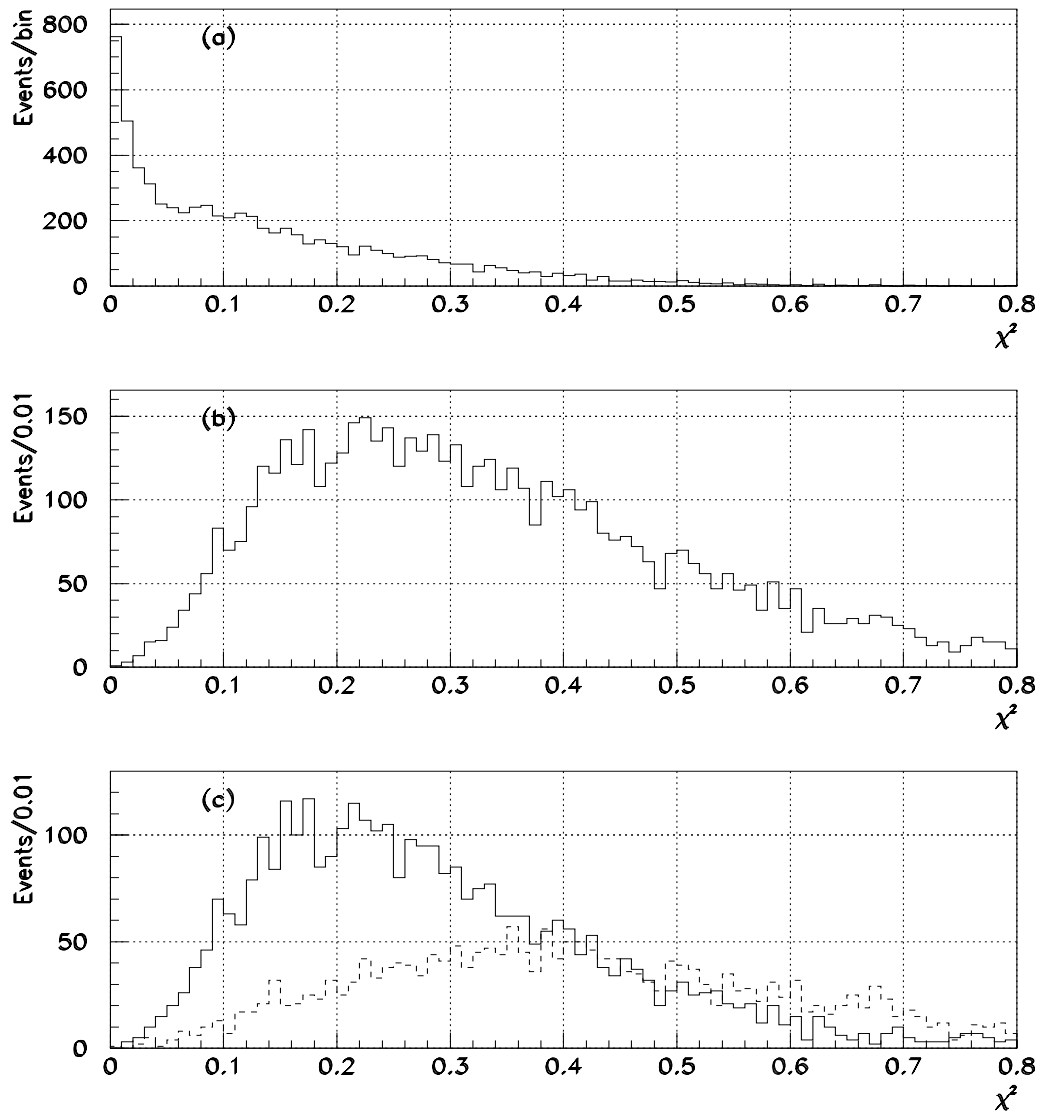


Figure 4.5: Comparison of χ^2 distributions for muon tracks in SAMUS. (a) Monte Carlo; (b) Muon candidates in real data; (c) Separation of events in (b) into good muons ($E_{\text{had}} > 2$ GeV, solid line) and background ($E_{\text{had}} < 2$ GeV, dashed line).

However, Fig. 4.5(c) shows that there is some significant difference on the χ^2 distributions for good muons ($E_{\text{had}} > 2$ GeV) and background ($E_{\text{had}} < 2$ GeV). Therefore, we decided to apply a cut on the χ^2 distribution, with only a marginal effect on

data. This cut represents a requirement based on track fit quality, which is not emphasized in the other cuts. A cut on $\chi^2 < 0.6$ has the purpose of discarding only those few events with very bad track fits.

A total of 3,710 muons satisfy all the above requirements, so they constitute our basic data sample². The distributions of transverse momentum and pseudo-rapidity for this basic sample are shown in Fig. 4.6. Sub-figure (b) shows $|\eta_\mu|$, for better statistics, as it does not matter which side of the detector the muon went through.

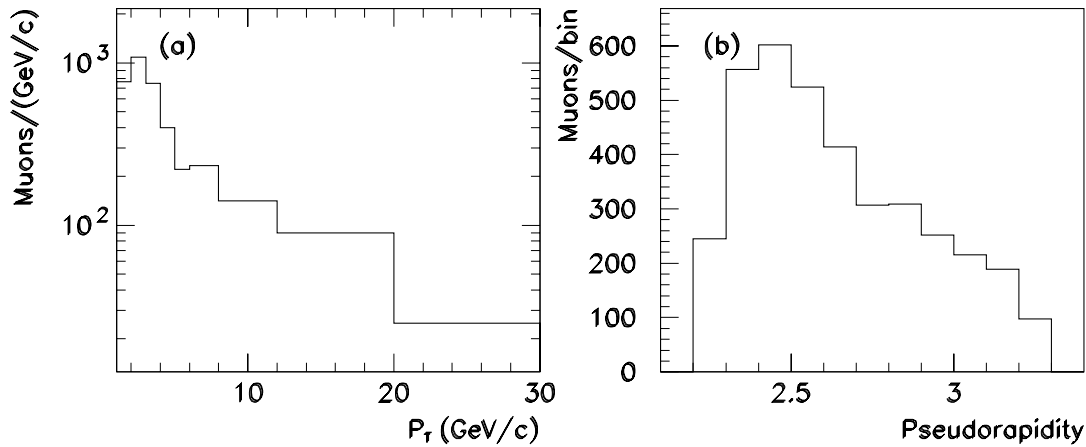


Figure 4.6: Some muon distributions after muon identification cuts. (a) transverse momentum and (b) pseudo-rapidity.

Experimentally, the $dN/dp_{T\mu}$ distribution comes from the histogram shown in Fig. 4.6, dividing the number of muons N_i in each p_T bin by the p_T range for that bin (bin width), as the bins are not equidistant. We chose to use variable bin widths to reduce statistical errors at high- p_T , and also because this region is largely affected by the smearing due to SAMUS momentum resolution (see section 4.7).

4.4 Efficiencies

The experimental determination of the inclusive muon cross section σ_i^μ is done for each p_T bin, from the number of muons N_i observed in that particular bin, through the expression:

$$\sigma_i^\mu = \frac{N_i - B_i}{\varepsilon \int \mathcal{L} dt} \quad (4.4)$$

²Note however that a last cut, the fiducial cut on muon detection efficiency, will be applied later

where B_i is the estimated fraction of background for bin i , ε is the global detection efficiency for muons in SAMUS, and $\int \mathcal{L} dt$ is the total integrated luminosity corresponding to the analyzed data sample.

The most important step to convert dN/dp_{T_μ} in $d\sigma^\mu/dp_{T_\mu}$ is in the determination of the global detection efficiency, ε . It is essential that each source of detection inefficiency is analyzed and estimated, and its effect included into ε .

The Monte Carlo data sample is usually the main source of information for the estimation of the many contributions to the detection efficiency, which is estimated by comparing the number of events passing and failing each selection criteria (cut):

$$\varepsilon_{\text{MC}}(\text{corte}) = \frac{N(\text{pass})}{N(\text{pass}) + N(\text{fail})} \Big|_{\text{MC}} \quad (4.5)$$

As a cross check, the same calculation is performed using the real data sample, assuming that after off-line cuts, it is a background-free sample:

$$\varepsilon_{\text{dados}}(\text{cut}) = \frac{N(\text{pass})}{N(\text{pass}) + N(\text{fail})} \Big|_{\text{data}} \quad \varepsilon_{\text{MC}}(\text{cut}) = \frac{N(\text{pass})}{N(\text{pass}) + N(\text{fail})} \Big|_{\text{MC}} \quad (4.6)$$

Typically, the real efficiency of any cut should be less than ε_{MC} , as the Monte Carlo is an ideal situation (many inefficiency sources are not properly simulated). On the other hand, as the data sample after final cuts does have some background in it, and any cut should be harder to background than to real muons, it follows that the real efficiency for that cut should be higher than $\varepsilon_{\text{dados}}$. Combining the two assertions above, we find that:

$$\varepsilon_{\text{dados}} < \varepsilon_{\text{real}} < \varepsilon_{\text{MC}}, \quad \forall \text{ cut} \quad (4.7)$$

This is a valuable constraint we have to check how reliable our efficiency estimations are for each cut, specially when ε_{MC} and $\varepsilon_{\text{dados}}$ are close values. When they are not close to each other, we should be more careful in estimating $\varepsilon_{\text{real}}$.

Tab. 4.2 shows the values found for the efficiency estimations of all event selection criteria. For all listed criteria, we assume that there is no dependence on kinematical muon variables, like p_{T_μ} or η_μ .

To choose a value for $\varepsilon_{\text{real}}$, each cut was analyzed carefully. For χ^2 , the value 0.96 was taken, as this variable is not well represented in Monte Carlo. For the cut on energy deposition, we note that the presence of other particles close to a muon makes it more likely to pass the cut, instead of less likely. This is the reason why $\varepsilon_{\text{dados}}$ is higher than ε_{MC} , so the value 0.94 was taken. For the cut on N_{hits} , the large difference between ε_{MC} and $\varepsilon_{\text{dados}}$ recommended a more careful procedure for estimating its efficiency.

Estimation based on	ε_{MC}	$\varepsilon_{\text{dados}}$	$\varepsilon_{\text{real}}$
On-line selection (extra factors)			
K_{L1} Multiplicity cut (L1)		0.46	0.46
K_{L2} Calorimeter confirmation (L2)		0.94	0.94
Off-line selection			
$N_{\text{hits}} \geq 16$	0.99	0.85	0.90
$E_{\text{had}} > 2 \text{ GeV}$	0.91	0.94	0.94
$\chi^2 < 0.6$	0.99	0.96	0.96
$\varepsilon_{\text{offline}}$			0.81

Table 4.2: Efficiency estimations for many selection criteria, using both Monte Carlo and real data. The last column shows the values taken for each criterion, as described in the text.

This procedure, illustrated in Fig. 4.7, consists in taking the ratio of histograms before and after the $N_{\text{hits}} > 16$ cut, and fit the region around the peak by a constant. The fitted value, $\varepsilon_{N_{\text{hits}}} = 0.90$, is taken as the best estimation for the efficiency studied. As expected, the low- E_{had} region is cut harder by the cut, while the high- E_{had} region is not statistically significant to be used in the fit.

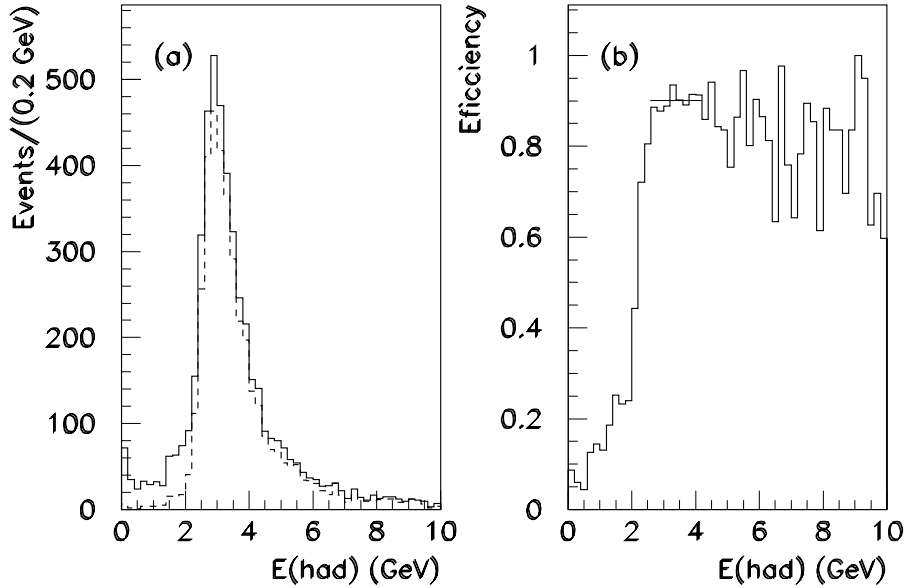


Figure 4.7: Estimation procedure used for the efficiency of the cut $N_{\text{hits}} > 16$. (a) E_{had} distributions before and after the cut on N_{hits} . (b) Ratio of the two histograms in (a), where the peak region was fitted to a constant.

Other inefficiency sources, like geometrical acceptance, trigger (levels 1, 1.5 and 2) and reconstruction, were studied carefully in gigantic Monte Carlo samples^[54]. They were found to be strongly dependent on the muon kinematical variables (momentum p_{μ} ,

pseudo-rapidity η_μ , azimuth ϕ_μ and electrical charge q). The combined effect of these efficiencies, $\varepsilon_{\text{Trig.Reco}}(p_\mu, \eta_\mu, \phi_\mu, q)$, was studied and the results were coded into a set of routines, which were then used to determine these efficiencies in an individual basis, for each muon.

In Fig. 4.8 one can see the spatial dependence of $\varepsilon_{\text{Trig.Reco}}$, for three different combinations of muon energy and electrical charge. In these plots, X and Y represent the cartesian coordinates, as defined in the $D\bar{O}$ global coordinate system (see Fig. 3.11), as if one is at the center of the detector, and one is looking at the south A-station ($z_A = 4.244m$). The density of points in (a) is proportional to $\varepsilon_{\text{Trig.Reco}}$ in each point, while for plots (b-d) this spatial dependence is illustrated as contour plots (note that (a) and (b) are equivalent). The contour plots shown represent those points of the $\varepsilon_{\text{Trig.Reco}}(X, Y)$ surface where it reaches a given value (0.20 for the solid line, 0.05 for the dashed line).

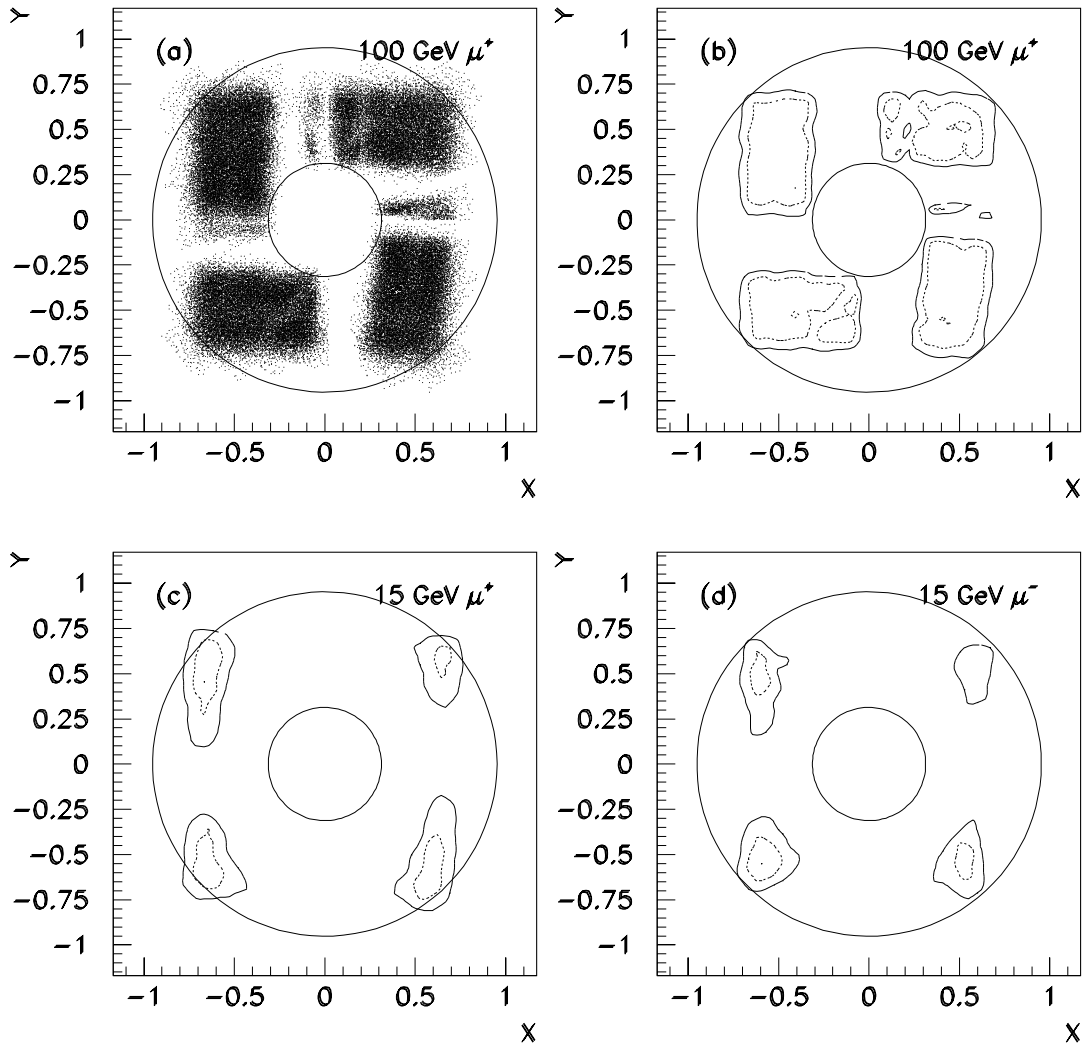


Figure 4.8: Spatial dependence of $\varepsilon_{\text{Trig.Reco}}$, in cartesian coordinates, for different combinations of muon momentum and electrical charge: (a) 100 GeV μ^+ , shown as a scatterplot; (b) The same as in (a), shown as a contourplot; (c) Contourplot for 15 GeV μ^+ ; (d) Contourplot for 15 GeV μ^- . As mentioned in the text, the contours shown represent limits of the fiducial cut, as described in next section.

One can clearly notice the existence of four efficient regions ($\sim 70\%$), separated by regions where the efficiency falls to zero. The low efficiency for these regions is due to programming mistakes for tables of level 1.5 trigger. Actually, these mistakes were primarily due to out-of-date documentation existing for the definition of level 1 muon trigger quadrants in SAMUS trigger region. Those tables were used at the collection of the data samples used at the present analysis. The programming bugs were recently fixed, and more data shall be available for analysis soon.

4.4.1 Fiducial Cut on Detection Efficiency

According to Eq. 4.4, each event which goes into the σ_i^μ cross section calculation is histogrammed according to a weight proportional to $1/\varepsilon_{\text{Trig.Reco}}$. Fig. 4.9(a) shows the $\varepsilon_{\text{Trig.Reco}}$ distribution for the muon candidates surviving the off-line cuts. One can see that many events are reconstructed in those regions where the on-line efficiency is zero, or very close to zero. These events might be removed from the analysis, as they do not contribute to the cross section (zero efficiency muons) or contribute with very large and unreliable weights (low efficiency muons). These events were removed by a fiducial cut, where we demand that each muon candidate has a minimum associated value for the detection efficiency, so that this muon can be safely used in the σ_i^μ calculation.

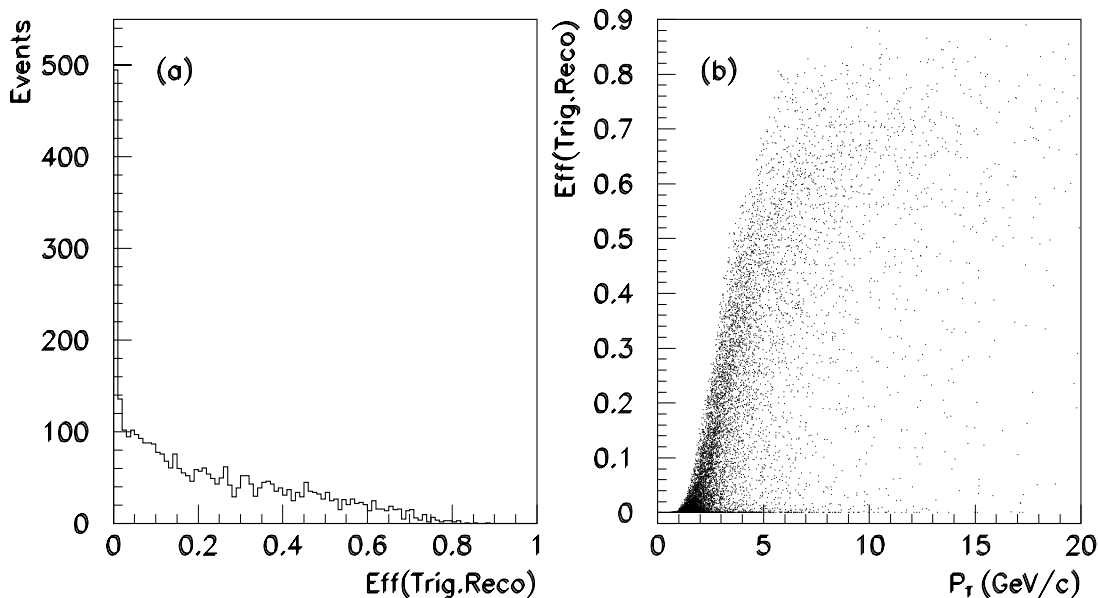


Figure 4.9: $\varepsilon_{\text{Trig.Reco}}$ distributions for muon candidates after off-line cuts. (a) Many muons are reconstructed in low $\varepsilon_{\text{Trig.Reco}}$ regions. (b) A lower cut in $\varepsilon_{\text{Trig.Reco}}$ indirectly corresponds to a lower cut on transverse momentum.

This requirement is equivalent to a fiducial cut, in the sense that any (η, ϕ)

combination pointing to a region where $\varepsilon_{\text{Trig.Reco}}$ is lower than a certain threshold, is unconditionally discarded from the analysis. One also see in Fig. 4.9(b) that a lower limit on $\varepsilon_{\text{Trig.Reco}}$ corresponds to a lower limit on the transverse momentum. This correlation is due to the transverse momentum threshold associated to the trigger logic.

As for any fiducial cut, the correction to this cut on $\varepsilon_{\text{Trig.Reco}}$ is done based on the corresponding fiducial acceptance (\mathcal{A}), defined as the ratio between the area in SAMUS stations kept by the fiducial cut (A_{fid}) and the total area of the analysis (A_{tot}):

$$\mathcal{A} = \frac{A_{\text{fid}}}{A_{\text{tot}}} \quad (4.8)$$

where A_{tot} corresponds to the region limited by the circles of Fig. 4.8. Note that the circles represent the pseudo-rapidity limits 2.2 and 3.3 of our analysis.

Fig. 4.10 shows graphically the \mathcal{A} dependence on the electrical charge and momentum of the muon, for three typical values of the fiducial cut. Note the distinguishing behavior between the monotonically increasing curve for μ^- and the maximum for μ^+ . This fact is due to the particular configuration of the magnetic field inside the SAMUS toroids, which at the south side kicks μ^+ 's towards the beamline and μ^- 's outwards. At the north side, the same fact occurs contrariwise, favoring the detection of negatively charged muons. Note also that, as the muon momentum increases, \mathcal{A} tends to the same asymptotic value for both μ^+ 's and μ^- 's, as it should, as the magnetic deflection is smaller for more energetic particles.

To evaluate the stability of the fiducial cut correction, we studied the variation of σ_i^μ in each $p_{T\mu}$ bin, as a function of the value chosen for the fiducial cut. In the ideal case (infinite statistics and perfect knowledge of $\varepsilon_{\text{Trig.Reco}}$, an increase on the value chosen for the fiducial cut would reduce the number of events contributing to the muon cross section in a given p_T bin. But \mathcal{A} would also be reduced in the same proportion, so that the cross sections in any p_T would not change. That means σ_i^μ would not depend on the value chosen for the fiducial cut.

Fig. 4.11 shows the variation of σ_i^μ in each p_T bin, as a function of the value chosen for the fiducial cut, as calculated from our data sample after off-line cuts. In the general case, the curves seem to follow some pattern: it increases slowly at the beginning, flattening out at a certain point, and then falling off quickly to zero.

The first tendency, of a slow and steady increase, reflects the finite character of our sample, as no event is lost due to the increase on the fiducial cut. Thus the reduction on \mathcal{A} forces σ_i^μ to increase slowly. The second tendency is the expected stability plateau, mentioned in the previous paragraph as the ideal behavior. The third part corresponds to the point where the fiducial cut drastically reduces the event population of each p_T bin, due to the mentioned correspondence between fiducial cut and a transverse momentum cut (see Fig. 4.9(b)). The drastic population reduction in a p_T bin makes the cross section in that bin fall to zero. We should take this fact into account when choosing the value of

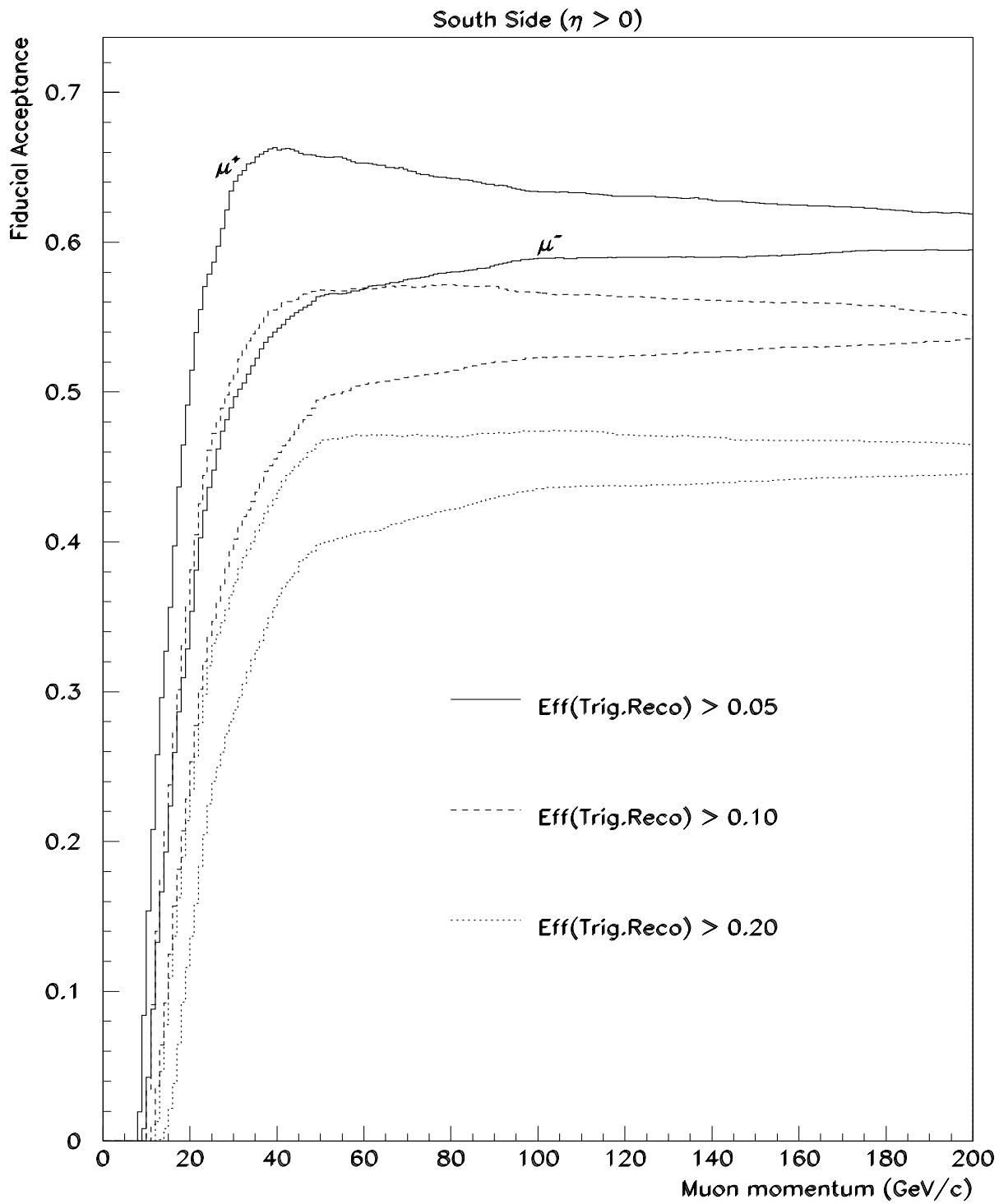


Figure 4.10: Acceptance of the fiducial cut, based in the fractional area kept by the fiducial cut (inside the contours) with respect to the total analysis area (between circles).

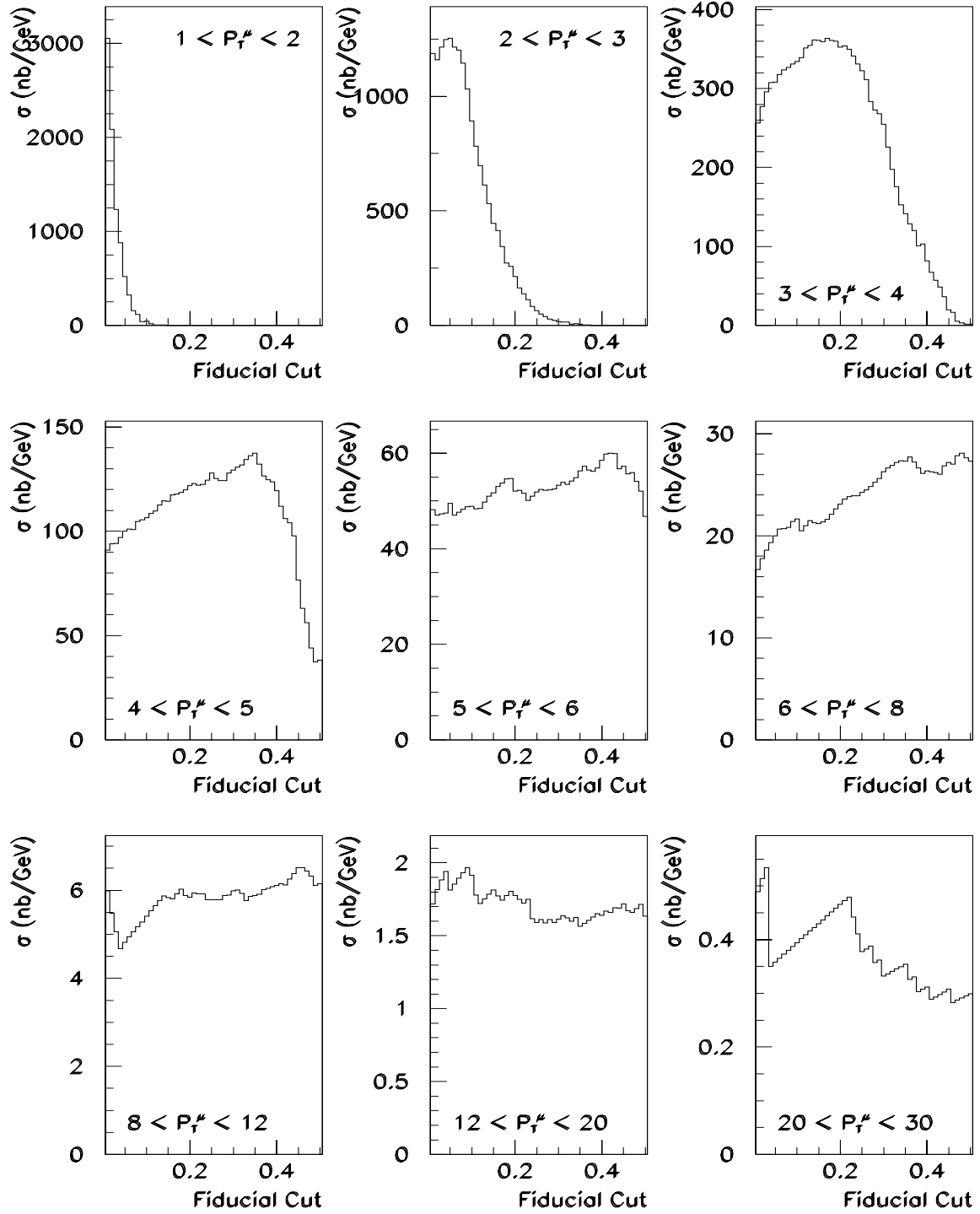


Figure 4.11: Cross section variations as a function of the value chosen for the fiducial cut, for each p_T bin used in the data treatment.

the fiducial cut, to avoid being caught into this third regime.

Analyzing Fig. 4.11, one sees that the first p_T bin is on the third regime from the beginning, and this should be interpreted as the current inability of DØ detector to extract physical measurements using forward (SAMUS) muons with transverse momentum below 2 GeV/c.

For the other p_T bins, the fiducial cut values were chosen so that the cross sections in each bin are kept in the stability plateau. We chose the lower limits on $\varepsilon_{\text{Trig.Reco}}$ as 0.05 for $2 < p_T < 3$ GeV/c, and 0.20 for $p_T > 3$ GeV/c.

Keeping in mind the cross section calculation (Eq. 4.4), we need to estimate the amount of background in our data sample. This is the subject of the following section.

4.5 Backgrounds

Despite all off-line cuts applied with the purpose of background rejection, there will always be some residual background in the data sample. We need a reliable estimation method for the amount of background (B) in our sample, so that we can subtract its effect from the cross section calculation.

The most important background source to muons in SAMUS region comes from accidental combinations of hits forming spurious tracks. The spurious tracks tend to be composed of a smaller number of hits than tracks from real muons. Also, spurious tracks in general do not have calorimeter confirmation.

Fig. 4.12 shows the distributions of E_{had} , the energy deposited in the hadronic calorimeters along the muon trajectory, for real data, and compares good muon candidates to those where less than 16 hits were used in the muon track fit.

Assuming that the low- E_{had} region is totally due to combinatorial background, one can estimate B by normalizing the two histograms in the low- E_{had} region, and comparing the areas in each histogram for E_{had} values above 2 GeV. This procedure is illustrated in Fig. 4.12(c), where the normalized background distribution is shown by the dashed line. One finds an estimation of $B = 2.3\%$ for the background fraction in the data sample after off-line cuts.

A similar process can be used also for the other muon quality variable, N_{hits} . In this case, we used E_{had} as the control variable, defining “good muons” and “background” as those muon candidates where $E_{\text{had}} > 2$ GeV and $E_{\text{had}} < 2$ GeV, respectively. There is a large overlap between the N_{hits} distributions for good muon candidates and for background, but one assumes that each distribution individually can be well represented by a gaussian. We therefore fit the histograms using gaussian functions to represent each of the contributions separately.

First we fitted the background distribution by a gaussian $g_b(x)$ (see Fig. 4.13).

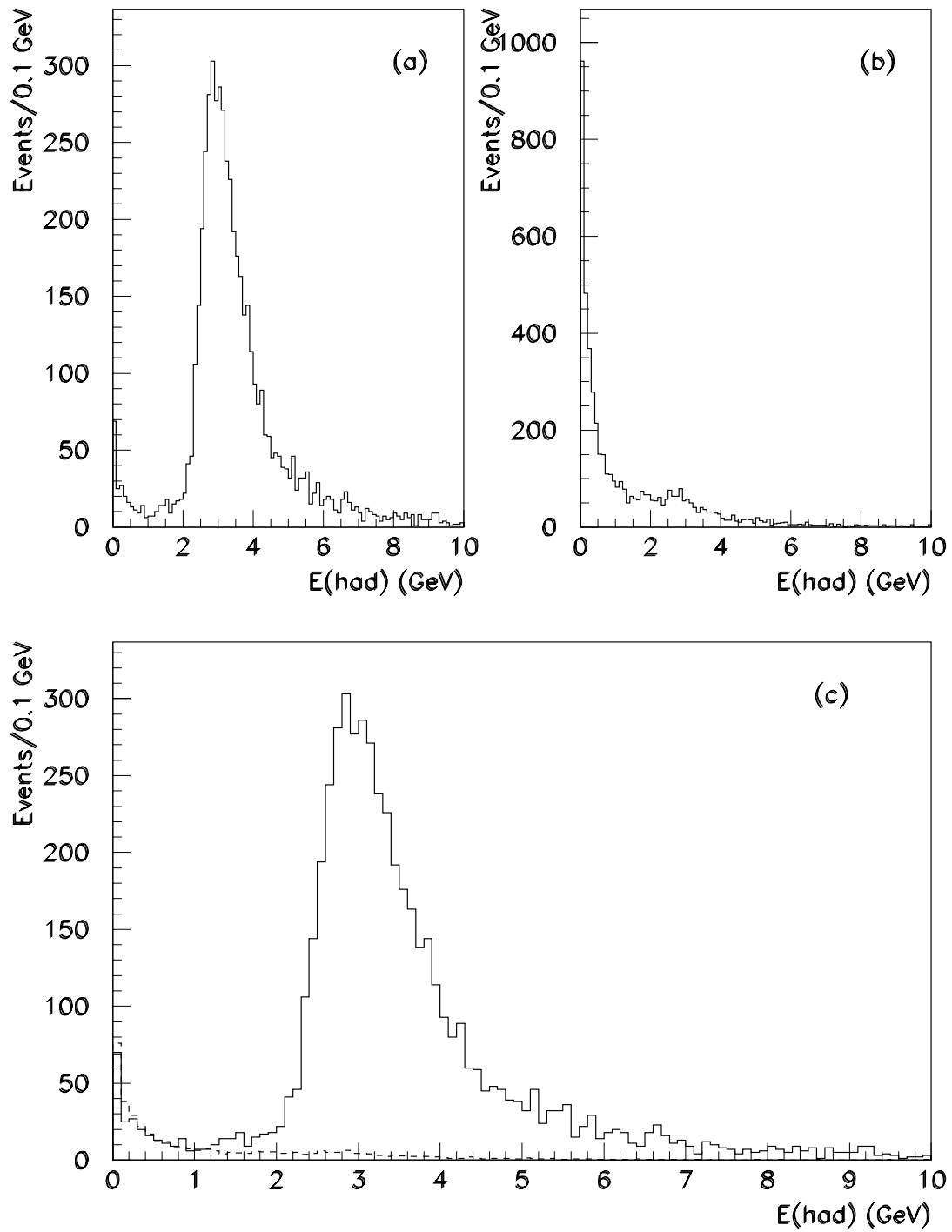


Figure 4.12: Estimation of the background fraction based on the energy (E_{had}) deposited in the hadronic calorimeters: (a) muon candidates after off-line cuts; (b) muons with less than 16 hits along the muon track; (c) background estimation procedure, as described in the text.

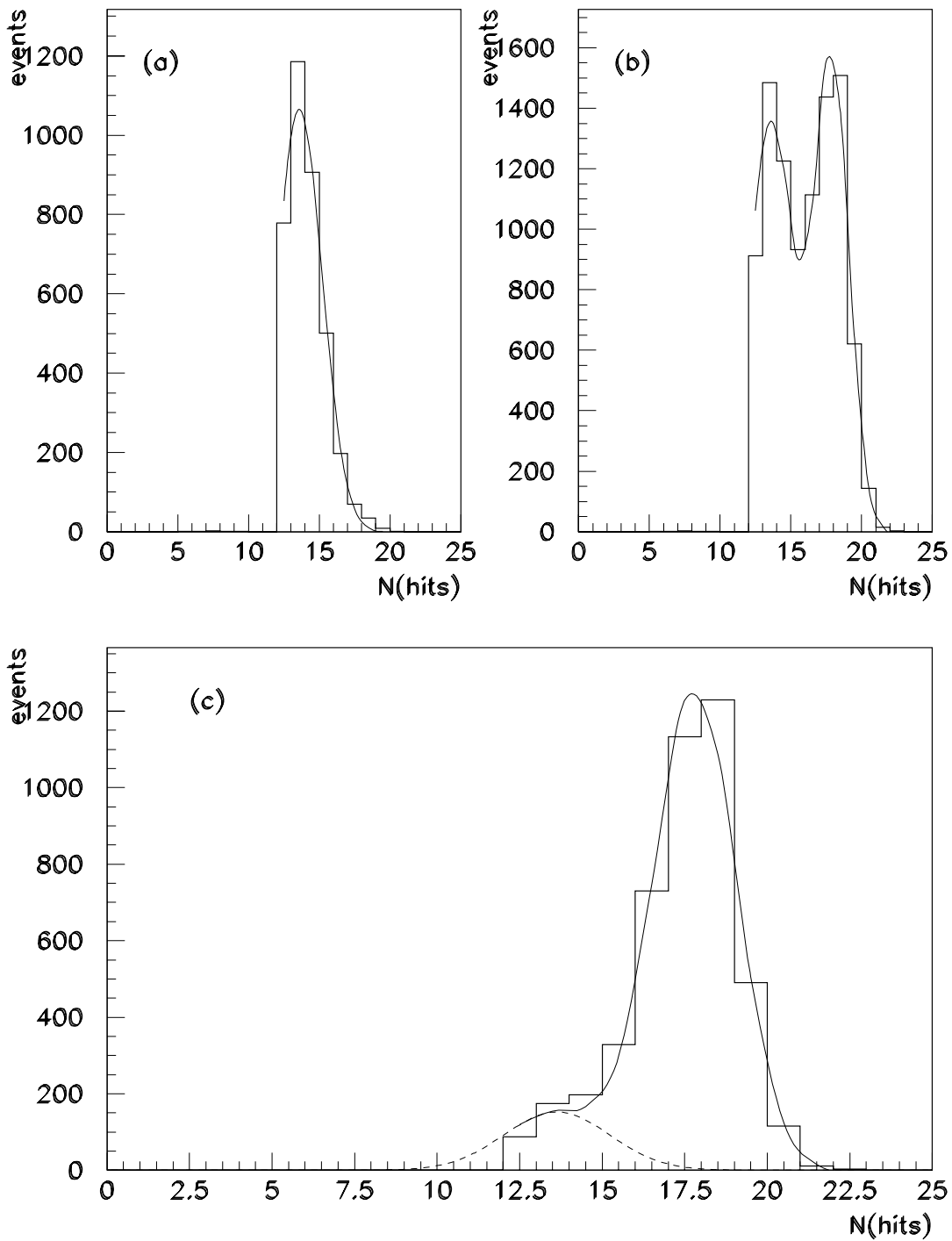


Figure 4.13: Using the N_{hits} distribution for an independent estimation of the amount of background in our data sample, after off-line cuts: (a) N_{hits} distribution for background ($E_{\text{had}} < 2 \text{ GeV}$); (b) real data before off-line cuts; (c) Background estimation procedure, as described in the text.

Then we fixed the mean and width of $g_b(x)$, leaving only its amplitude as a free parameter, and fitted the distribution of Fig. 4.13(b) to obtain the parameters of the second gaussian, $g_\mu(x)$. Finally, we applied the off-line cuts and fitted the histogram of Fig. 4.13(c). This procedure gives us another estimation for B , from the area under the first gaussian, $g_b(x)$, in the region $N_{\text{hits}} \geq 16$. The procedure is illustrated in Fig. 4.13, and the resulting background fraction was found to be $B = 1.2\%$, which is compatible to the value found from the E_{had} distribution.

There are also other background sources, such as beam halos, cosmic rays, punchthrough, etc. However it is estimated that, in SAMUS region, all these contributions are negligible when compared to the combinatoric background just estimated. This latter, on its turn, is so small as compared to some of the uncertainties involved (see section 4.8), that we have decided not to do any background subtraction in the present analysis. We will just neglect the background fraction in our data sample, as far as cross section determination is concerned, setting $B_i = 0$ in Eq. 4.4.

4.6 The Experimental Spectrum

With all the information accumulated up to here, we are almost ready to calculate the forward differential inclusive muon cross section $d\sigma^\mu/dp_{T_\mu}$, using Eq. 4.4. The integrated luminosity was estimated in Tab. 4.1. The background contamination will be neglected.

The global muon detection efficiency (ε) is estimated from the product of the efficiencies associated to each on-line and off-line selection criteria, with the addition of the two extra factors mentioned in Tab. 4.2, which account for corrections to the on-line efficiency:

$$\varepsilon_{\text{online}} \equiv K_{L_1} K_{L_2} \varepsilon_{\text{Trig.Reco}} \quad (4.9)$$

and therefore, considering the efficiencies for off-line selection criteria, and also the fiducial cut correction, we find the global muon detection efficiency in SAMUS region, given by:

$$\varepsilon = K_{L_1} K_{L_2} \varepsilon_{\text{offline}} \varepsilon_{\text{Trig.Reco}}(p, \eta, \phi, q) \mathcal{A}(p, q) \quad (4.10)$$

where p , η , ϕ and q represent respectively the momentum, pseudo-rapidity, azimuth and electrical charge of each muon individually.

Substitution of the above estimates on Eq. 4.4 gives us the conversion of dN/dp_{T_μ} to $d\sigma^\mu/dp_{T_\mu}$. Therefore, dividing both sides of the resulting equation by the total pseudo-rapidity interval ($\Delta\eta$) used in our analysis, we find the experimental spectrum $d\sigma^\mu/dp_{T_\mu} \Delta\eta$, which is shown graphically in Fig. 4.14. This result is presented in the form of a variable-bin histogram.

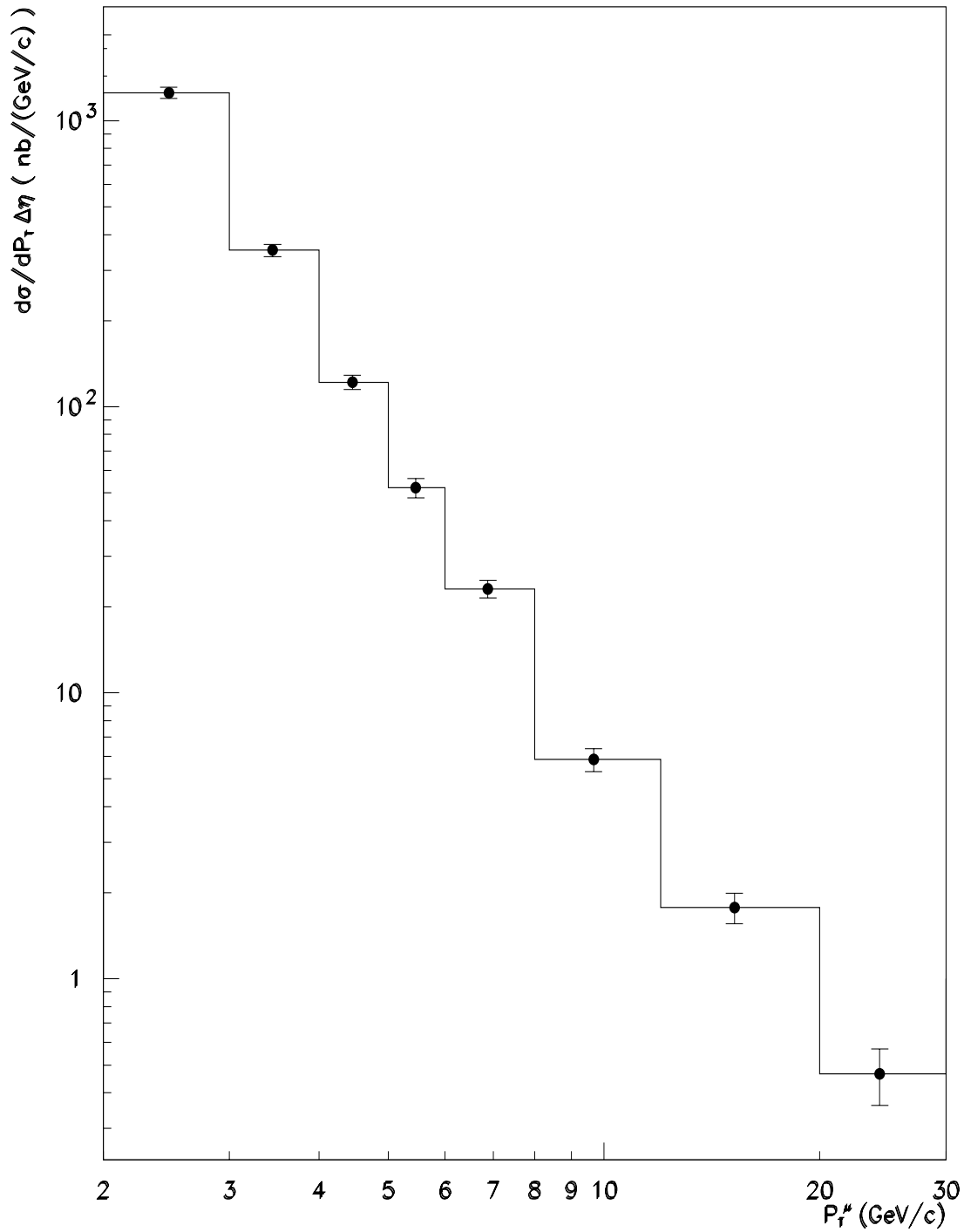


Figure 4.14: The experimental spectrum found for the inclusive differential cross section for small angle muons, presented as a variable-bin histogram. Using the prescription of Ref. [55], we replace this histogram by the experimental points, shown here with statistical error bars only.

In the following section we discuss a last treatment which needs to be done to the differential inclusive muon cross section spectrum presented, namely the correction for muon momentum resolution in SAMUS region. For the purpose of this correction, we need to associate each p_T bin to a given abscissa.

Using the center of each bin as abscissa is not recommended in such a case, where we have large bins and a steeply falling $d\sigma^\mu/dp_{T\mu}\Delta\eta$ spectrum. Lafferty and Wyatt^[55] suggest to use the abscissa x_{lw} , such that:

$$f(x_{lw}) = \frac{1}{\Delta x} \int_{x_l}^{x_h} f(x) dx \quad (4.11)$$

where x_l and x_h are the lower and upper limits of each p_T bin respectively, $\Delta x \equiv x_h - x_l$ and $f(x)$ is the theoretical distribution (see Fig. 2.7) after being smeared due to poor muon momentum resolution in SAMUS region. Note that, as we shall see in the following section, we shall not use the theoretical function $F(x)$ (solid line in Fig. 2.7) directly in Eq. 4.11, as it must not be compared directly to experimental data. We must use the smeared function $f(x)$ instead.

Therefore, we represent the experimental spectrum by nine points, whose ordinates are the differential cross section in each p_T bin, and whose abscissae are calculated by Eq. 4.11. These data points are also shown in Fig. 4.14, with the corresponding statistical error bars.

4.7 Momentum Resolution

An important problem related to the observation of muons in DØ spectrometer is the degradation of their measured momenta. This means that the measured muon momentum is not exactly equal to its real momentum, but it is distributed around the actual value of this momentum, according to some probability distribution function.

The degradation on the muon momentum measurement at DØ can be ultimately attributed, in first place, to the absence of magnetic field in the volume of the DØ tracking system, which prevents us of using the central detector information for the momentum determination of any charged particles. To reach the inner layers of the muon system, muons have already traversed a large number of radiation lengths (central detector, calorimeters, etc.) and are thus subject to multiple Coulomb scattering. Besides that, alignment and chamber positioning uncertainties in the muon system also contribute to the poor momentum resolution, specially in the region of high momenta, where the muon trajectory is almost rectilinear.

All these effects must be taken into account before we can make a comparison between the experimental spectrum and the theoretical predictions. The muon momen-

tum resolution in SAMUS region was estimated^[56] via the simulation of isolated muons through the DØGeant package (see section 3.4.3), for five different values of muon transverse momentum. Comparing the original and reconstructed momenta, we have an estimation for the muon momentum resolution in SAMUS. The momentum resolution gets worse as the muon momenta increase, as one can see in Fig. 4.15.

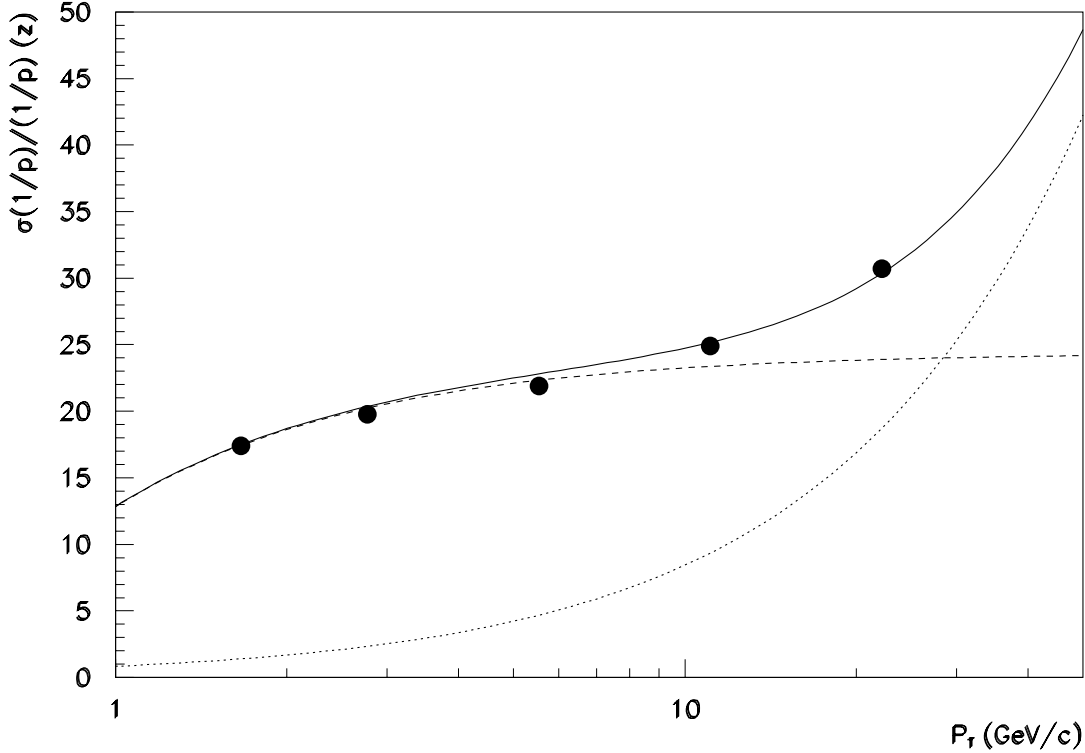


Figure 4.15: The muon momentum resolution in SAMUS region, as a function of transverse momentum (adapted from [56]). The dashed (dotted) line represents the contribution from multiple Coulomb scattering (alignment and positioning uncertainties of SAMUS stations). The solid line is the quadratic sum of these independent contributions.

Thereafter, all five points thus obtained were fitted to a function of transverse momentum, which represents the momentum resolution function in SAMUS:

$$\frac{\sigma(1/p)}{1/p} = \sqrt{\sigma_{\text{Coul}}^2 + \sigma_{\text{Posic}}^2} \quad (4.12)$$

where σ_{Coul} and σ_{Posic} are respectively the contributions from multiple Coulomb scattering and from alignment and positioning of SAMUS stations, represented by:

$$\sigma_{\text{Posic}} = 0.845p_T \quad \text{e} \quad \sigma_{\text{Coul}} = 24.4 \left(1 - \frac{0.475}{p_T}\right) \quad (4.13)$$

The experimental spectrum of Fig. 4.14 was corrected using a procedure described by Elvira *et al.*^[57], which consists basically in taking a functional form $F(p_T, \alpha_i)$ which contains N free parameters α_i , and able to fit the expected spectrum (solid line of Fig. 2.7). The function F is convoluted with a function $G(p'_T - p_T)$, generating a smeared function, $f(p'_T, \alpha_i)$, which represents the experimental distribution including effects due to the detector resolution. The smeared function f depends on the same N free parameters as the function F :

$$f(p'_T, \alpha_i) = \int G(p'_T - p_T) F(p_T, \alpha_i) dp_T \quad (4.14)$$

where the smearing function $G(p'_T - p_T)$ is a gaussian of width $\sigma(1/p)$ given by Eq. 4.12.

The experimental points are fitted by the smeared function $f(p'_T, \alpha_i)$, and from this fit we obtain estimates for the N free parameters α_i . The substitution of these parameters back in $F(p_T, \alpha_i)$ gives us the corrected distribution which, after the smearing $G(p_T)$ due to the muon momentum resolution, best fits the experimental points of Fig. 4.14.

In our case we used a 3-parameters function:

$$F(p_T, \alpha_i) = \frac{\alpha_1}{p_T^{\alpha_2}}, \quad \forall p_T > \alpha_3 \quad (4.15)$$

Note that the parameter α_3 here is just a gross representation for the range-out of low-momentum muons by the material of the endcap calorimeters and SAMUS magnets. As a free parameter, it represents the lower limit of the numeric integration performed in the development of Eq. 4.14. The best estimate for the three free parameters used are presented in Tab. 4.3.

Parameter	Fitted value	Error (1σ)
α_1	2.914×10^5	0.23×10^5
α_2	5.775	0.071
α_3	1.602	0.037

Table 4.3: Fitted values for the three free parameters used in the procedure of correction for the smearing due to muon momentum resolution in SAMUS region.

The results of this correction procedure are shown on Fig. 4.16. The dashed line represents the smeared function $f(p'_T, \alpha_i)$ after the fit to experimental points, which are shown as black circles, with statistical error bars. The solid line represents the corrected distribution, $F(p_T, \alpha_i)$. Note the impact of muon momentum resolution, specially in the high- p_T region, comparing the solid and dashed curves.

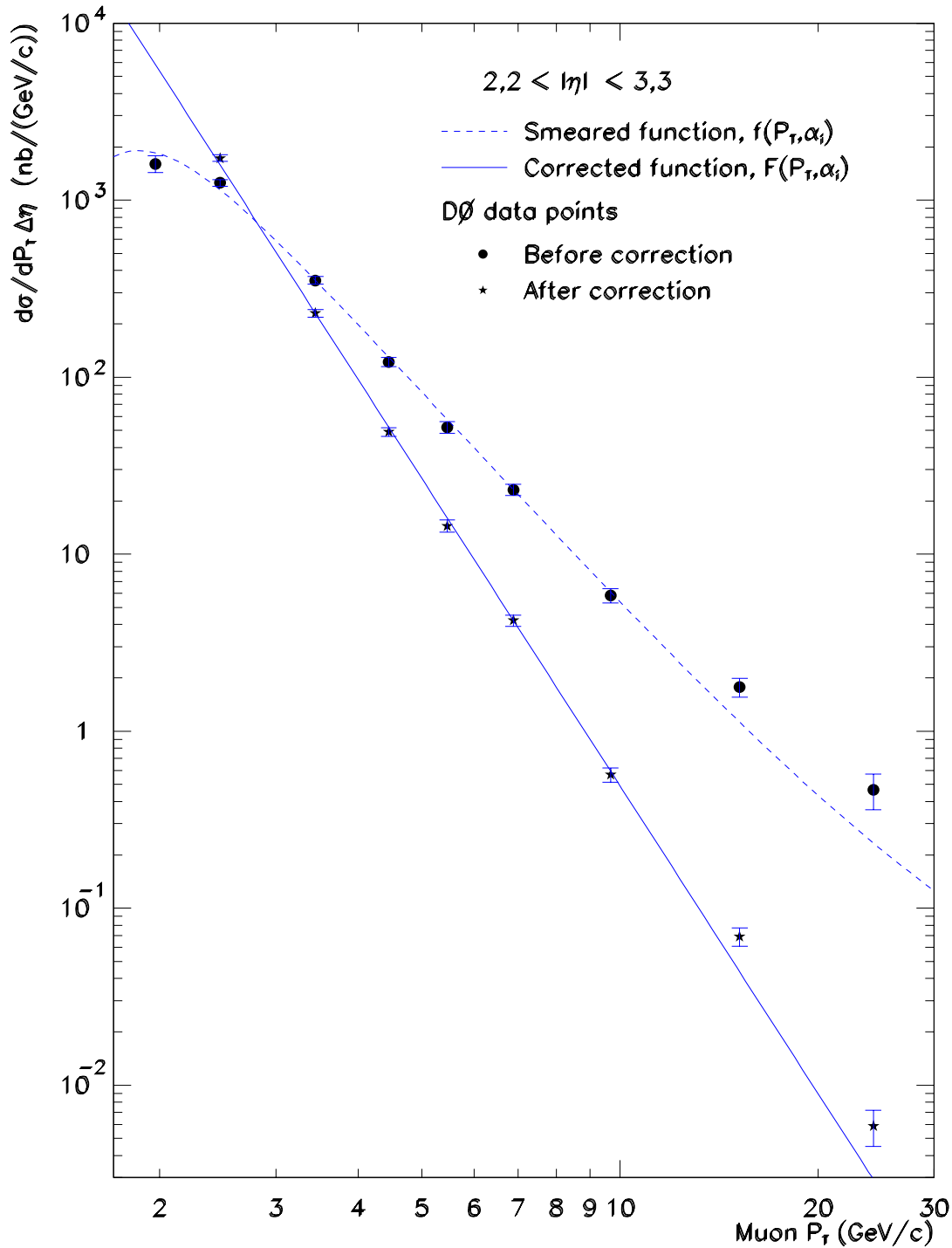


Figure 4.16: Result of the correction procedure for muon momentum resolution in SAMUS. The corrected function $F(p_T, \alpha_i)$ is represented by the solid line. The dashed line represents the smeared function, $f(p_T, \alpha_i)$, which was fitted to the experimental data points. The error bars in the experimental data points represent statistical errors only. The points resulting from the correction procedure are also shown.

From the results of this correction procedure, corrected experimental points can be determined according to the expression:

$$\left. \frac{d\sigma^\mu}{dp_{T_\mu} \Delta\eta} \right|_{\text{corrected}} = \frac{F(p_T, \alpha_i)}{f(p_T, \alpha_i)} \left. \frac{d\sigma^\mu}{dp_{T_\mu} \Delta\eta} \right|_{\text{n\~{a}o corrected}} \quad (4.16)$$

The corrected points thus calculated are also shown in Fig. 4.16, as stars. These points can be directly compared to the theoretical predictions from ISAJET model, presented by the end of chapter 2. Before this comparison, however, let us briefly discuss the treatment of systematical errors involved in our analysis.

4.8 Systematical Error Analysis

There are many possible sources of systematical uncertainties in the results of the present analysis. In this section we briefly describe the main sources, and we will make an estimation of their influence on the final results.

One of the most important sources of systematical errors is the integrated luminosity measurement corresponding to the collected data sample. The luminosity is measured at DØ by the level 0 scintillating hodoscopes, and these measurements have an associated uncertainty estimated in 12%. This contribution obviously does not depend on p_{T_μ} .

The background fraction in our final data sample was estimated in about 2.3%. As no subtraction procedure was performed, this value is directly taken to be an estimation of the systematical errors associated to the amount of background in our final data sample.

The systematical errors associated to the fiducial cut correction were estimated from the variations of the cross sections in each p_T bin (see Fig. 4.11), around the chosen values for the fiducial cut.

Another important source of systematical errors is the process of evaluation of uncertainties involved in the muon detection process. The systematical errors associated to $\varepsilon_{\text{Trig.Reco}}$ were taken to be, in each p_T bin, the statistical errors associated to the Monte Carlo sample used for estimating $\varepsilon_{\text{Trig.Reco}}$ [54]. These errors are then combined in quadrature with the errors associated to the determination of the extra factors K_{L_1} and K_{L_2} .

The off-line cuts also have a significant contribution to the total systematical errors. As an estimation to these contributions, we took half of the difference between the estimations based on Monte Carlo and real events. Therefore, the systematical errors associated are probably overestimated, but we decided to be conservative at this point.

All the contributions mentioned above were added in quadrature, as shown on Tab. 4.4.

p_T Bin GeV/c	Error Sources					Partial Systematical Errors
	Integr. Lumin.	Backgr. Contam.	Fiduc. cut	On-line Effic.	Off-line Effic.	
2 - 3	0.12	0.023	0.086	0.12	0.12	0.23
3 - 4	0.12	0.023	0.086	0.055	0.12	0.20
4 - 5	0.12	0.023	0.062	0.043	0.12	0.19
5 - 6	0.12	0.023	0.051	0.038	0.12	0.18
6 - 8	0.12	0.023	0.084	0.035	0.12	0.19
8 - 12	0.12	0.023	0.032	0.033	0.12	0.18
12 - 20	0.12	0.023	0.10	0.032	0.12	0.20
20 - 30	0.12	0.023	0.19	0.032	0.12	0.26

Table 4.4: Details of the analysis of systematical errors associated to the experimental spectrum of Fig. 4.14, before the momentum resolution correction. The word “partial” at the last column means that errors associated to the procedure of momentum resolution correction have not been included so far.

The systematical errors associated to the detector resolution effects have been estimated by using different functional forms for the theoretical distributions, and also considering the effect of even worse momentum resolution effects than the curve shown of Fig. 4.15. The results were added in quadrature with the results of Tab. 4.4, and the numbers are illustrated in Tab. 4.5. The contribution from momentum resolution correction procedure was included separately due to two facts: first, because it does not contribute to the experimental spectrum of Fig. 4.14, as that spectrum does not include any momentum resolution correction. Second, contrary to the other contributions shown at Tab. 4.4, the uncertainties associated to the momentum resolution cannot be significantly reduced, as mentioned later, by the end of this section.

One can notice in Tabs. 4.4 and 4.5 that the largest contributions to the systematical errors come from measurements of integrated luminosity, from estimations for efficiencies of off-line cuts and from the procedure for corrections of detector resolution effects.

The systematical uncertainties associated to off-line cuts can be significantly improved. For this purpose we have to optimize the detector simulation, producing Monte Carlo samples more realistic and better representing real data. This is expected to happen in the medium term future.

It also seems to be possible to reduce the systematical errors associated to the integrated luminosity measurements. This possibility has been analyzed by the specialists, and preliminary results indicate a reduction for the errors in luminosity measurements from 12% to about 5.5%. This will represent a strong reduction on the systematical uncertainties of our results.

p_T Bin GeV/c	Partial Syst.Err.	Syst. Error Mom.Res.Corr.	Total Syst.Error
2 - 3	0.23	0.063	0.23
3 - 4	0.20	0.075	0.21
4 - 5	0.19	0.036	0.19
5 - 6	0.18	0.027	0.18
6 - 8	0.19	0.113	0.22
8 - 12	0.18	0.273	0.33
12 - 20	0.20	0.473	0.51
20 - 30	0.26	0.603	0.66

Table 4.5: Sum in quadrature of the experimental systematical errors (see Tab. 4.4) with the systematical errors associated to the procedure for correction of detector resolution effects.

Finally, the muon momentum resolution in $D\emptyset$ is not expected to improve significantly in the short term future, because it requires big changes in the experimental apparatus itself, replacing the current toroidal magnets by solenoidal superconducting magnets to generate magnetic field in the central region of the detector. This solenoidal magnet is in research and development stage, and it is expected to become operational in Collider Run II, about year 2000.

4.9 Results

In this section we present the final results of the analysis of data collected at the $D\emptyset$ spectrometer, around July 1993, with the purpose of measuring the differential inclusive muon production cross section at the forward region,

$$2 \text{ GeV}/c < p_{T_\mu} < 30 \text{ GeV}/c$$

$$2.2 < |\eta_\mu| < 3.3$$

in $p\bar{p}$ collisions at energies of 1.8 TeV in the center of momentum frame of the proton-antiproton system.

Tab. 4.6 shows the values found for $d\sigma^\mu/dp_{T_\mu}\Delta\eta$, including corrections due to detector resolution effects.

Fig. 4.17 presents graphically the results from Tab. 4.6. The statistical (total) errors are illustrated in the internal (external) error bars. These experimental data points can be directly compared to the theoretical predictions, based on ISAJET model, represented by the dashed line. The shaded band around the dashed line represents an estimation of 40% for the uncertainties associated to these theoretical predictions. One

p_T Bin GeV/c	Abscissa GeV/c	$d\sigma^\mu/dp_{T_\mu}\Delta\eta$ nb/(GeV/c)	Relative Errors		
			Stat.	Syst.	Total
2 - 3	2.47	1730.	0.044	0.23	0.24
3 - 4	3.45	230.	0.049	0.21	0.22
4 - 5	4.46	49.0	0.057	0.19	0.20
5 - 6	5.46	14.5	0.077	0.18	0.20
6 - 8	6.88	4.22	0.072	0.22	0.24
8 - 12	9.67	0.57	0.093	0.33	0.34
12 - 20	15.20	0.069	0.12	0.51	0.53
20 - 30	24.24	0.006	0.23	0.66	0.69

Table 4.6: Numerical values for the differential inclusive muon production cross section in the kinematical region $2.2 < |\eta_\mu| < 3.3$.

can notice that, despite of being compatible at the low p_T region, there is a small disagreement on the slopes of expected and measured spectra, which makes them incompatible at the high- p_T region.

One can notice a small feature in Fig. 4.16: the last two experimental points lie a little above the dashed curve, which properly fitted all other data points. We checked the possibility that those two points could be due to a contribution from leptonic decays of intermediate weak vector bosons W^\pm e Z . ISAJET model for Drell-Yan processes indicated that muons coming from such decays should have a $d\sigma^\mu/dp_{T_\mu}\Delta\eta$ spectrum flat at about 0.003 nb/(GeV/c) in the range $12 < p_{T_\mu} < 40$ GeV/c. One can see that this value is about two orders of magnitude below the numbers corresponding to those last two data points observed in our experimental spectrum (transverse momentum under 30 GeV/c). We thus discard the possibility of contributions due to Drell-Yan processes in the present results.

Finally, we should emphasize that the results presented here constitute the first experimental measurement of the inclusive muon production cross section for the kinematical region $|\eta| > 2.2$. A clean muon sample in such small angles region opens up the possibility for the study of some very interesting topics, including the heavy quark inclusive production cross section in this forward region, and the study of gluon distribution functions inside the nucleons. Presently, among the many operating detectors, DØ spectrometer is the only one able to perform such studies, thanks to its excellent geometrical coverage for muon detection.

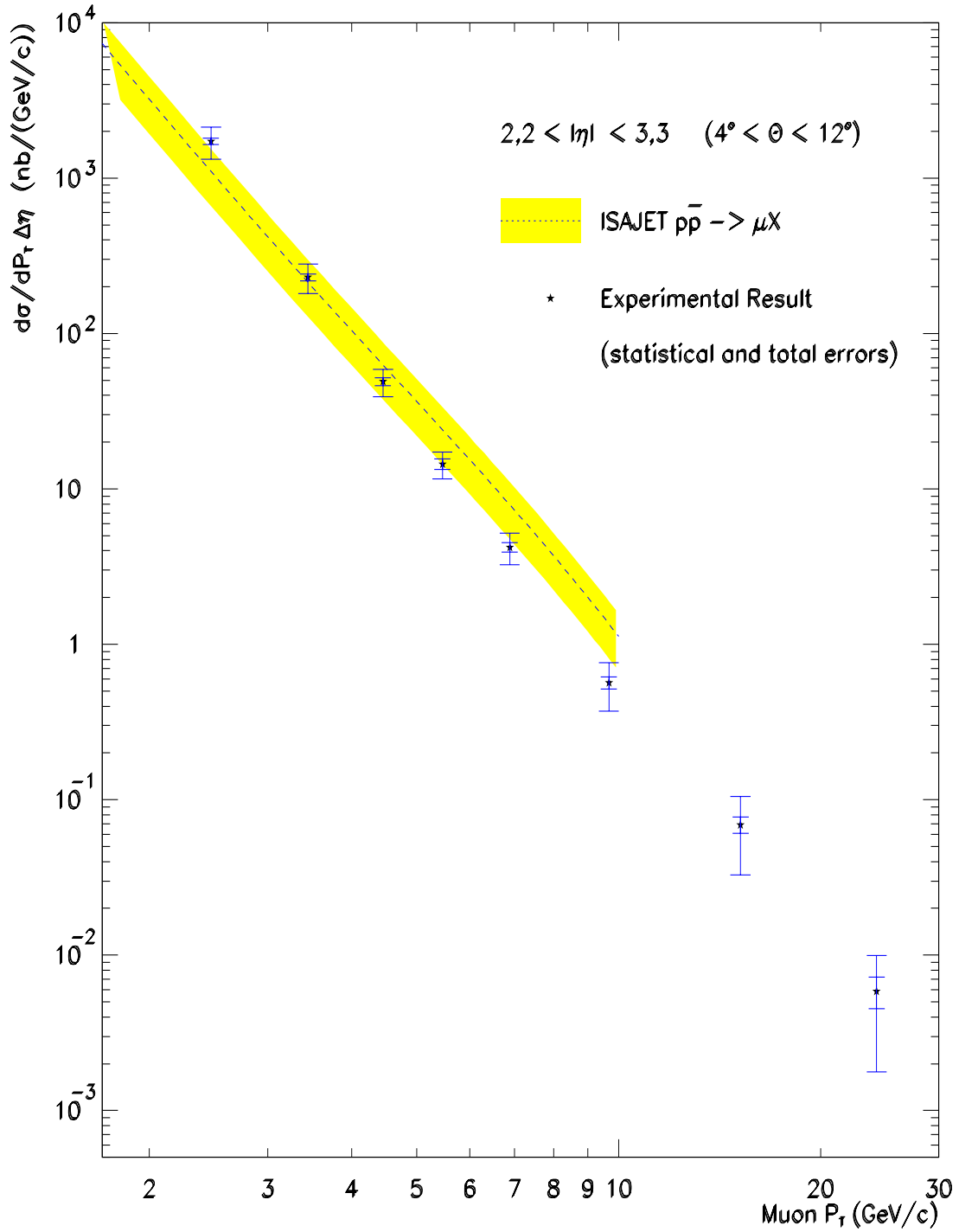


Figure 4.17: Experimental spectrum of the differential inclusive muon production cross section in the kinematical region $2.2 < |\eta| < 3.3$, with statistical and total error (internal and external bars respectively). The shaded band corresponds to theoretical uncertainties of about 40% on predictions from ISAJET model.

Chapter 5

Conclusions

In the present work we present the first experimental measurement of the inclusive muon production cross section (σ^μ) in the forward region:

$$\begin{aligned} 2 \text{ GeV}/c < p_{T_\mu} < 30 \text{ GeV}/c \\ 2.2 < |\eta_\mu| < 3.3 \end{aligned}$$

as well as its dependence with muon transverse momentum, $d\sigma^\mu/dp_{T_\mu} \Delta\eta$.

These measurements are extremely difficult to be performed in hadronic colliders, due to very high background level existing in the proximity of the hadronic beam lines. Therefore, the results presented here were made possible thanks to a good performance of the DØ spectrometer and, in particular, the SAMUS spectrometer (forward muon detection system) and the multilevel trigger system.

Besides the very high background level, many other difficulties had to be faced, most of them inherent to any detector in its first round of data collection. Some examples of such difficulties in our analysis were the continuous evolution of the small angle muon trigger system, which was subject to many upgrades along its operation, with the purpose of higher muon detection efficiencies and higher rejection of combinatorial background. It's very gratifying to realize that our contribution to the development of the muon trigger system was essential for the results here presented.

The detector simulation packages are another example of difficulty faced in this analysis. These packages have to be tuned to correctly reproduce the detector effects over the simulated events. A great deal of work is still needed, specially regarding the modeling the high background level present in SAMUS region, allowing one to generate Monte Carlo samples which can reliably describe real data.

In section 4.9, we made a compared our results to the theoretical expectations, based on unbiased ISAJET NLO model for heavy quark production and decay. This comparison pointed to a small discrepancy in the slopes of measured and predicted spectra.

From the physics point of view, this discrepancy may have some origins. For instance, the ISAJET model's way to deal with NLO processes is not rigorous, but some kind of approximation. Also, the parameterization used in ISAJET for the gluon distribution functions inside the proton may be far from the true values, and this fact may strongly affect the heavy quark production through processes like $gg \rightarrow gg$, as pointed out in Eq. 2.19. Other sources of uncertainty, such as hadronization and semileptonic quark decay models, may also contribute to the observed discrepancy.

The last two data points in Fig.4.17 lie a little above the fitted function. We tested the hypothesis of an excess of events due to leptonic decays of the weak bosons W^\pm and Z . The simulation showed that this contribution would be about two orders of magnitude below the observed data points, then this hypothesis was discarded.

The systematical errors in our results, typically 25%, may be significantly reduced in the future, as soon as undergoing studies, on the luminosity measurement and on the tuning of detector simulation packages in SAMUS region, are concluded.

The forward inclusive muon production cross section measured in the present thesis can also be used to study the production of bottom quarks in this forward region. This is a very important topic from the QCD point of view, and it is left for the short term future.

Glossary

In the scope of this thesis, the following terms may have a special meaning, be it HEP specific or experiment specific. Some of them are defined in the main text, but are also listed here for easier reference by non-experts.

- **Background** Any object which, due to incomplete or incorrect identification, becomes indistinguishable from other distinct objects, contaminating them;
- **Bottom** Fifth quark flavor, it is also called *beauty*;
- **Bunch** Each of the packets composing a pulsing beam;
- **CBPF** Brazilian Center for Physics Research (*Centro Brasileiro de Pesquisas Físicas*);
- **CC** Central Calorimeter;
- **CCCH** Central Calorimeter Coarse Hadronic;
- **CCEM** Central Calorimeter ElectroMagnetic;
- **CCFH** Central Calorimeter Fine Hadronic;
- **CCT** *Coarse Centroid Trigger*, the Level 1 muon trigger;
- **CD** Central Detector;
- **CDC** Central Drift Chamber;
- **CDF** *Collider Detector Facility*. Like DØ, it is another large spectrometer designed for the study of $p\bar{p}$ collisions at the Tevatron. CDF is located at BØ;
- **CERN** *Organisation Européenne pour la Recherche Nucleaire*;
- **CF** Central part of the Muon System ($|\eta| < 1$);
- **Charm** Fourth quark flavor;

- **CTEQ** Specific parameterizations for parton distribution functions, suggested by the CTEQ collaboration (*The Project on Collaborative Theoretical and Experimental Studies of QCD*);
- **DØ** Name for the spectrometer whose data were used in the present work, and also for the international collaboration which has constructed and operates the DØ spectrometer;
- **DAq** Data Acquisition System;
- **DFLM** Specific parameterizations for parton distribution functions, suggested by Diemoz, Ferroni, Longo and Martinelli^[58];
- **EC** Endcap Calorimeter;
- **ECEM** Endcap Calorimeter ElectroMagnetic;
- **ECIH** Endcap Calorimeter Inner Hadronic;
- **ECMH** Endcap Calorimeter Middle Hadronic;
- **ECN** Endcap Calorimeter North;
- **ECOH** Endcap Calorimeter Outer Hadronic;
- **ECS** Endcap Calorimeter South;
- **EF** Intermediate part of the Muon System ($1 < |\eta| < 1,6$);
- **Farm** Array of interconnected computers or processors, working synchronously in a cooperative fashion, with the purpose of improving the overall performance (parallel processing);
- **FDC** Forward Drift Chambers;
- **FermiLab** Fermi National Accelerator Laboratory;
- **ICD** Inter-Cryostat Detector;
- **ICH** Inner Coarse Hadronic;
- **IFH** Inner Fine Hadronic;
- **L1TF** Level 1 Trigger Framework. It is the coordinator for the DØ Trigger System, at hardware level;
- **L1MU** Level 1 Muon Trigger
- **LAFEX** Cosmology and Experimental High Energy Physics Laboratory (*Laboratório de Cosmologia e Física Experimental de Altas Energias*);

- **LAr** Liquid Argon, used as active medium in $D\bar{O}$ sampling calorimeters;
- **Latch** Electronic device which keeps digital signals in their state at a specific time, called *sampling time*;
- **LHC** Large Hadron Collider, under construction at CERN;
- **LINAC** LINear ACcelerator;
- **LO** *Leading Order*, the lowest order of Perturbative QCD;
- **MAC** Module Address Card, component of the Muon System Electronics;
- **MCH** *Moving Counting House*, the place where most of the signal processing electronics is located.
- **MCH** Middle Coarse Hadronic;
- **MFH** Middle Fine Hadronic;
- **MG** Massless Gaps — scintillator plates located inside the cryostats;
- **MIP** Minimum Ionizing Particles;
- **MRS** Specific parameterizations for parton distribution functions, suggested by Martin, Roberts and Stirling^[59];
- **NLO** Next to Leading Order — second order in Perturbative QCD;
- **NNLO** Next to Next to Leading Order — third order in Perturbative QCD;
- **Off-line** Refers to any selection criteria or processing stage performed after the events are stored in magnetic media. In principle, any off-line step is reversible, in the sense that its effects can always be improved or removed. Some examples are the reconstruction and data analysis processing);
- **On-line** Refers to any selection criteria or processing stage performed at the time of event collection, before the event is written to permanent storage media. In principle, all on-line steps are irreversible, as they usually imply the elimination of events prior to their storage. Some examples are the triggers (any level), digitization, and so forth.
- **OTC** *Octant Trigger Card*, electronic boards composing the Level 1.5 Muon Trigger;
- **Overlap** Intermediate region where muon tracks traverse both SAMUS stations and WAMUS chambers;
- **PAW** *Physics Analysis Workstation*, software package designed for the statistical analysis of experimental data;

- **PDT** *Proportional Drift Tubes*. Each one of the cells composing WAMUS and SAMUS systems;
- **PLD** *Programmable Logic Devices*. Digital electronic devices, whose logic can be user programmed according to specific needs;
- **QCD** *Quantum ChromoDynamics*. The gauge theory describing color (or strong) interactions through the exchange of gluons;
- **QED** *Quantum ElectroDynamics*. The gauge theory describing electromagnetic interactions through the exchange of photons;
- **Quark** A kind of elementary particles (see Chapter 2);
- **RCP** *Run Control Parameters*. Files with groups of related parameters, which conveniently control the processing in most of DØ specific software packages.
- **Run** Data collection periods, during which all relevant detector parameters are reasonably constant in time;
- **SAMUS** *Small Angle MUon System* ($2,2 < |\eta| < 3,3$). The present thesis is based on data collected in this subdetector.
- **STC** *SAMUS Trigger Card*. Electronic boards composing the Level 1 Muon Trigger in SAMUS and Overlap regions;
- **Store** Time period (about 24 hours or less) during which the same bunches of protons and antiprotons are kept circulating and colliding in the Tevatron accelerator ring;
- **Top** Sixth (and last?) quark flavor. Top is the heaviest quark, and its existence has been confirmed recently.
- **Tevatron** The main accelerator ring at Fermilab, able to produce proton and antiproton beams with energies of up to 1 TeV;
- **TRD** Transition Radiation Detector;
- **Trigger** System responsible for selecting which events are to be recorded in permanent storage media. The trigger system also fires the data acquisition system to record the raw data for the selected events;
- **VTX** VerTeX Detector;
- **WAMUS** Wide Angle MUon System;

References

- [1] Aubert, J.J. *et al.*, *Phys. Rev. Lett.* **33**: 1404 (1974)
- [2] Augustin, J.E. *et al.*, *Phys. Rev. Lett.* **33**: 1406 (1974)
- [3] Anjos, J.C. *et al.* (E691), *Phys. Rev.* **D37**: 2391 (1988)
- [4] Alves, G.A. *et al.* (E769), *Phys. Rev. Lett.* **69**: 3147 (1992) *Phys. Rev. Lett.* **70**: 722 (1993)
- [5] Banerjee, S. *et al.* (E791), *FermiLab-CONF-94-125-E* (1994)
- [6] Frabetti, P.L. *et al.* (E687), *Phys. Lett.* **B323**:459 (1994)
- [7] Lima, J.G.R., “Análise Experimental do Decaimento Fraco $D^+ \rightarrow \phi K^+$, Duplamente Suprimido por Cabibbo”, M.Sc. Thesis, LAFEX/CBPF (1991)
- [8] Anjos, J.C. *et al.* (E691), *Phys. Rev. Lett.* **69**: 2892 (1992)
- [9] Carvalho, W.P., “Análise Experimental do Modo de Decaimento $D^+ \rightarrow \pi^+ \mu^+ \mu^-$ com Troca de Sabor do Quark c por Corrente Neutra”, M.Sc. Thesis, LAFEX/CBPF (1993)
- [10] Mello, C.G.B., “Procura por Correntes Neutras que Trocam Sabor pela Análise do Decaimento $D^+ \rightarrow \pi^+ \mu^+ \mu^-$ ”, M.Sc. Thesis, PUC/RJ (1994)
- [11] Nguyen, A. *et al.* (E791), *FermiLab-CONF-94-187-E* (1994)
- [12] Herb, S.W. *et al.*, *Phys. Rev. Lett.* **39**: 252 (1977)
- [13] Albajar, C. *et al.* (UA1), *Z. Phys.* **C48**: 1 (1990)
Albajar, C. *et al.* (UA1), *Phys. Lett.* **B257**: 459 (1991)
- [14] Akesson, T. *et al.* (UA2), *Z. Phys.* **C46**: 179 (1990)
Alitti, J. *et al.* (UA2), *Phys. Lett.* **B280**: 137 (1992)
- [15] Abachi, S. *et al.* (DØ), *Phys. Rev. Lett.* **74**: 2422 (1994)
- [16] Abe, F. *et al.* (CDF), *FermiLab-PUB-94-097-E* (1994)

- [17] Abachi, S. *et al.* (DØ), *Phys. Rev. Lett.* **74**: 2632 (1994)
- [18] Abe, F. *et al.* (CDF), *Phys. Rev. Lett.* **74**: 2626 (1994)
- [19] Geiser, A., “Beauty Production at CERN Proton Antiproton Collider: A Test of QCD”, Ph.D. Thesis, Rheinisch-Westfälischen Technischen Hochschule Aachen (1992)
- [20] Halzen, F. and Martin, A.D., “Quarks and Leptons, An Introductory Course in Modern Particle Physics”, John Wiley & Sons, Inc., New York, USA (1984)
- [21] Leader, E. and Predazzi, E., “Gauge Theories and the New Physics”, Cambridge Univ. Press, Cambridge, England (1982)
- [22] Commins, E.D. and Bucksbaum, P.H., “Weak Interactions of Leptons and Quarks”, Cambridge Univ. Press, Cambridge, England (1983)
- [23] Bjorken, J.D. and Drell, S.D., “Relativistic Quantum Mechanics”, McGraw-Hill, New York, USA (1964)
- [24] Glück, M. *et al.*, *Phys. Rev.* **D17**: 2324 (1978)
Combridge, B.L., *Nucl. Phys.* **B151**: 429 (1979)
- [25] Nason, P. *et al.*, *Nucl. Phys.* **B303**: 607 (1988)
Nason, P. *et al.*, *Nucl. Phys.* **B327**: 49 (1989)
- [26] Mangano, M. *et al.*, *Nucl. Phys.* **B373**: 295 (1992)
- [27] Altarelli, G. and Parisi, G., *Nucl. Phys.* **B126**: 298 (1977)
- [28] Plochow-Besch, H., “PDFLIB: Structure Functions and α_s Calculation”, User’s Manual - Version 3.00, W5051 PDFLIB, CERN-PPE.1992.06.27 (1992)
- [29] Botts, J. *et al.* (CTEQ), *Phys. Lett.* **B304**: 159 (1993)
- [30] Ferbel, T., “Experimental Techniques in High Energy Physics”, Addison-Wesley Publ. Company, Inc. (1987)
- [31] Paige, F. and Protopopescu, S., BNL Report n° 38034 (1986)
- [32] Marchesini, G. *et al.*, *Comput. Phys. Commum.* **67**: 465 (1992)
- [33] Giele, W.T. *et al.*, *Nucl. Phys.* **B403**, 633 (1993)
- [34] Sjöstrand, T., “Pythia 5.6 and Jetset 7.3, Physics and Manual”, CERN-TH.6488/92 (1992)
- [35] Peterson, C. *et al.*, *Phys. Rev.* **D27**: 105 (1983)
- [36] “Review of Particle Properties”, *Phys. Rev.* **D50**: 1 (1994)

- [37] Oguri, V., “Produção Inclusiva de Bottom em Colisões $p\bar{p}$ a $\sqrt{s} = 1,8$ TeV na Região Central do Detetor DØ”, Ph.D. Thesis, LAFEX/CBPF (in preparation)
Abachi, S. *et al.*, *Phys. Rev. Lett.* **74**, 3548 (1995)
- [38] Design Report, The DØ Experiment at Fermilab \bar{p} - p Collider, November 1984
- [39] Abachi, S. *et al.*, The DØ Detector, *Nucl. Instr. and Meth. in Phys. Res.* **A338**, 185 (1994)
- [40] Fernow, R., “Introduction to Experimental Particle Physics”, Cambridge Univ. Press, Cambridge, England (1986)
- [41] Aronson, S. *et al.*, *Nucl. Instr. and Meth. in Phys. Res.* **A269**, 492 (1988)
- [42] Rosenfeld, M., “Final Report on Design Review of the DØ Central Calorimeter Module Assembly”, *DØNote #654* (1987)
- [43] Yu, J., Ph.D. Thesis, State University of New York at Stony Brook, New York, USA (1993)
- [44] Abachi, S. *et al.*, *Nucl. Instr. and Meth. in Phys. Res.* **A324**, 53 (1993)
- [45] Featherly, J., *ORACLE and DEC Rdb/VMS Comparison*, *DØNote #324* (1985)
- [46] Brun R. *et al.*, ZEBRA User Guide (3.53), CERN Program Library Q100 (1987)
- [47] Hagopian, S., “DØ H PLOT – DI3000 User’s Guide”, *DØNote #483* (1986)
- [48] Hagopian, S., “DØ Event Display Users Guide Pixie V2.1”, *DØNote #941* (1990)
- [49] Shiers, J.D. *et al.*, “FATMEN (1.40) – The Complete Reference”, CERN Program Library Q123 (1992)
- [50] Carminati, F. *et al.*, GEANT User’s Guide (3.15), CERN Program Library (1992)
- [51] Raja, R., *Proceedings of the Workshop on Detector Simulation for the SSC*, Argonne, IL (1987)
Graf, N.A., *Proceedings of the First International Conference on Calorimetry in High Energy Physics*, Batavia, IL (1990)
- [52] Murphy, C., “Monte Carlo Study of $B - \bar{B}$ Produced J/Ψ ’s and their Triggering at DØ”, *DØNote #1608* (1992);
- [53] PAW, the Complete Reference (1.07), CERN Program Library Q121 (1993)
- [54] Denisov, D. and Eroshin, O., “Efficiency of the single muon detection in SAMUS spectrometer of the D0 detector for Run 1B”, *DØNote #2282* (1994)
- [55] Lafferty, G.D. and Wyatt, T.R., “Where to Stick Your Data Points: The Treatment of Measurements Within Wide Bins”, *CERN-PPE/94-72* (1994)

- [56] Efimov, A., “Momentum and angular resolutions of the SAMUS spectrometer with DØRECO version 12”, *DØNote #2093* (1994)
- [57] Elvira, V.D. *et al.*, “Smearing Correction to the Jet Cross Sections”, *DØNote #2247* (1994)
- [58] Diemoz, M. *et al.*, *Z. Phys.* **C39**: 21 (1988)
- [59] Martin, A.D. *et al.*, *Phys. Rev.* **D37**: 1161 (1988); *Phys. Lett.* **B206**: 327 (1988); *Mod. Phys. Lett.* **A4**: 1135 (1989)